Hochschule für Angewandte Wissenschaften Hamburg
Hamburg University of Applied Sciences

Projekt 2

Studiendepartment Fahrzeugtechnik und Flugzeugbau

An Approach to Involving Testing and Software Computing into the Predictions of Model Aircraft Engine Performance

Arno Apffelstaedt

30. Juni 2008

Hochschule für Angewandte Wissenschaften Hamburg
Fakultät Technik und Informatik
Department Fahrzeugtechnik + Flugzeugbau
Berliner Tor 9
20099 Hamburg

in Zusammenarbeit mit:

University of Limerick
Department of Mechanical & Aeronautical Engineering
Limerick
Ireland

Verfasser: Arno Apffelstaedt
Abgabedatum: 30.06.2008

Prüfer: Prof. Dr. Dieter Scholz, MSME
Betreuung: Dr. Trevor Young, Senior Lecturer

Abstract

The module of aircraft design at the University of Limerick is taught by using the annually Design/Build/Fly (D/B/F) Competition of the American Institute of Aeronautics and Astronautics (AIAA). The students are assigned to design an unmanned, electrical powered and radio controlled aircraft which satisfies best the given mission objectives. In several flight tests, it was found out that the thrust generated by the propellers does not seem to match expectations. This report deals with the question how to use testing and software computing to predict the performance of model aircraft engines accurately. An existing motor test rig was redesigned to produce accurate measurements on the power system. Two motors, the Hacker A60-18M and the Plettenberg HP370/50/A3, were chosen to be tested consecutively with two different propellers, the APC 20x10 and the APC 22x12W. The motors were powered with battery packs of identical design and capacity. The force of the propeller pulling forward was measured and recorded. Further, the rotational rate of the propeller, the speed of air exiting the propeller and the motor voltage and current were measured. The time a power system could provide a constant thrust value was calculated and named the 'usable running time'. The measured performance from static and wind tunnel tests was contrasted to the equipment's theoretical performance and to the estimates of computer software called Propeller Selector. It was found out that the performance measured was close to propeller and battery discharge theory. The usable running time was found to be a function of the battery discharge and independent from the motor-propeller combination used. It was further found out that the estimates of the Propeller Selector were close to the results of the static tests. A mean down deviation of 5.22 per cent was found. Measurements of the wind tunnel tests were found to be doubtable. The small diameter of the wind tunnel air stream could not provide a uniform airflow over the propeller diameter. As a result, the estimates of the Propeller Selector were far-off the measured performance. The deviation averaged out at 36.24 per cent. A CD containing test data is included in the appendix.

Acknowledgements

First, I would like to thank Dr. Trevor Young, senior lecturer at the University of Limerick and my supervisor for this project. It is due to him that I was able to do this project. Thanks for helpful advice how to write my report and for the expert knowledge during the test phase.

Many thanks to Dr. Dieter Scholz, lecturer and Erasmus coordinator at the HAW Hamburg, who established my first contact with Dr. Trevor Young and the University of Limerick.

Many thanks to Mr. Conny Schmidt, doctoral candidate at the University of Limerick, who gave me all the advice and practical support I required. Moreover, he brought forward many ideas, which are discussed in this report.

Many thanks to Mr. John Cunningham and Mr. Adrian McEvoy, senior technicians for the aeronautical labs at the University of Limerick, who supported me with expert knowledge, personal time and equipment. Thanks also for setting up my experimental apparatus and for building all parts that were needed for the new-designed test rig.

My thanks go also to the students of last year's aircraft design module, for designing and building a large part of the test rig used.

Content

List of Figures

List of Tables

Nomenclature

Symbols

a'	inflow factor
C_n	nominal battery capacity [Ah]
D	propeller disc diameter [m]
F	force [N]
F_D	drag [N]
F_F	forward force [N]
g	earth gravity [$m \cdot s^{-2}$]
I	current [A]
I_{in}	input current [A]
J	advance ratio
m	mass [kg]
M_C	multiple or fraction of C [h^{-1}]
m_i	measuring points in thrust measurements
n	number of measurements taken
n	propeller revolutions per unit time [s^{-1}]
P	power [W]
p	pressure [Pa]
p_0	static pressure [Pa]
$P_{absorbed}$	power absorbed [W]
P_{in}	input power [W]
P_{out}	output power [W]
q	dynamic pressure [Pa]
r	propeller radius [m]
T	thrust [N]
$T_{average}$	average thrust produced [N]
T_i	single thrust measurement [N]
T_K	absolute temperature [K]
$t_{storage}$	battery storage time [days]
t_{usable}	usable running time [s]
U	voltage [V]
U_{in}	input voltage [V]
v	velocity of air or flight speed [$m \cdot s^{-1}$]
v_{pitch}	velocity of air exiting the propeller [$m \cdot s^{-1}$]
v_{tip}	tip speed [$m \cdot s^{-1}$]
Z_a	number of armature conductors (electrical motor)

Greek Letters

α	blade angle
η_i	Froude efficiency or Froude ideal
η_p	propeller efficiency
η_{Total}	total efficiency of the motor-propeller combination
λ	pitch or pitch length [m]
ρ	mass density of the air [$kg \cdot m^{-3}$]
σ	standard deviation
τ	motor torque [Nm]

Abbreviations

AIAA	American Institute of Aeronautics and Astronautics
APC	Advanced Precision Composites
D/B/F	Design/Build/Fly
GP	Gold Peak International Ltd.
GRS	Geodetic Reference System
IAG	International Association of Geodesy
M	metal
MH	metal hydride
NACA	National Advisory Committee for Aeronautics
NiCd	nickel-cadmium
NiMH	nickel-metal hydride

1 Introduction

Since the year 2005, the module of aircraft design at the University of Limerick is taught by using the annually Design/Build/Fly (D/B/F) Competition of the American Institute of Aeronautics and Astronautics (AIAA). The students are assigned to design an unmanned, electrical powered and radio controlled aircraft which satisfies best the given mission objectives.In addition, as the mission objectives reflect a flight mission of real size transport aircraft the usual design approach of the aerospace industry has to be used. The competition as well as the use of it as a teaching method gives the student the chance to be part of a aircraft design process that is as close to the real world as possible.

When the design of the aircraft is complete, it has to be proven successful by building the aircraft and showing its actual flight performance. To succeed in doing so, the quest for the optimal power system is a crucial part of the designing process. The power system sets limits for the manoeuvrability, weight and possible mission length of the aircraft. Where a lot of fuselage and wing design can easily be adopted from real aircraft design approaches, the decision for an electric power system needs the thoughtful implementation of model aircraft knowledge. As past projects have shown, the complexity of this task makes it problematic to asses the true performance of the chosen power system. In several flight tests, which followed the aircraft assembly, it was found out that the thrust generated by the propellers did not match expectations.

This report tries to find ways to implement laboratory pre-flight tests and software computations of the chosen power systems into the design process to predict the in-flight performance accurately. An existing motor test rig was redesigned to achieve thrust over time measurements of the power system. In addition, several other measurements were added into the test procedure.To ascertain the accuracy of the test rig, two motors equipped with two propellers were tested on the test rig. The test included static tests and wind tunnel tests on the Eiffel wind tunnel at the University of Limerick. Afterwards, the test results were compared to the theory of propeller performance and to the theory of battery discharge.
Finally, computer software estimations were compared to the test results. It should be found out, if accurate performance estimations can be made possible without performing time-intense laboratory testing.

1.1 Goals and Objectives

The following objectives were set for this project:

- Ascertain the performance of motors and propellers used
- Contrast the measured performance to the equipment's theoretical performance
- Evaluate the difference between static and wind tunnel tests
- Evaluate the thrust estimates of computer software
- Complete the development of the test rig

2 Theory

2.1 Electrical Model Aircraft Engine Performance

The power system of an electrical driven model aircraft can roughly be compared to the power system of a piston-engine driven real-size aircraft as in both cases the thrust is produced by the revolving of a propeller. Both, piston-engine and electrical motors convert input power into shaft power, which then drives the propeller. Besides the propeller thrust, there is no such secondary thrust produced as for example by a jet exhaust of a turboprop engine. A major difference of electrical motors to piston-engines is that the shaft power produced is not affected by a mass flow of air into an intake manifold and therefore not influenced by the outside air-density.

2.2 The Brushless DC Motor

Basic Principle

The principle of all electric motors is based on the repulsing and attracting forces between magnets. The basic theory goes back to a conductor that is located in a magnetic field. If a current is applied to the conductor, a magnetic field will be formed around that conductor. The magnetic field of the conductor is now located at right angles to the outer magnetic field, the flux lines of both magnetic fields will be either in the same or in opposite direction. Flux lines in the same direction will repel each other; flux lines in opposite direction will attract each other.

The magnetic forces will create a downward force on the conductor. A reverse in current will change the direction of the conductor's flux. Furthermore, if the current through the conductor is doubled, the downward force will be doubled. Using a coil instead of a single conductor, the forces on both sides will result in a magnetic torque:

$$\tau = 2 \cdot F \cdot r \tag{3.1}$$

where
τ = torque [Nm]
F = force [N]
r = radius, distance of coil-side to centre of rotation [m]

Moreover, if the coil is allowed to rotate, the north pole of the coil will move to the south pole of the outer magnetic field, and vice versa.
Imagining a shaft, driven by the torque, leads us to the understanding of the basic principle of an electric motor. Continuous rotation would then be possible through the continuous relative change of the magnetic forces or a continuous change in current. Conventionally, this can be realized either by using the frequency of an alternating current or by switching the current mechanically by using brushes. In a brushless direct-current motor, the current is switched electronically by using a controller. The turning part of a motor is called the rotor and is generally made up of many coils, to create a full circle of rotating conductors and therefore a constant torque.

Electric Aircraft Engines

When using the electric motor to turn a propeller, its torque has to be big enough to overcome the propeller's moment of inertia and its aerodynamic drag. The moment of inertia depends on the propeller's weight and its centre of gravity. The weight is influenced by the material used and the size of the propeller. If looking at propellers of the same material and shape, a larger propeller will have a bigger moment of inertia than a small one. Hence, the motor will need a bigger torque to drive the large propeller.The aerodynamic drag is depending on the airfoil and the twist of the propeller. This is discussed in more detail in chapter 3.3. For the motor torque of a two-pole construction **Sokia 1990** approximates:

$$\tau \approx Z_a \cdot \Phi \cdot I_a \tag{3.2}$$

where
Z_a = the number of armature conductors
Φ = field flux of outer magnetic field [Wb]
I_a = armature current [A]

The field flux of the outer magnetic field Φ and the number of armature conductors Z_a are generally constant in an electric motor. As can be seen in equation (3.2) the torque then is a function of the armature current I_a only. Again, if we want to turn a large propeller, the torque has to be bigger. For a given motor, the current I_a then has to be bigger.

2.3 The Propeller

Propeller Efficiency

The propeller as a whole can be seen in a rough estimate as an actuator disc that by rotating transfers energy to the surrounding air.

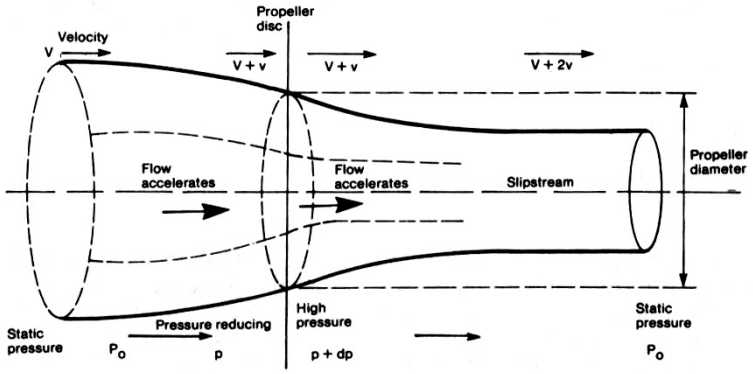

Figure 3.1 Pressure and velocity changes through the actuator disc (**Simons 1994**)

Figure 3.1 shows the revolving actuator disc and the changes in the airflow and pressure. On its way to the front of the disc, the pressure is reduced from the static pressure p_0 to a lower pressure p and therefore the velocity increases ($v+\Delta v$). When passing the disc, the energy transferred to the airflow results in an increase of pressure dp, whereas the velocity experiences a further enlargement ($v+2\Delta v$).

The thrust produced is given by the difference of pressure dp between the front and the rear of the actuator disc and can easily be calculated when assuming that the pressure change is evenly spread over the entire disc area (**Simons 1994**):

$$T = \frac{\pi}{4} \cdot D^2 \cdot dp \tag{3.1}$$

where
T = thrust [N]
D = disc diameter [m]
dp = difference of pressure [Pa]

Even the assumption that the pressure change is constant over the whole diameter is false for a real propeller, “particularly near the hub of a real propeller” (**Simons 1994**), it leads to a first understanding of the thrust produced.

To be able to make a statement about the efficiency of a power system, the ratio of Δv to v, the increase of air speed through the propeller to the actual flight speed is crucial to know. It is called the inflow factor and is directly related to the ideal or Froude efficiency of a propeller. The Froude efficiency η_i is the absolute efficiency limit of a propeller for a particular flight speed and power input. The true efficiency of a propeller η_p can then be compared to its ideal.

$$a' = \frac{\Delta v}{v} \tag{3.2}$$

$$\eta_i = \frac{1}{1 + a'} \tag{3.3}$$

$$\eta_p = \frac{T \cdot v}{P} \tag{3.4}$$

where

a' = inflow factor
Δv = speed increase through the actuator disc [ms^{-1}]
v = flight speed [ms^{-1}]
η_i = Froude efficiency or Froude ideal
η_p = propeller efficiency
P = shaft power input [W]

Looking at equation 3.1 a certain thrust can be attained either by a small propeller running at a high rotation speed (*D* small, *dp* large) or by a large propeller at a slow rate (*D* large, *dp* small). As equation 3.3 shows, the Froude efficiency is large when the air speed increase through the propeller is small. Therefore, the larger, slow running propeller would have a better efficiency. Unfortunately, for real-sized aircraft as well as for model aircraft the propeller size is limited. The efficiency falls rapidly if the propeller blades are too large that their tip speed reaches the speed of sound (**Raymer 1999**). As the speed of sound is rarely reached with model aircraft propellers, moreover ground clearance and undercarriage length set the limits (**Simons 1994**). The inflow factor in equation 3.2 is also influenced by the flight speed. Efficiency will crow with higher flight speeds until the overall drag equals the thrust.

Propeller Pitch

To specify the aspect of drag it is necessary to describe the propeller blades in more detail as rotating airfoils. The blade generates thrust the same way as a wing produces lift.

Propeller airfoils have a selected design lift coefficient. These average out at 0.5 for real-size aircraft propellers (**Raymer 1999**). To produce optimal lift a wing-airfoil has to be set at a

certain angle to the flight speed. Likewise, there is an optimal angle of attack for the propeller airfoil to produce its maximum thrust. As the angular speed along a rotating propeller blade increases with the radius, the relative airflow to the airfoil changes, as can be seen in fig 3.2. Propellers therefore show a varying twist along their blade axis. Furthermore, figure 3.2 shows that the relative airflow depends as well on the flight speed. For every single flight speed, the optimal angle of attack is a different one. With the following equations, the tip speed can be calculated (**Raymer 1999**):

$$(v_{tip})_{static} = \pi \cdot n \cdot D \tag{3.5}$$

$$(v_{tip})_{helical} = \sqrt{(v_{tip})_{static}^{\ 2} + v^2} \tag{3.6}$$

where

n = rotational rate [s^{-1}]
D = propeller diameter [m]
v_{tip} = tip speed [ms^{-1}]
v = flight speed [ms^{-1}]

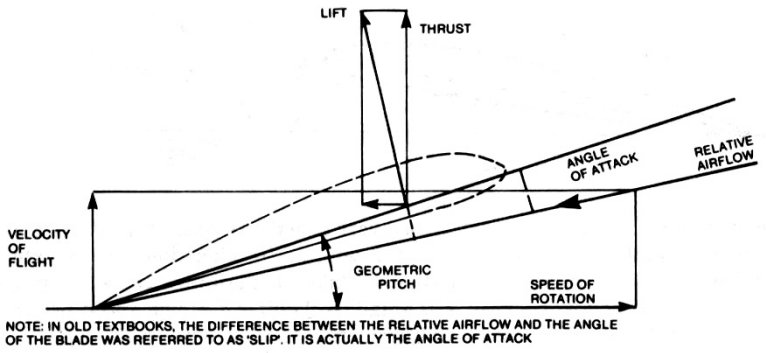

Figure 3.2 Pitch and relative airflow at the propeller blade (**Simons 1994**)

The pitch of an aircraft propeller refers to its ‘all-over’ angle of attack and is given as a length. Reason for this is shown by **Simons 1994**: “The basis of this figure [pitch represented as a length] is the notional distance the propeller would advance in one revolution if it were literally screwing itself through a solid medium like a screw or a bolt.” The ‘all-over’ pitch of a propeller corresponds to the angle of the blade at 75 per cent of the distance from hub to tip (**Raymer 1999**, **Simons 1994**). If the pitch is given as a length, the blade angle can be calculated using the following formula:

$$\tan\alpha = \frac{\lambda}{\pi \cdot 0.75D} \tag{3.7}$$

where

α = blade angle at 75 per cent of the distance from hub to tip

λ = pitch or pitch length [m]

Most real-size piston-engine driven aircraft are equipped with a variable pitch propeller, which allows the pilot to change the pitch while flying, so that it is theoretically always running most efficiently. This technique is mechanically regarded very complicated even for real-size aircraft what makes it difficult to use it for small model ones. If a variable pitch propeller cannot be realized, there are two different ways to deal with the design of a "fixed-pitch" propeller. One way is to use a constant pitch propeller that is designed to have an optimal efficiency at a certain flight and rotation speed. This can be useful for competitive racer model aircraft, which are supposed to attend only their maximum cruising speed. For models that have to fly flight missions, where different mission segments are flown at different cruising speeds, it is better to use fixed-pitch propellers that have a changing pitch in radial direction. Even they never reach a peak in efficiency as they are not designed for one speed, they can operate at reasonably good efficiencies throughout the whole flight mission. With a constant pitch propeller they would fly most of the time "off-design" what at worst could mean the risk of a propeller stall at 75take-off, where the flight speed is low and the rotating speed very high (**Simons 1994**). **Raymer 1999** differentiates fixed-pitch propellers between "cruise props" and "climb props" depending upon the flight condition favoured during the design approach.

The amount of drag produced by a propeller (or its resistance to the air) increases with both, its diameter and its pitch. When using a fixed-pitch propeller, the diameter to pitch ratio d/p is stated as well. As a result, if a larger propeller should be driven at the same revolution rate as a smaller one, the pitch has to be reduced. In other words, the diameter to pitch ratio has to be increased (**Simons 1994**). Fig 3.3 expresses the relationship between intended flight speed, rotational rate, and propeller pitch for model aircraft. Note that the propeller pitch in this figure is given the symbol *P*. With a given pitch and flight speed the remaining variable is the propeller diameter. It can be seen that the diameter then has a dominant effect on the power required to drive the propeller.

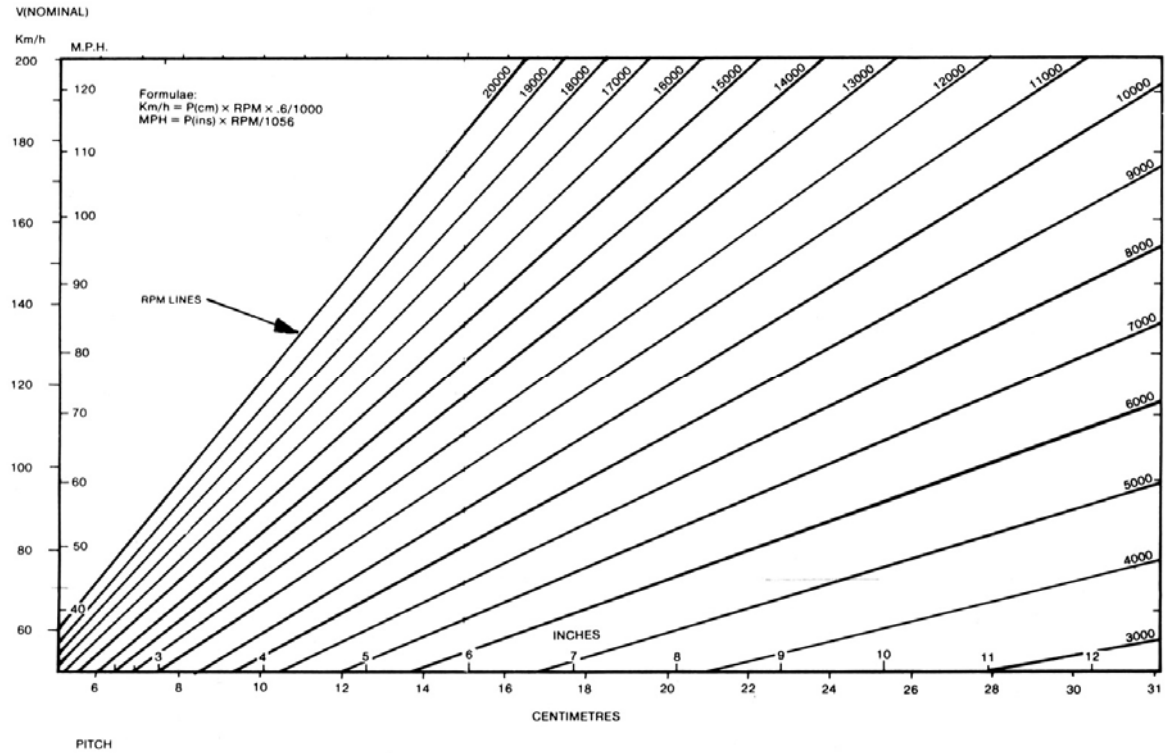

Figure 3.3 Intended flight speed vs. propeller pitch (**Simons 1994**)

2.4 The NiMH Battery

General Characteristics

The characteristics of a nickel-metal hydride (NiMH) battery are similar to those of a nickel-cadmium (NiCd) battery, but the electrochemical reaction is based on hydrogen instead of cadmium as the active negative material. As the metal hydride electrode has a higher energy density, the negative electrode can be smaller than the one of a NiCd battery. That results in a higher capacity for the NiMH battery as the volume of the positive electrode can be larger. Moreover, a battery not containing cadmium is more environmental friendly (**GP 2006**). Unfortunately, the NiMH battery does not have the same high rate capability of the nickel-cadmium battery and is less tolerant to overcharge (Linden 1995). Advantages and disadvantages of NiMH batteries are summarized in Table 3.1.

Table 3.1 Advantages and Disadvantages of Nickel-Metal Hydride Batteries (Linden 1995)

Advantages	**Disadvantages**
• Higher capacity than NiCd batteries • Sealed construction, no maintenance required • Cadmium-free, minimal environmental problems • Rapid recharge capability • Long cycle life • Long shelf life in any state of charge	• High-rate performance not as good as with NiCd batteries • Poor charge retention • Moderate memory effect

NiMH Chemistry

As of any other rechargeable battery, the mode of operation of a nickel-metal hydride battery is based on a reversible electrochemical reaction. The over-all electrochemical reaction can be simplified to the following two equations (**GP 2006**):

Charging $$Ni(OH)_2 + M + e^- \rightarrow NiOOH + MH \quad (3.8a)$$

Discharging $$NiOOH + MH \rightarrow Ni(OH)_2 + M + e^- \quad (3.8b)$$

where
$Ni(OH)_2$ = nickel hydroxide
$NiOOH$ = nickel oxy-hydroxide
MH = metal hydride

M = metal (mostly titanium or zirconium)
e^- = electrical energy (electron)

When charged, the electrical energy input (e^-) converts $Ni(OH)_2$ to the higher energy NiOOH. When used, the battery discharges by releasing electrical energy (e^-) and converting NiOOH back to $Ni(OH)_2$. M is representing a hydrogen-storage alloy, mostly titanium or zirconium.
As can be seen in figure 3.4 the $Ni(OH)_2$ forms the positive electrode and the M-alloy the negative one. A simple transfer of H atoms between the positive and negative electrode happens during charge and discharge.

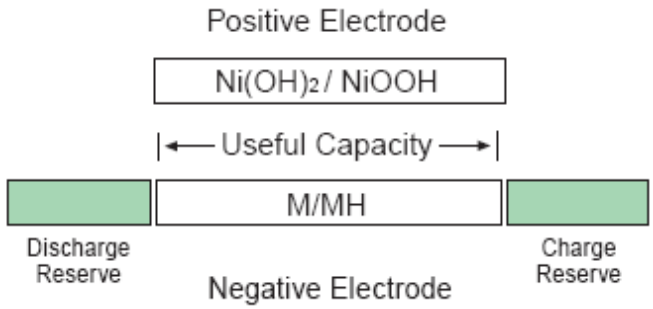

Figure 3.4 Relationship between useful capacity, charge reserve, discharge reserve. (**GP 2006**)

Charging Characteristics of NiMH Batteries

Generally speaking, it is more efficient to charge the batteries at or below room temperature, as the chemicals in the positive and the negative electrode are more stable. Consequently, the discharge capacity is higher (**GP 2006**). As figure 3.5 depicts, discharge capacity falls when exceeding too high ambient temperatures while charging.

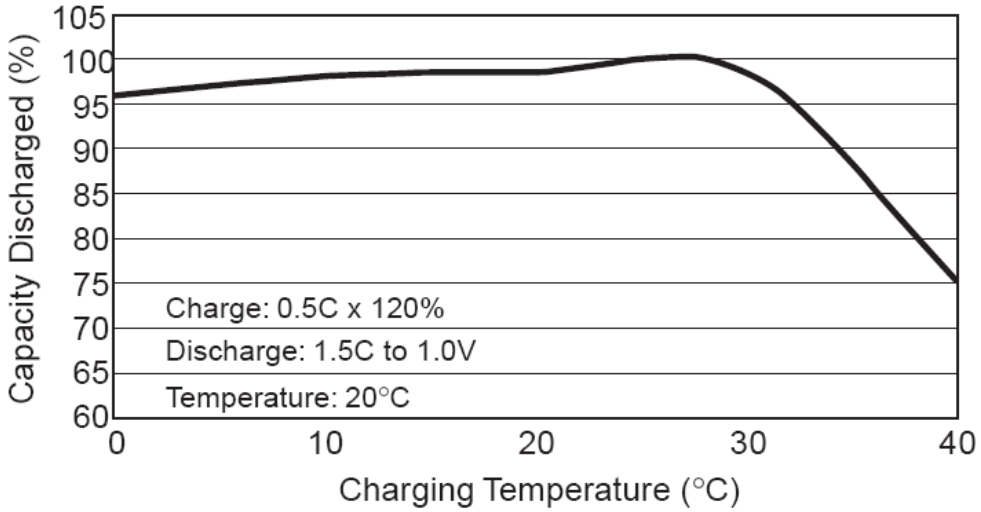

Figure 3.5 Charge-Temperature Characteristics of Standard Series (**GP 2006**)

Indicating Current with the C rate

The value "0.5 C" in figure 3.5 is called the C rate. It is a typical method for indicating the charge and discharge current of a battery. The current is then defined as follows (Linden 1995):

$$I = M_C \cdot C \tag{3.9a}$$

where
I = discharge/charge current [A]
C = nominal, numerical value of rated capacity of a cell or a battery [Ah]
M_C = multiple or fraction of C [h^{-1}]

For example, if a battery with a nominal capacity of 2200 mAh is charged at 1100 mA, M is 0.5:

$$M_C = \frac{I}{C} = \frac{1100}{2200} = 0.5 \tag{3.9b}$$

In this case, the battery is charged with a rate of 0.5 C. If charged at a current of 6.6 A, it would be charged at a rate of 3.0 C.

Discharging Characteristics of NiMH Batteries

As **GP 2006** explains, the nominal discharge capacity of a NiMH battery is rated at 0.2 C to an end voltage of 1V after charging at 0.1 C for 14 to 16 hours. In other words: to get a 100 percent nominal discharge capacity, the battery has to be overcharged to at least 140 percent at a very low current. Furthermore, the 100 percent discharge capacity can only be achieved when discharging with a C rate at or lower 0.2. For our battery example with 2200 mAh, a discharge rate of 0.2 C would mean a discharge current of 440 mA. The battery would then have a 100 percent capacity of eleven hours (2200 mAh divided by 0.2). When discharged at 1.0 C (2200 mA), the energy will last for less than one hour. In a few words, the higher the current, the lower the capacity. Nearly the same behaviour can be found for the discharge voltage. As for the capacity, the nominal discharge voltage of 1.2 V of NiMH batteries is measured at a discharge rate of 0.2 C. The discharge voltage is reduced by higher discharge currents. NiMH manufactures therefore recommend a discharge rate not higher 3.0 C, otherwise the useable output voltage would simply be two low for most applications (GP 2006).

As can be seen in figure 3.7, a flat discharge profile after a sudden voltage drop is characteristic, especially for low C rates. With higher currents not only is the capacity

shortened, but also the discharge voltage declines faster. Moreover, discharge capacity and voltage are affected by ambient temperature. When discharged at low temperatures both drop due to decreased molecular mobility.The effect of temperature becomes critical when both, high currents and low temperatures (< 10 °C) come together. The voltage then declines constantly due to the increasing resistance at low temperatures. In that case the characteristic flat discharge profile cannot be realized (Figure 3.6).

A lot of the foregoing is expressed in figure 3.7. It can be seen that the discharge voltage and discharge capacity drop rapidly with increasing current. As mentioned before, the nominal capacity is depleted when dropping below 1.0 V discharge voltage. A horizontal line indicates that fact. The effect of the discharge current on capacity in comparison with several secondary battery systems is shown in figure 3.8.

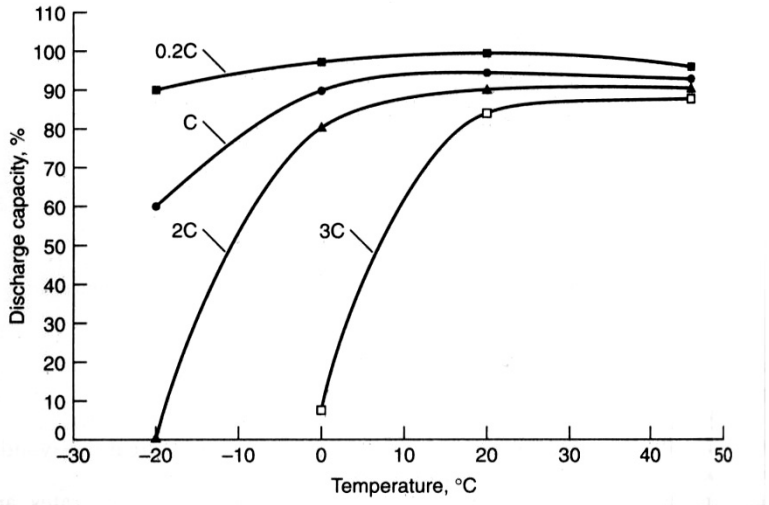

Figure 3.6 Discharge capacity at different C rates and ambient temperatures (Linden 1995)

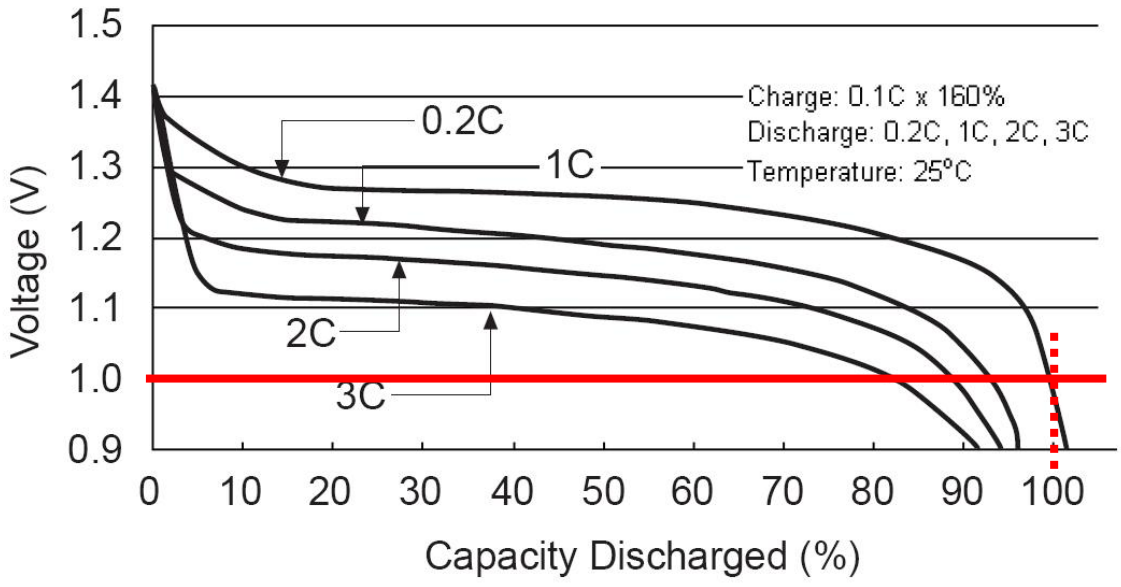

Figure 3.7 Discharge voltage over capacity at different C rates (**GP 2006**)

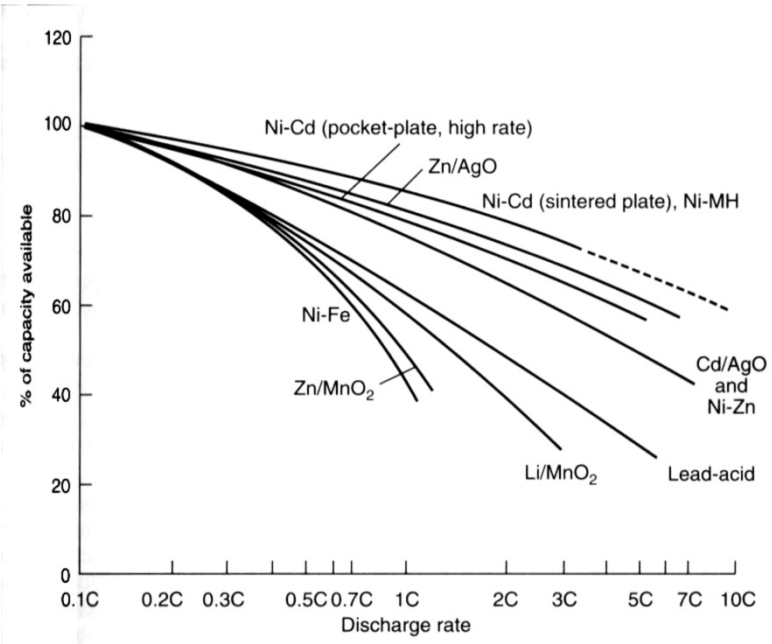

Figure 3.8 Discharge current vs. Capacity of different battery types (Linden 1995)

Voltage Depression (Memory Effect) and Self Discharge

Charging and discharging a nickel-metal hydride battery repeatedly without a full discharge can result in a loss of capacity and a drop of discharge voltage. When the battery is discharged only partially, then charged again, the active materials that have not been used change their physical characteristics "due to electrolyte dry-out" (**GP 2006**), and therefore increase battery resistance (Linden 1995). When discharged again, the voltage is depressed. This phenomenon is commonly known as the memory effect of a battery. The voltage depression is highly affected by the depth of discharge. It can be reduced if the battery is discharged to an appropriate end voltage. As Linden (1995) explains, "discharging to an end voltage below 1.1 V per cell should not result in a significant voltage depression or capacity loss".

When stored for a longer time, slow chemical reactions on both electrodes decrease the state of charge and capacity. This effect is called the self-discharge of a battery where the decrease is a function of ambient temperature and time. Higher ambient temperatures will result in a faster reduction of capacity. Figure 3.9 illustrates the capacity-loss due to storage over 30 days at different ambient temperatures.

Both, voltage depression and self-discharge will not result in a permanent capacity-loss.
In both cases, the capacity of a NiMH battery can be restored completely by charging and discharging the battery a few times (Linden 1995).

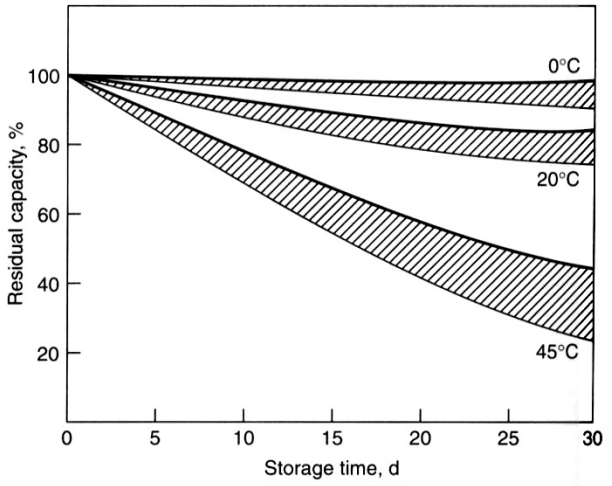

Figure 3.9 Capacity vs. Storage time and temperature (Linden 1995)

2.5 Software for Estimating Propeller Thrust

Background

To compare the results of the experiments to already existing propeller data, software called *Propeller Selector* (Gyles Aero Design) was used. The program calculates the thrust produced of two-, three-, and four bladed model aircraft propellers. The calculations are based on experimental data from the National Advisory Committee for Aeronautics (NACA) Technical Note No.698 (Appendix D). To estimate and compare the performance of real size aircraft propellers at different air speeds, experiments were carried out by the NACA at a wind tunnel at the Stanford University in the late 1930s. The NACA tested the propellers at blade angles of 15°, 25°, 35° and 45°. As explained in chapter 3.3, this angle refers to the blade angle at 75 per cent from the distance from propeller hub to tip. According to the author of the software Brian R. Gyles (2002), the propellers used by the NACA were similar in design to the ones used today on model aircraft. In particular, the propellers used by the NACA were tested at blade angles that can be found on model aircraft propellers today.

Inputs and Outputs

The inputs needed to estimate propeller performance with the *Propeller Selector* are pitch and diameter of the propeller, the rotational rate and the air speed. The outputs are thrust, power output, power absorbed and the propeller's efficiency. Additionally, the software provides a warning that stall conditions are being approached by changing the colour of the thrust output window. The airspeed can also be set to zero, which allows us to use the software for the

comparison with static thrust results as well as wind tunnel test results. It must be said that the software outputs ‘Power Output’ and ‘Efficiency’ can only be calculated if the input of ‘Air Speed’ is not zero. This is according to the general definition of propeller efficiency, which is defined as thrust by air speed over shaft power input. Figure 3.10 shows a screenshot taken from the *Propeller Selector* user interface.

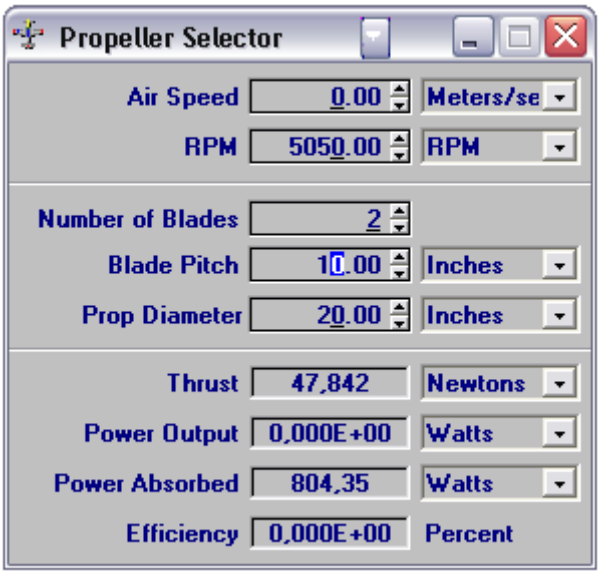

Figure 3.10 Propeller Selector User Interface (Gyles Aero Design Software)

3 Apparatus and Measurement Procedures

3.1 Apparatus

Test Rig

The test rig used for the experiments discussed in this report was mainly designed by students of aeronautical engineering of the University of Limerick. The design was slightly changed to be able to monitor and record the thrust continuously. This was mainly possible by using a smaller load cell and a digital transient recorder that transferred thrust readings to a computer program. The design process and the calibration of the modified test rig are described in detail in the corresponding appendix (Appendix A).

Motors

The two motors tested and compared for this report were brushless DC motors of similar size, weight and expected performance, the Hacker A60-18M (1) and the Plettenberg HP 370/50/A3 (2). Both motors are directly driven, i.e. they are not equipped with a gearbox. Further information on these motors can be found in the corresponding appendices.

Propellers

Two propellers were tested with the two motors mentioned above. The APC 20x10 is a fixed-pitch propeller with a pitch of 254 mm (10 in) and a diameter of 508 mm (20 in). The APC 22x12W is a fixed-pitch propeller with a pitch of 270 mm (12 in) and a diameter of 558.8 mm (22 in). The ‘W’ behind its classification refers to extra-wide propeller blades. Both propellers are made of glass-fibre composite material.

Batteries

All tests were undertaken using three battery packs consisting of twenty-eight GP2200 NiMH batteries in a series connection. The batteries have a nominal discharge capacity Cn of 1.2 Ah and a nominal discharge voltage of 1.2 V. The packs were always fully charged with a charging current of 3.0 A. According to equation (3.9b) the charging C rate is calculated as follows:

$$M_C = \frac{I}{C} = \frac{3.0}{2.2} = 1.\overline{36}$$

I.e. the batteries were charged with a C rate of $1.\overline{36}$.

The nominal discharge capacity to which the battery packs were charged was shown by the charging computer. Despite their identical configuration and charge processes, the battery packs showed differences in the indicated discharge capacity. To be able to distinguish between them in the tests, the battery packs were numbered. Table 4.1 shows the numbering and the optical differences between the battery packs. To eliminate further influencing factors, it was tried to use the same battery pack for each series of comparable test.

Table 4.1 Numbering and Identification of Battery Packs used

Battery Pack Identification Number	**Indicated Discharge Capacity**	**Optical Distinctive Feature**
1	2235 mAh	symmetric constellation: 4 line-ups each with 7 batteries one-part: all line-ups bond together
2	2221 mAh	symmetric constellation: 4 line-ups each with 7 batteries two-part: each 2 line-ups bond together
3	1850 mAh	asymmetric constellation: 3 line-ups with 9-10-9 batteries one part: all line-ups bond together

3.2 General Assumptions

Room temperature, ambient pressure and air density

For all experiments discussed in this report, the ambient conditions were measured and included in the computations of the test results. Direct measurements were the room temperature T and the ambient pressure p. From these two the density of air can be calculated using the following equation.

$$\rho = \frac{p}{R \cdot T_K} \tag{4.1}$$

where

ρ = air density [kg·m^{-3}]
p = static pressure [N·m^{-2}]
R = specific gas constant of dry air = 287.05 J·kg^{-1}·K^{-1}
T_K = absolute temperature [K]

Gravity

In addition, as the value of earth gravity is dependent on the location, the earth gravity for Limerick was calculated using equation (4.2) and included in the computations of the test results. Equation (4.2) is given by **Ahern 2007** and was developed, based on satellite data, by the International Association of Geodesy (IAG). It should be noted that Geodetic Reference System (GRS) formulae take into account only the change caused by latitude. The earth gravity also changes with altitude, as one is moving further away from the centre of gravity. Precisely, the gravity calculated with the following equation is only valid at sea level.

$$g = 9.7803267714 \cdot \left(\frac{1 + 0.00193185138639 \cdot \sin^2 \Theta}{\sqrt{1 - 0.00669437999013 \cdot \sin^2 \Theta}} \right) \tag{4.2}$$

where

g = earth gravity [m·s^{-1}] = 9.81274 m·s^{-1} (Limerick)
Θ = latitude in degrees = 52.3° (Limerick)

3.3 Direct Measurements

Direct Thrust

The thrust measurement apparatus consists of a load cell that restrains the propeller from moving forward. It is attached to a shaft that accommodates the motor and is located in the propeller's axis of rotation. The load cell then measures the pull upon the shaft or the propeller thrust. For wind tunnel measurements, the pull upon the shaft is the forward force. The thrust can then be calculated by determining the drag produced by the wind tunnel. This is described in more detail in chapter 4.4.

Propeller Revolution Speed

The revolution speed of the propeller was measured by a portable laser tachometer. A patch on the propeller blade reflects the laser light and sends it back to the tachometer. The tachometer then calculates the interval between to reflections and hence the propeller revolutions per minute.

Pitch Speed

To measure the dynamic pressure of air exiting the propeller, a pitot tube was permanently placed 50.8 mm behind the propeller blades. The pitot tube received the dynamic pressure at 110 mm distance from the hub and transferred it to a manometer. The speed of air can then be found by the equation:

$$v = \sqrt{\frac{2 \cdot q}{\rho}} \tag{4.3}$$

where
v = speed of air [ms^{-1}]
q = dynamic pressure [Pa]
ρ = air density [kgm^{-3}]

Motor Current and Voltage

The motor current was measured using a digital clamp ampere meter on the external circuit. A digital voltmeter was used to measure the voltage across the motor. As there are no consumer loads besides the motor, the motor current corresponds to the discharge current of the batteries. Similarly, the voltage across the motor is identical with the discharge voltage of the batteries.

3.4 Calculating Usable Running Time

The usable running time is the time the motor-propeller-battery combination can provide reasonably constant thrust at a certain power setting. The usable running time is therefore a measurement of thrust over time. This was possible as the load cell measuring the thrust was connected to a computer via a digital transient recorder. The transient recorder was recording measurements of the actual thrust every 0.5 sec while the motor was running. The usable running time was defined to start when the thrust becomes reasonably constant (tolerance: ± 5 %). To compensate high thrust fluctuations, not the thrust measurements themselves were compared, but the mean of *n* measurements. The mean values of three successive series were compared to the mean value of the one series preceding them.

The end condition, which stops the usable running time, was defined slightly different. It ended when the thrust peaked off five percent of its constant value. Again, the mean values of three series of thrust measurements were compared to a reference value. This time the reference value was the mean of all thrust measurements in the domain of the usable running time. The following equations illustrate the start (4.4a) and the end condition (4.4b).

$$m_s \Rightarrow 0.95 \le \frac{\left(\frac{\sum_{i=m+n}^{m+2n} T_i}{n}\right)}{\left(\frac{\sum_{i=m}^{m+n} T_i}{n}\right)} \le 1.05 \wedge 0.95 \le \frac{\left(\frac{\sum_{i=m+2n}^{m+3n} T_i}{n}\right)}{\left(\frac{\sum_{i=m}^{m+n} T_i}{n}\right)} \le 1.05 \wedge 0.95 \le \frac{\left(\frac{\sum_{i=m+3n}^{m+4n} T_i}{n}\right)}{\left(\frac{\sum_{i=m}^{m+n} T_i}{n}\right)} \le 1.05 \qquad (4.4a)$$

$$m_e \Rightarrow \frac{\left(\frac{\sum_{i=m}^{m+n} T_i}{n}\right)}{\left(\frac{\left(\sum_{i=m_s}^{m-1} T_i\right)}{(m-m_s-1)}\right)} \le 0.95 \wedge \frac{\left(\frac{\sum_{i=m+n}^{m+2n} T_i}{n}\right)}{\left(\frac{\left(\sum_{i=m_s}^{m-1} T_i\right)}{(m-m_s-1)}\right)} \le 0.95 \wedge \frac{\left(\frac{\sum_{i=m+2n}^{m+3n} T_i}{n}\right)}{\left(\frac{\left(\sum_{i=m_s}^{m-1} T_i\right)}{(m-m_s-1)}\right)} \le 0.95 \qquad (4.4b)$$

where

m = actual measuring point

m_s = measuring point starting the usable running time

m_e = measuring point ending the usable running time

T_i = single thrust measurement

n = number of thrust measurements in a series

3.5 Wind tunnel measurements

Wind tunnel

The wind tunnel tests in this report were carried out at the Eiffel wind tunnel of the University of Limerick, located inside the Lonsdale Building. The test rig was built up behind the rectangular open throat of the tunnel, which has side lengths of 493 mm (19.4 in).

Estimating distance of test rig to diffuser outlet

Wind tunnel tests are supposed to simulate a flight in free atmosphere, where the propeller is advancing through the air with a certain speed, the airspeed. As the propellers are larger in diameter than the open throat in side length, we had to move further away from the outlet.

At first, we used a simple approach by extending the diffuser virtually until the diameter of the diffuser reaches propeller size (see figure 4.1). For a 20 in (508 mm) propeller we had to move at least 237 mm away. This is a very naïve approach, as it expects the airflow to be constant over the whole size of the diffuser outlet. In reality, the airflow through the diffuser is varying from a maximum at its core to zero speed at the inner walls. Due to wall effects, the usable diameter of the airflow is highly reduced. To overcome this effect, we moved the test rig for the 20 in propeller to an overall distance of 500 mm away from the diffuser outlet. As can be seen below, the airflow over the propeller diameter was still not constant.

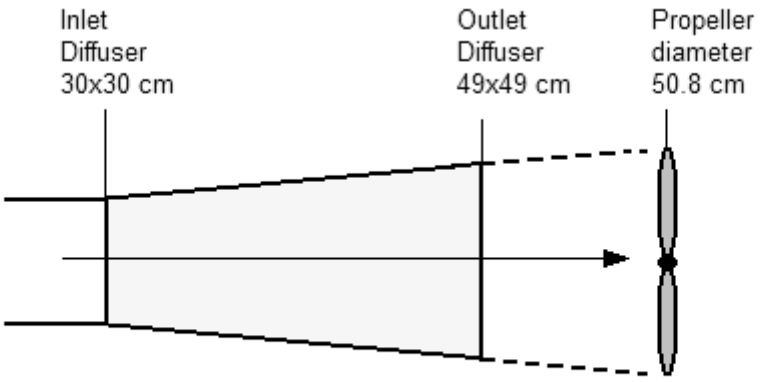

Figure 4.1 Estimating distance of propeller to diffuser outlet

Airflow over the propeller diameter

For this measurement, the propeller was not running. To get a reasonably good value for the airspeed over the propeller diameter, we measured the speed of air from the wind tunnel at different points in the cross sectional area of the propeller diameter. A pitot head was used to measure values for the area the propeller would run in. To get an adequate result of the distribution of speed over the airflow diameter, we did not measure directly at the propeller blades, as the ram pressure at the blades would falsify the measurements. Instead, we measured the speed of air at ninety degrees from both propeller blades. It was decided to take the first measurement at 50 mm away from the propeller hub, as the inner core of the propeller will not produce extensive thrust in comparison to the rest of the propeller blade. Overall, the speed of air was measured at eight points along the propeller radius. Table 4.2 and figure 4.2 show the results of a measurement for one wind tunnel setting.

Table 4.2 Airspeed along propeller radius

Measuring Point	Distance from propeller hub [mm]	Pressure [mmWg]	Pressure [Pa]	Airspeed [m/s]
1	50	15	147.33	15.81
2	80	14	137.50	15.28
3	110	11	108.04	13.54
4	140	8	78.57	11.55
5	170	5	49.11	9.13
6	200	3	29.47	7.07
7	230	2	19.64	5.77
8	255	1	9.82	4.08

Figure 4.2 Airspeed over propeller radius (propeller not running)

In figure 4.2 in can be seen that the velocity distribution is following a bell-shaped curve along the propeller diameter. The hub will experience an airflow that is nearly four times faster than the airflow at the propeller tips. This difference is unfortunately so high that it will influence the adequacy of our test results concerning the thrust.

First, the thrust produced by the outer part of the propeller is accounting for a huge part of the overall thrust. If the air stream approaching the outer part is much slower, this will result in discrepancy between the thrust measured and the thrust of the propeller flying in free atmosphere. Moreover, as can be seen in figure 3.1, a running propeller is absorbing an airflow that is larger than its own diameter. If the tips of the propeller, as in our experiment, are running outside of the fast core of the air stream, the propeller is absorbing even slower air from the outside. Both effects are visualized in figure 4.3. Very adequate results can therefore only be reached for small propellers or huge diffusers, where the air stream to propeller diameter ratio is large. In these cases, the whole propeller would be able to run in the core of the air stream and experience nearly the same airspeed.

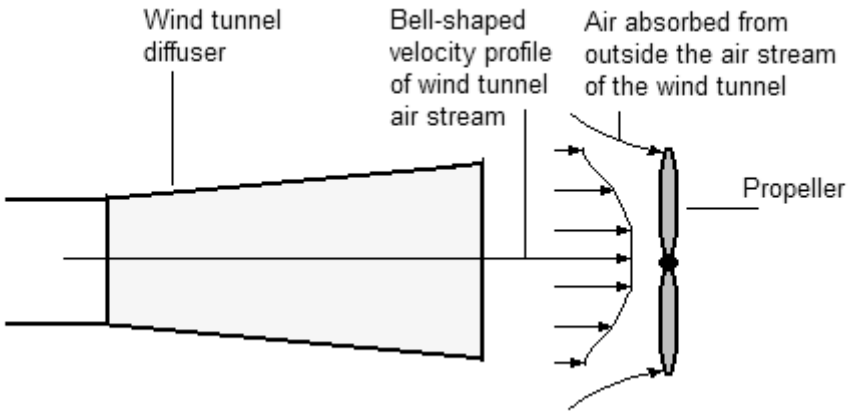

Figure 4.3 Uneven airflow advancing the propeller due to propeller size and slip stream

As with our propeller/diffuser combinations it was not possible to reach a uniform speed over the propeller diameter, we calculated the arithmetic mean of the airspeed advancing the propeller.

Drag Produced by the Wind Tunnel Air Flow

For the wind tunnel tests, the force on the load cell cannot be seen as pure thrust. The airflow against the power unit is producing form drag, which will reduce the pulling force as it is vectored in the opposite direction. The force on the load cell must then be seen as the forward force. If the load cell measurement falls to zero, the forward force falls to zero. This is when the thrust equals the drag. For example, an aircraft flying at constant speed will have the thrust equal to the drag.
Per definition, forward force is thrust minus drag. Therefore, to calculate the thrust produced by the propeller, the drag has to be determined and added to the forward force. The relationship between forward force, thrust and drag is given in the following equation.

$$F_F = T - F_D \Leftrightarrow T = F_F + F_D \tag{4.5}$$

where
F_F = forward force [N]
T = thrust [N]
F_D = drag [N]

To determine the drag produced from the wind tunnel airflow, static and wind tunnel measurements were compared. Regardless of the primary input current, after the theoretical capacity of the batteries is over, the discharge voltage falls to a constant value of about 15 to 16 V per pack. These final discharge voltages and currents are still able to turn the propeller at a small rotational rate and to produce a little thrust.For the wind tunnel test, this thrust is so little, that the airflow pushing against the power unit is compressing the load cell. This negative forward force can easily be measured for any wind tunnel air speeds. It already represents a fraction of the drag, which has to be determined. For the static test, the thrust produced by the final discharge power can be measured. This thrust is also produced while running in the wind tunnel. Combining the two measurements, the drag produced can be determined by subtracting the negative forward force from the final thrust. The thrust produced while running at higher currents can then be approximated by adding the drag to the measured forward force. It should be noted that this approach is only considered an approximation of both, the drag and the thrust. In fact, when running in an air stream, the drag on the propeller is not constant, but changing with the rotational rate.

4 Static Tests

The static tests were performed using four different input currents. At the very beginning of our experiments, a full throttle test of the Hacker A60-18M with an APC 20x10 propeller was performed. This test provided us with the first current of 37 A. The following currents were chosen to match roughly 70 per cent (25.9 A), 50 per cent (18.5 A) and 33 percent (12.2 A) of this current. As the input current could only be set by the motor's radio control, the exact adjustment was not always possible. The actual input currents of the compared measurements therefore deviate slightly from the exact target values. Still, very comparable measurements were reached. The results are discussed in detail in the following subchapters.

4.1 Test Results

Hacker A60-18M with APC 20x10 and APC 22x12W

Tables 5.1a+b, and figures 5.1a+b show the results gathered from the static tests performed with the Hacker A60-18M motor.

Table 5.1a Direct Thrust Measurement Hacker A60-18M with APC 20x10 (Static Test)

I_{in}[A]	U_{in} [V]	P_{in} [W]	Battery No.	t_{usable} [s]	$T_{average}$ [N]	n [RPM]	v_{pitch} [m/s]
37	24.65	912.05	1	120.5	52.657	5050	19.094
25.9	27.90	722.61	2	164	42.613	4640	16.416
19.65	30.10	591.47	2	258	35.903	4278	15.018
12.2	32.23	393.21	1	443.5	26.243	3700	13.018

Table 5.1b Direct Thrust Measurement Hacker A60-18M with APC 22x12W (Static Test)

I_{in}[A]	U_{in} [V]	P_{in} [W]	Battery No.	t_{usable} [s]	$T_{average}$ [N]	n [RPM]	v_{pitch} [m/s]
36.5	24.5	894.25	1	92	47.768	4100	15.716
24.8	28.3	701.84	2	129.5	46.499	3837	14.554
19.8	29.8	590.04	2	191	36.213	3606	13.459
12	33	396	1	373.5	30.165	3145	12.185

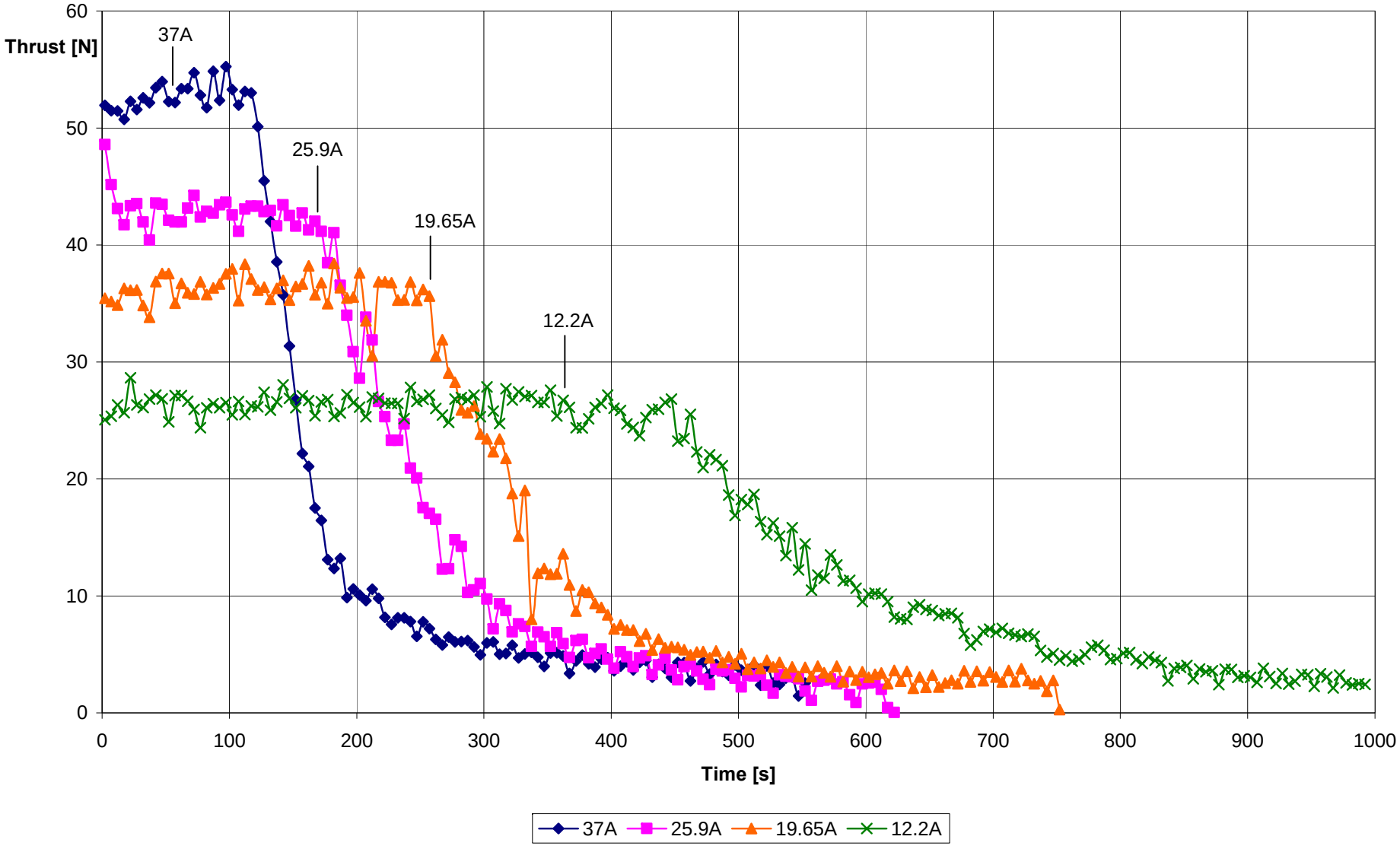

Figure 5.1a Thrust over Time – Hacker A60-18M with APC 20x10 at different Currents (Static Test)

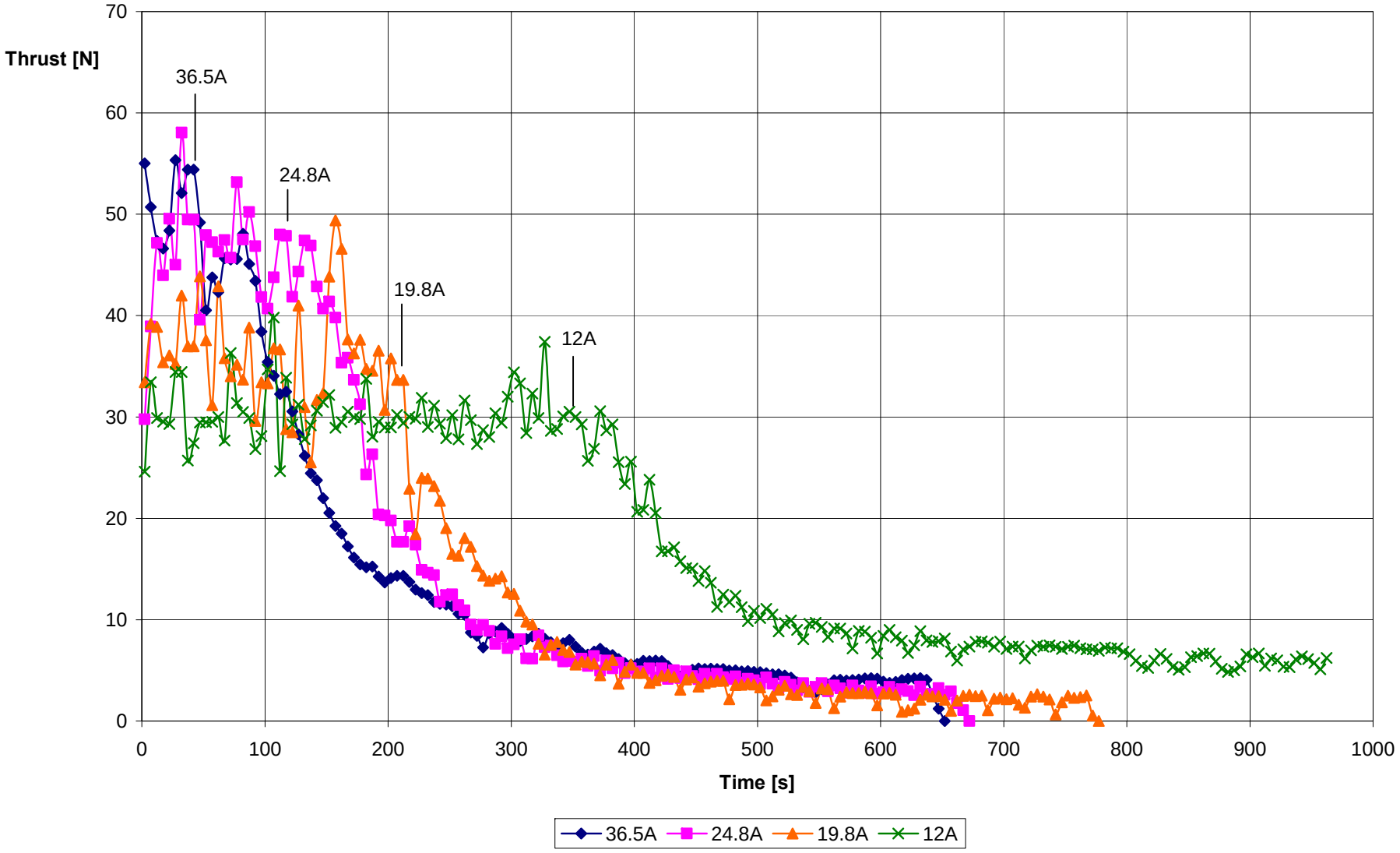

Figure 5.1b Thrust over Time – Hacker A60-18M with APC 22x12W at different Currents (Static Test)

Plettenberg HP370/50/A3 with APC 20x10 and APC 22x12W

Tables 5.2a+b, and figures 5.2a+b show the results gathered from the static tests performed with the Plettenberg HP370/50/A3 motor.

Table 5.2a Direct Thrust Measurement Plettenberg HP370/50/A3 with APC 20x10 (Static Test)

I_{in}[A]	U_{in} [V]	P_{in} [W]	Battery No.	t_{usable} [s]	$T_{average}$ [N]	n [RPM]	v_{pitch} [m/s]
39	24.00	936.00	3	94	50.093	5103	18.463
25	28.54	713.50	3	136.5	39.517	4721	16.985
20.1	30.48	612.65	1	177.5	37.177	4450	16.253
12.2	32.30	394.06	2	366	26.456	3805	13.658

Table 5.2b Direct Thrust Measurement Plettenberg HP370/50/A3 with APC 22x12W (Static Test)

I_{in}[A]	U_{in} [V]	P_{in} [W]	Battery No.	t_{usable} [s]	$T_{average}$ [N]	n [RPM]	v_{pitch} [m/s]
37.5	24.6	922.5	3	81.5	48.804	3994	14.834
25.2	28.1	708.12	3	140	43.228	3662	14.512
20.2	30.4	614.08	1	177.5	41.764	3514	13.652
12.2	32.18	392.6	2	347	30.092	2941	12.014

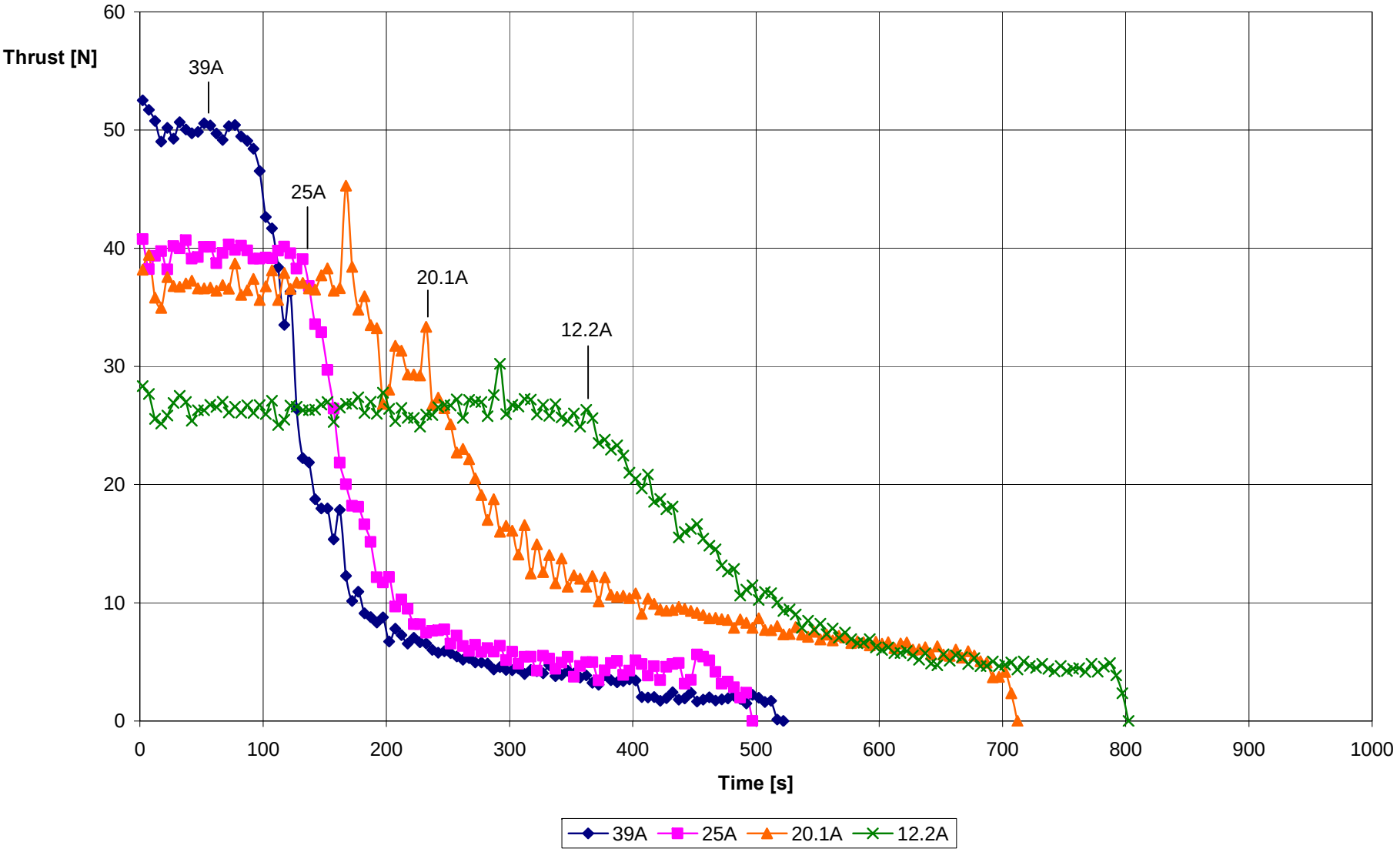

Figure 5.2a Thrust over Time – Plettenberg HP370/50/A3 with APC 20x10 at different Currents (Static Test)

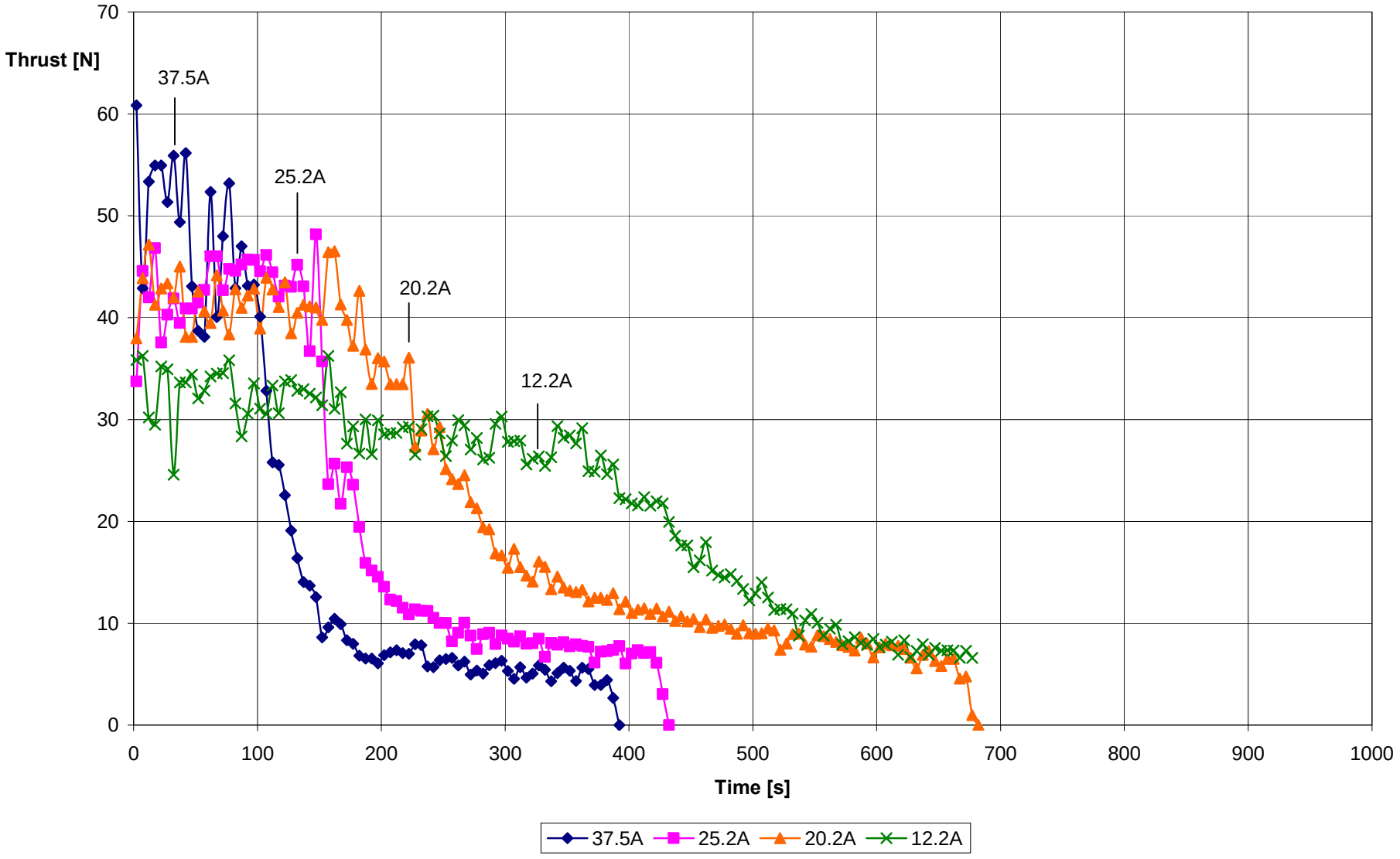

Figure 5.2b Thrust over Time – Plettenberg HP370/50/A3 with APC 22x12W at different Currents (Static Test)

4.2 Thrust at different power settings

Input Power

The power input is defined as the product of input current and input voltage. As described in detail in chapter 3.4, the discharge voltage of a battery is not constant and must be seen as a function of the discharge current. As the tests were performed with relatively high discharge currents, the nominal discharge voltage of 1.2 V per cell was not reached. Tables 5.1a through 5.2b show the drop in voltage with higher discharge currents. An increase in current from 20 A to 37 A will result in a decrease of more than 5.0 V. Combining the results of the static tests with fully charged batteries, the relationship between the discharge voltage and the current draw can be approximated as being linear. It is visualized in figure 5.3. The trend is given by the following equation.

$$U = -0.3178 \cdot I + 36.351 \tag{5.1}$$

where
U = Discharge Voltage [V]
I = Discharge Current [A]

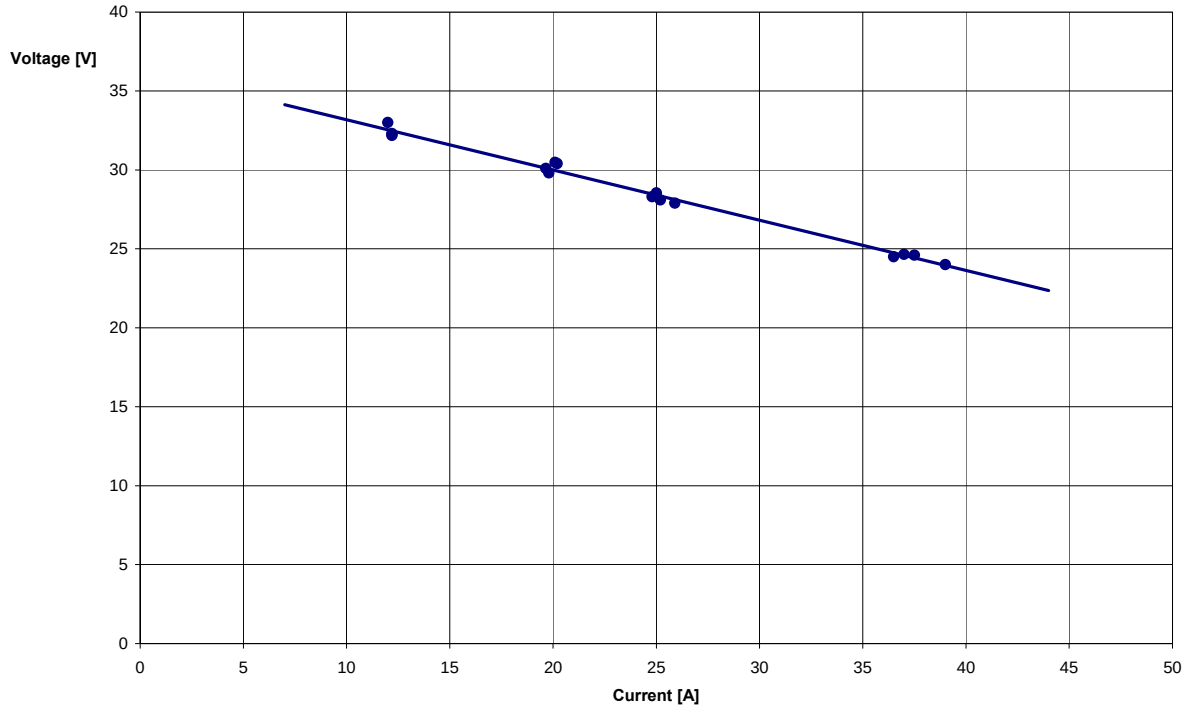

Figure 5.3 Discharge Voltage over Discharge Current – Experimental (Fully charged batteries)

This significant drop of voltage at higher current draws is the reason for the input power not to increase linearly with higher currents. A doubled current will therefore not result in a

doubled power input. Anyhow, as the voltage decreases slower than the current increases, a higher current will result in a higher power input.

The discharge current of the batteries equals the armature current I_a of the motor. As described in chapter 3.2, a higher armature current will result in a larger torque. If the propeller remains the same, a larger discharge current will therefore result in a higher rotational rate n. A higher rotational rate increases the angle and the velocity of the air entering the propeller and hence generates a larger lift on the propeller blades. The thrust will increase until the propeller meets its stall speed, where the angle of attack at the propeller blades becomes too large to produce further lift.

Comparison of Average Thrust

The motors in our experiments showed different efficiencies in transforming power input into thrust output in the way described above. Figure 5.4 shows the average thrust produced at different power inputs for the different combinations. As can be seen, equipped with the smaller propeller APC 20x10, both motors follow nearly the same linear increase at low power input. The two thrust measurements with higher input power are significantly dominated by the Hacker A60-18M. Whereas it continues to follow the same linear increase for the thrust output, the curve of the Plettenberg motor drops nearly 3.0 N behind.

For the larger APC 22x12W, the thrust values of the two motors are similar only for the lowest power input at 12.2 A. The Plettenberg motor then seems to follow a curve similar to the one with the smaller propeller. Again, the thrust increase between the lowest and second lowest power input cannot be maintained for the higher power inputs.

The thrust produced by the Hacker motor is inferior at the second lowest power input, but shows the highest value of all combinations at a power input of 700 W. Surprisingly, the thrust produced at the highest input power is below all other combinations. Anyhow, superiority of the large propeller at lower power inputs and of the small propeller at higher power inputs is observable.

Comparison of Thrust Fluctuations

It is necessary also to pay special attention to the amplitude of the thrust fluctuations for the different propeller combinations. Figures 5.1a through 5.2b show the thrust measurements over time for the different combinations. The thrust fluctuations around the mean value for the larger propeller have significantly higher amplitudes than the ones for the small propeller. The thrust values are reasonably stable for low input power. The higher the input power, the wider the bandwidth of the fluctuations. Moreover, the amplitudes for the tests on the Hacker motor

are significantly higher. It should be noted that the thrust curves given in figures 5.1a through 5.2b are already smoothed. One point in the curve stands for the mean of actually ten measurement points. The large difference in thrust dispersion between the propellers can be observed more clearly in figure 5.5. As can be seen, the thrust recorded at 37 A with the APC 22x12W fluctuates between 0.0 lb (0.0 N) and 20 lb (89 N).

In all cases, large fluctuation falls together with relatively low average thrust values. This suggests that a smoothly running propeller is more effective in producing thrust. Additionally, the fact that the large propeller was beating the air heavily at high power settings could be a sign that the propeller was running too fast and therefore off-design.

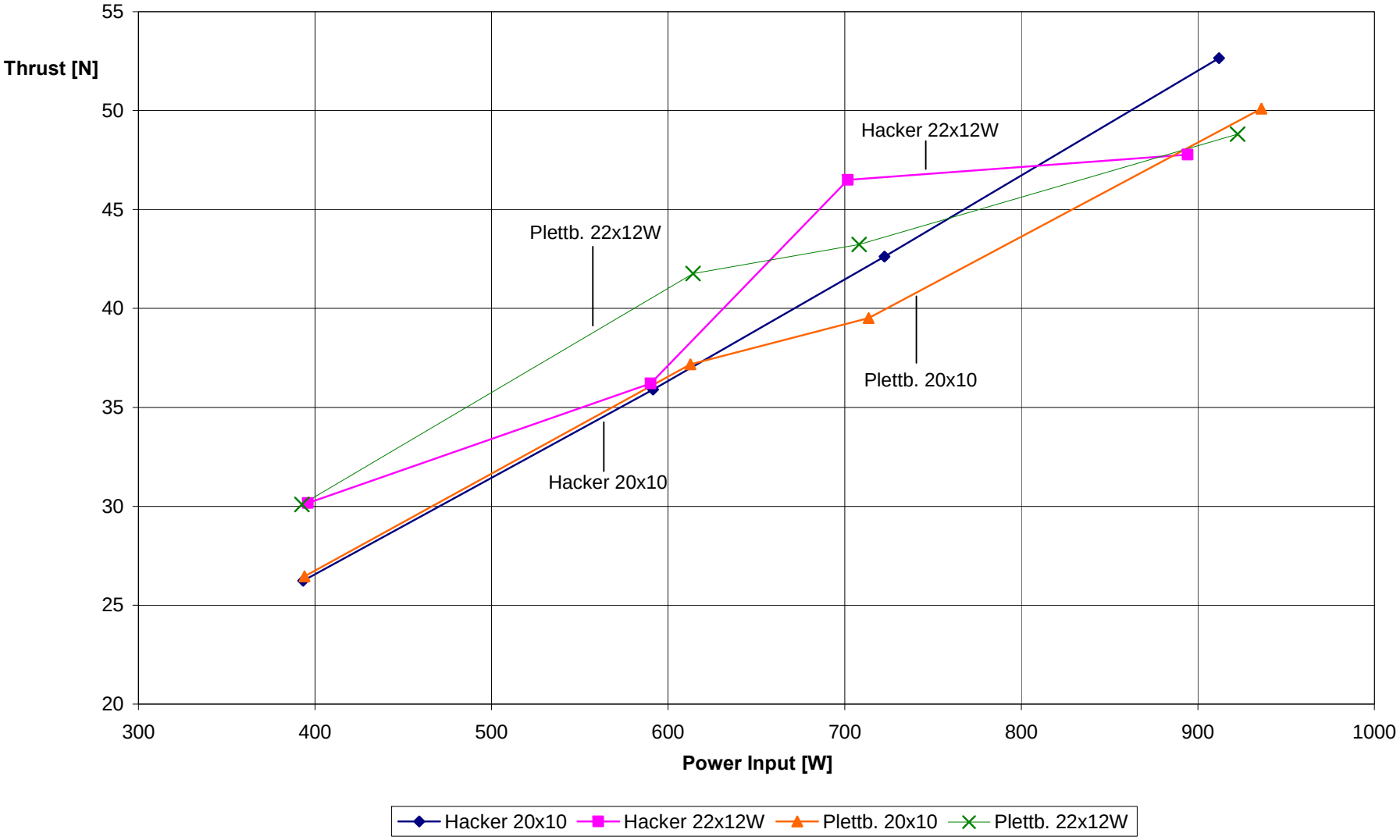

Figure 5.4 Thrust over Power Input – Hacker A60-18M vs. Plettenberg HP370/50/A3 with Propellers APC 20x10 and APC 22x12W (Static Test)

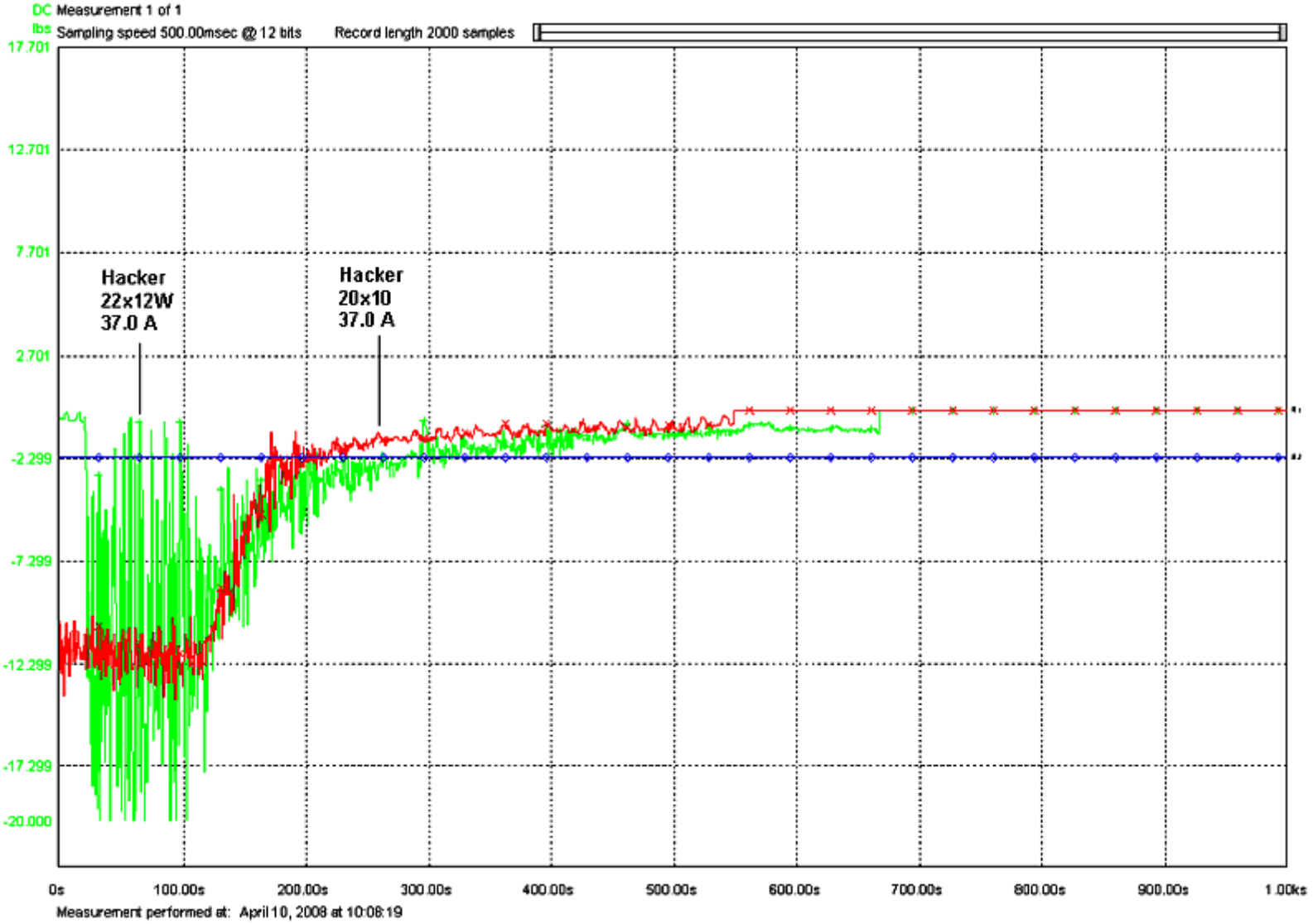

Figure 5.5 Thrust Measurement Hacker A60-18M with APC 22x12W (Static Test) – Handyscope Transient Recorder Hardcopy

4.3 Comparison to Thrust Estimates with Computer Software

Software Suitability

As already mentioned in chapter 3.5, the *Propeller Selector* software is based on experimental data of tests performed by the NACA in the late 1930s. The NACA tested two-, three- and four-bladed propellers at blade angles of 15°, 25°, 35° and 45° degrees. With equation (3.7), the blade angle of the propeller blades used for our experiments can be calculated. The blade angle of the APC 20x10 propeller was calculated to 11.98°, the blade angle of the APC 22x12W propeller was calculated to 13.03°. These blade angles do not exactly match the blade angles tested by the NACA, but can still be used as input for the *Propeller Selector*. It can therefore be assumed that the software has to extrapolate the experimental data. The same assumption applies to the input of flight speed. It can be set to zero even the NACA research did not include static testing.

Thrust estimates cannot be gained entirely without using actual test measurements. The *Propeller Selector* needs the revolutions per unit time as input to calculate the thrust produced. According to their usual definitions (see chapter 3.3), the *Propeller Selector* cannot produce results for propeller efficiency and power output if the air speed is set to zero.

Contrasting Test Data and Software Estimates

Thrust estimates were gained by setting the air speed to zero and using the actual measurements of the propeller's rotational rate. Table 5.3 contrasts the thrust estimates calculated from these inputs and the direct thrust measurements, which is the pulling force on the load cell. Furthermore, it contains the software estimate of the power absorbed by the propeller. The power absorbed is the power input of the shaft to the propeller. Not all of this power can be converted into thrust. The power output of the propeller is the air speed multiplied by the thrust produced. As mentioned above, the power output falls to zero in static tests. The Propeller Selector software shows warning signs if the calculations estimate the propeller being close to stall at the given inputs. Table 5.3 indicates if these warning signs emerged. Figure 5.6 visualizes the measured thrust values and the thrust estimates by the software.

Table 5.3 Measured Thrust and Estimated Thrust at different Currents – Hacker A60-18M vs. Plettenberg HP370/50/A3 with Propellers APC 20x10 and APC 22x12W (Static Test)

Test	I_{in}[A]	P_{in} [W]	n [RPM]	$T_{average}$ [N] measured	$T_{average}$ [N] estimated	Deviation [%]	$P_{absorbed}$ [W] estimated
Hacker 20x10	37.00	912.05	5050	52.657	47.842	-9.14%	804.35
Hacker 20x10	25.90	722.61	4640	42.613	40.389	-5.22%	623.92
Hacker 20x10	19.65	591.47	4278	35.903	34.333	-4.37%	488.99
Hacker 20x10	12.20	393.21	3700	26.243	25.682	-2.14%	316.36
Hacker 22x12W	36.50	894.25	4100	47.768	48.908*	2.39%	772.82
Hacker 22x12W	24.80	701.84	3837	46.499	42.835*	-7.88%	633.43
Hacker 22x12W	19.80	590.04	3606	36.213	37.832*	4.47%	525.78
Hacker 22x12W	12.00	396	3145	30.165	28.778*	-4.60%	348.81
Plettb. 20x10	39.00	936	5103	50.093	48.851	-2.48%	829.95
Plettb. 20x10	25.00	713.5	4721	39.517	41.811	5.81%	657.17
Plettb. 20x10	20.10	612.65	4450	37.177	37.149	-0.08%	550.37
Plettb. 20x10	12.20	394.06	3805	26.456	27.160	2.66%	344.06
Plettb. 22x12W	37.50	922.5	3994	48.804	46.412*	-4.90%	714.41
Plettb. 22x12W	25.20	708.12	3662	43.228	39.017*	-9.74%	550.65
Plettb. 22x12W	20.20	614.08	3514	41.764	35.927*	-13.98%	486.55
Plettb. 22x12W	12.20	392.6	2941	30.092	25.165*	-16.37%	285.24

*Software indicated propeller approaching stall conditions

Accuracy of thrust estimates for the 20x10 propeller

The estimated thrust values for the smaller propeller are reasonably good, especially for the lower input powers and rotational rates. The actual measured values for the Hacker motor are rising more steeply than the estimated thrust values.

One value on the Plettenberg curve is anomalously off the estimated thrust curve. The reason for this is not clear. However, as the other measurements seem to be following a steady curve, the measurement could be faulty. In average, the software is estimating thrust values that are below the actual measured thrust. The deviation averages out at -1.87 per cent for the estimated values.

Accuracy of thrust estimates for the 22x12W propeller

For the 22x12W propeller the estimates are not as close to the measured thrust. It should be noted that for the 22x12 propeller at zero air speed, warning signs, estimating the propeller being close to stall, emerged at any rotational speed. Not until the air speed was raised, the warning signs disappeared. According to the *Propeller Selector* help file, the output values

shown at this stage are what they would be if the propeller runs unstalled and thus do not represent the actual performance of the propeller. Additionally, the software does not provide an input for uncommon propeller design. The ‘wide-blade’ 22x12W propeller was therefore calculated as a regular 22x12 propeller.

However, the estimate of a possible propeller stall does not seem unlikely, especially when observing the thrust curve of the Hacker motor. For the two higher rotational rates, the curve is flattening. This could indicate a thrust peek, which is followed by a propeller stall at higher rotational speed. Large thrust fluctuations, mentioned already in chapter 5.2, and the propeller beating the air heavily, support the assumption of a propeller running off-design.

Admittedly, the Plettenberg curve is inconsistent with the theory of a propeller stall. Especially at low rotational rates, the Plettenberg motor was producing much higher thrust than estimated. And the thrust seems to be constantly rising, even if the slope is less steep for higher speeds. It almost looks as if the measurement curve converges towards the estimated values. To put it concisely, it is unclear why the measured thrust values of one motor are so far off the values of the other. Theoretically, the same propeller running at a certain rotational speed should produce the same thrust albeit the motor. Motor constants, as for example the motor efficiency, are generally not of importance, as the same rotational rate means that the propeller is driven by the same shaft power. If an overloading of the Hacker motor with the large propeller and a high power input caused the thrust to destabilize cannot be answered at this stage.

The estimated values for the larger propeller deviate 6.33 per cent down in average. The highest deviations can be found for the Plettenberg motor at lower rotational speeds.

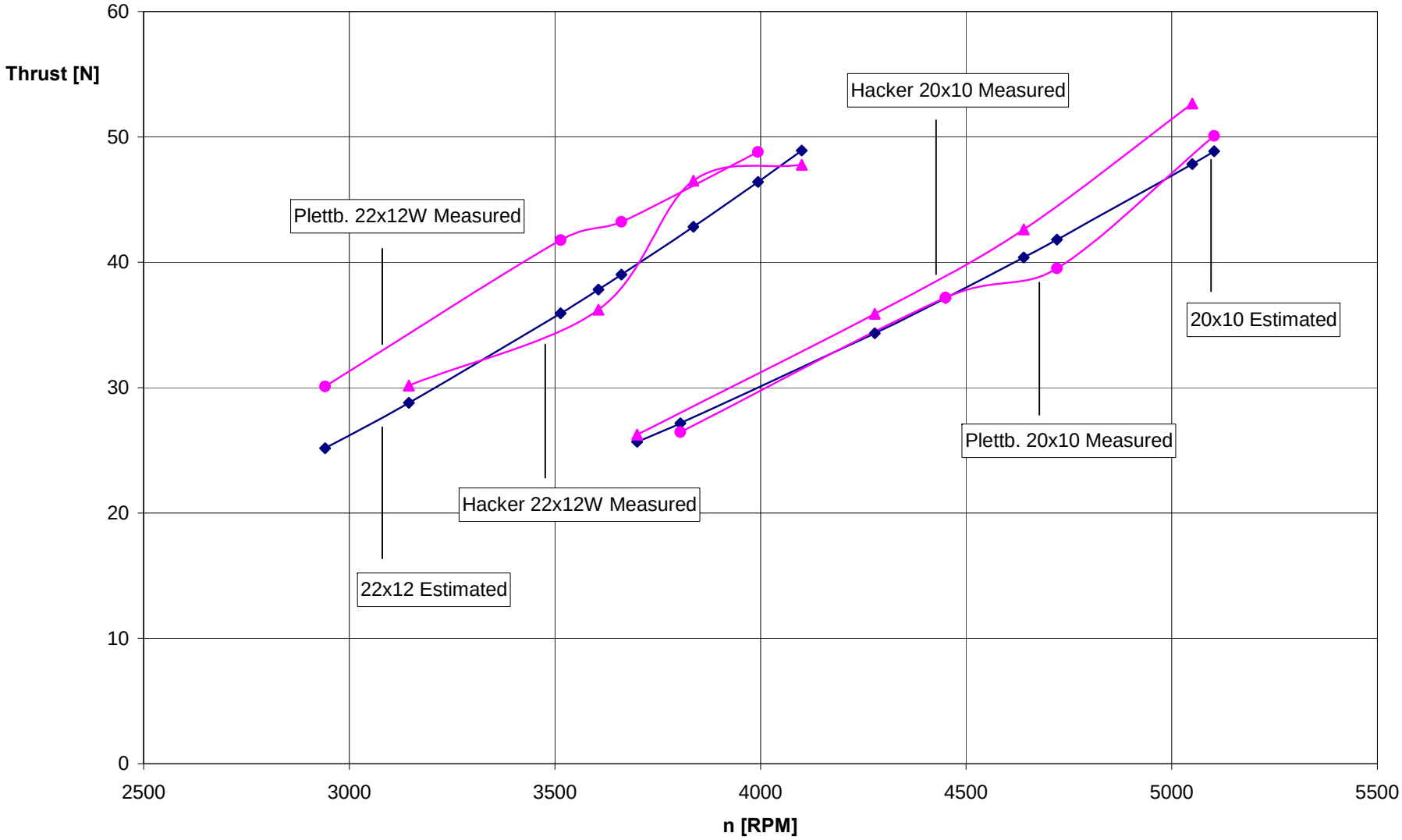

Figure 5.6 Thrust over Rotations per unit time – Propeller Selector Estimates vs. Direct Measurements (Static Test)

4.4 Usable Running Time at different Power Settings

Comparison to Battery Discharge Theory

The usable running time was calculated using the start and end conditions described in chapter 4.4. As can be seen in figure 5.7a, the time the motor-propeller-battery combination was able to produce constant thrust was significantly decreasing with higher current draw.

The usable running time is closely linked to the capacity of the battery packs. Both are functions of the discharge voltage. The basis for the calculation of usable running time, the thrust, is dependent on a constant input power, which is the product of discharge current and voltage. It is still important to differentiate, as their definitions are different. Whereas capacity is calculated to an end voltage (per cell) of 1.0 V, the usable running is calculated to a thrust reduction of 5 per cent. As seen in the foregoing chapter, the discharge voltage drops with higher currents. Depending on the current drawn, the voltage will reach the capacity calculation limit of 1.0 V before or after the usable running reaches its end condition. As can be seen below, the voltage can be so radically depressed by high currents that a calculation of capacity is not even possible.

However, comparing the thrust graphs from figures 5.1a through 5.2b with the discharge voltage graphs given by **GP 2006** in chapter 3.4, one will note their similarity. A reasonably constant power output is followed by a sudden drop in voltage (figure 3.7) and thrust (figure 5.1a- 5.2b). It is important to realize that the graphs, which are most comparable to the battery discharge theory in figure 3.7, are the graphs for the lower discharge currents, especially for the discharge current of 12.2 A. Very high discharge currents are not intended by battery manufacturers, and a maximum of 3.0 C is recommended. In the experiments discussed, we were discharging the batteries at much higher C rates. Table 5.4 is providing information about the applied discharge currents I_{in}, the nominal battery capacity C_n, the resulting C rate and discharge voltage U_{in}, and the calculated usable running time t_{usable}. Equation (3.10b) was used to calculate C_n. As can be seen in table 5.4, even the lowest applied discharge rate of 12.0 A is equivalent to a C rate of 5.45 and therefore exceeds the recommended maximum C rate by 2.45.

When realizing the difference of the C rate recommended by manufacturers and the C rate used to produce enough thrust for a model airplane, the loss in running time with higher currents becomes understandable. The theory of battery discharge and figure 5.7a suggests running the motors with currents as low as possible. With lowering the discharge current, the usable running time is increasing almost exponentially. One should also recall the fact that not only the running time but also the discharge voltage is increasing. In average, with reducing the current from 37 A to 12.2 A, the running time can be quadrupled, where the thrust is reduced only by about 40-50 per cent.

Table 5.4 Usable Running Time at different Currents – Hacker A60-18M vs. Plettenberg HP370/50/A3 with Propellers APC 20x10 and APC 22x12W (Static Test)

Test	I_{in}[A]	C_n [Ah]	C rate	U_{in} (Pack) [V]	U_{in} (Cell) [V]	t_{usable} [s]
Hacker 20x10	37.00	2.2	17.72	24.65	0.88	120.5
Hacker 20x10	25.90	2.2	11.36	27.90	1.00	164
Hacker 20x10	19.65	2.2	9.14	30.10	1.08	258
Hacker 20x10	12.20	2.2	5.55	32.23	1.15	443.5
Hacker 22x12W	36.50	2.2	16.59	24.50	0.88	92.0
Hacker 22x12W	24.80	2.2	11.27	28.30	1.01	129.5
Hacker 22x12W	19.80	2.2	9.00	29.80	1.06	191.0
Hacker 22x12W	12.00	2.2	5.45	33.00	1.18	373.5
Plettb. 20x10	39.00	2.2	17.73	24.00	0.86	94.0
Plettb. 20x10	25.00	2.2	11.36	28.54	1.02	136.5
Plettb. 20x10	20.10	2.2	9.14	30.48	1.09	177.5
Plettb. 20x10	12.20	2.2	5.55	32.30	1.15	366.0
Plettb. 22x12W	37.50	2.2	17.05	24.60	0.88	81.5
Plettb. 22x12W	25.20	2.2	11.45	28.10	1.00	140.0
Plettb. 22x12W	20.20	2.2	9.18	30.40	1.09	177.5
Plettb. 22x12W	12.20	2.2	5.55	32.18	1.15	347.0

Superiority of the Hacker-APC 20x10 combination

Figure 5.7a can be mainly divided into two sections, the curve given by the results of the Hacker motor running with a small propeller (Hacker 20x10) and the curves of the three other tests, which are all very similar. At all discharge currents, the usable running time of the Hacker A60-18M equipped with the APC 20x10 propeller is above all others. The reason for this is unclear, as the running time should mainly be influenced by the current draw as mentioned above.

There is probably a connection between these results and the very smooth thrust curves and the following decline in figure 5.1a, which is steeper than for the other motor-propeller combinations. It is therefore possible that the start and end conditions for the calculation of the usable running time could have be influenced, as they are functions of the stability and smoothness of the thrust curve. Other explanations could be found in the use of different battery packs and the inability to control the current exactly with the radio control. A slightly higher current and the use of an inferior battery pack could already have affected the running time adversely. Anyhow, the absolute superiority in running time of one combination needs more investigation. The possible reasons mentioned above do not fully explain a mean minus deviation of 23 per cent in running time for the remaining tests.

Using the Results to predict Usable Running Time

As mentioned above, the calculated usable running time for the three other combinations fall below these values and follow very similar curves. A graphical approach to predict usable running times at certain current draws and battery capacities of 2200 mAh can therefore be established on these results. A curve running through the worst results (shortest running time) reached for each current can then be used, as shown in figure 5.7b. It should be noted that the results presented here are calculations of start and end conditions that are highly affected by the amount and magnitude of thrust fluctuations. A well-matched combination, producing a smooth thrust curve, could possibly reach longer running times, as shown by the Hacker motor equipped with the smaller propeller.

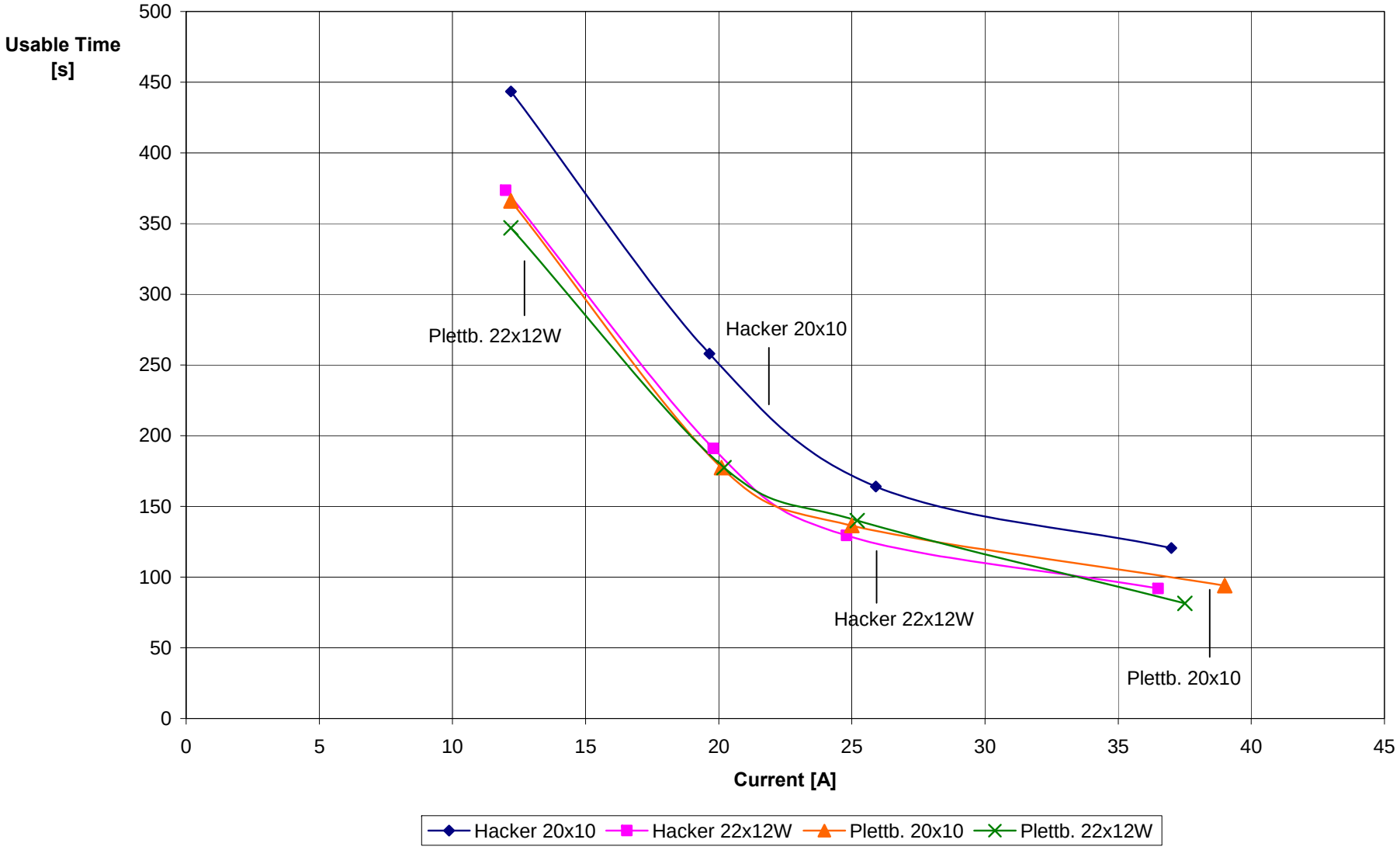

Figure 5.7a Usable Running Time over Current – Hacker A60-18M vs. Plettenberg HP370/50/A3 with Propellers APC 20x10 and APC 22x12W (Static Test)

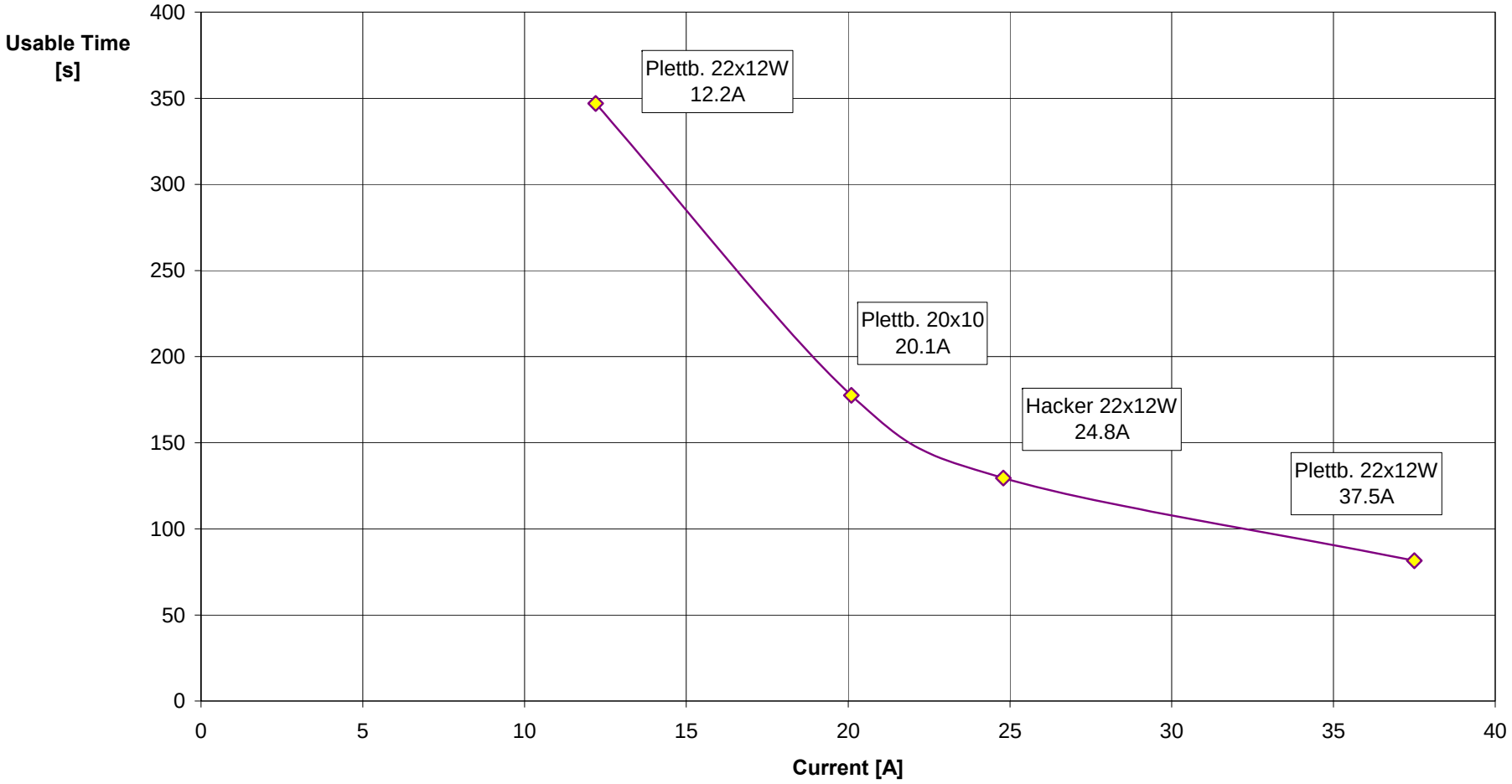

Figure 5.7b Graphical Approach for estimating Usable Running Time – For Battery Capacities of 2200 mAh – Experimental (Static Test)

4.5 The Effect of Battery Storage on Running Time

Not using a battery short after charge and storing it instead will decrease its capacity due to an effect called self-discharge. This effect is described in more detail in chapter 3.4. The discharge is then a function of storage time and temperature, a higher temperature causing a faster discharge. As can be seen in figure 5.8, it is helpful to store battery packs at 0 °C, as the self-discharge is then reduced to a minimum.

It happened accidentally in our testing routine that the battery packs were once fully charged and could then not be used for two weeks. This gave us the chance to observe the effect of self-discharge on the usable running time of a model aircraft power unit. The batteries for this experiment were stored 14 days at 20 °C. The thrust curve was recorded as usual and the usable running time was calculated using equations 4.4a and 4.4b. The usable running time of the self-discharged batteries was then compared to the result of the same combination using freshly charged batteries. Results of this experiment are registered in table 5.5. The loss in usable running time over storage time is visualized in figure 5.9.

Table 5.5 Fully charged Battery vs. 14 days stored Battery – Plettenberg HP370/50/A3 with Propeller APC 20x10 (Static Test)

I_{in}[A]	U_{in} [V]	P_{in} [W]	Battery No.	$t_{storage}$ [days]	t_{usable} [s]	t_{usable} [%]	$T_{average}$ [N]	n [RPM]	v_{pitch} [m/s]
25	28.54	713.50	3	-	136.5	100%	39.517	4721	16.985
20.1	30.48	612.65	1	-	177.5	100%	37.177	4450	16.253
12.2	32.30	394.06	2	-	366	100%	26.456	3805	13.658
25.9	27.9	722.61	3	14	131	95.97%	41.647	4798	16.964
20	29.5	590	1	14	142.5	82.82%	36.581	4533	15.968
12.2	31.4	383.08	2	14	255	69.95%	27.593	3897	13.754

Comparing the result in table 5.5, the per cent loss in running time seems to increase with decreasing input power. At an input current of 12.2 A, the usable running time is more than 100 s shorter after the 14 days storage. As against an input current of 25.9 A results in a rather small loss of 4 per cent.

Our results support the self-discharge graph given by Linden (1995). Comparing figures 5.8 and 5.9, one can identify the similarities. Anyhow, regarding small current draws, the loss in running time is larger than expected. This could have reason in the difference between the definitions of running time and capacity. Other possible explanations could be found in the high discharge C rates and storing temperatures slightly varying from 20 °C. When closely observing table 5.5, one will note that in comparison to the loss in usable running time, the average thrust seems to remain about the same. Figures 5.10a and 5.10b show the thrust recordings for 20 A and 12 A with freshly charged and stored batteries. As can be seen, a

model aircraft equipped with stored batteries is therefore likely to have the same propeller performance, while its flight time will be highly reduced.

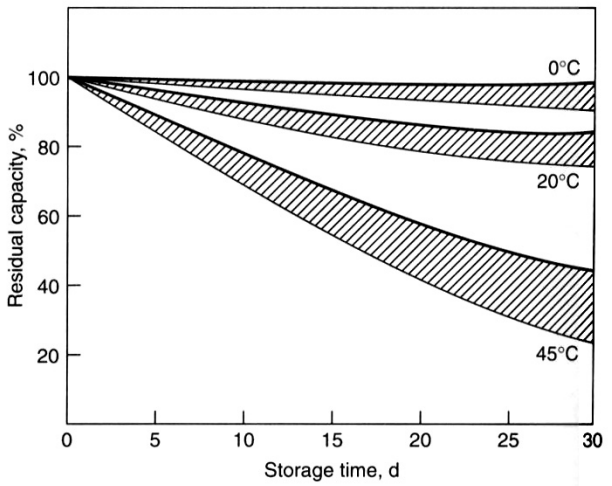

Figure 5.8 Theory: Capacity vs. Storage time and temperature (Linden 1995)

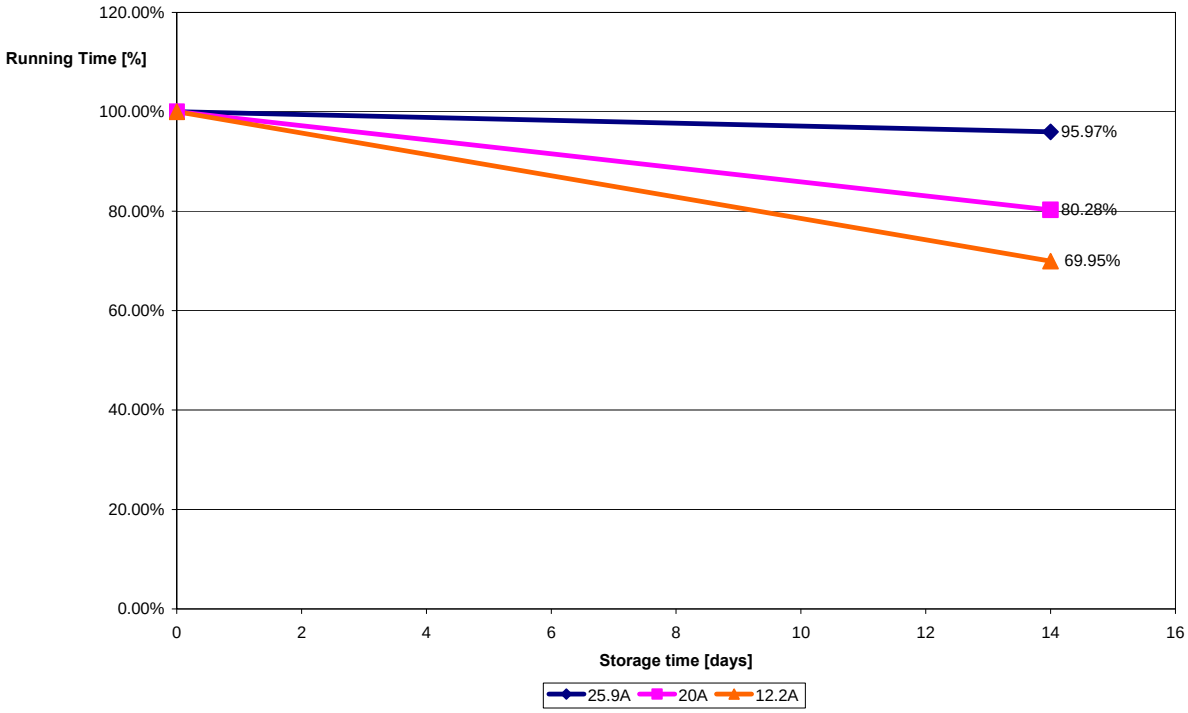

Figure 5.9 Useable Running Time over Storage Time at 20 °C (Static Test)

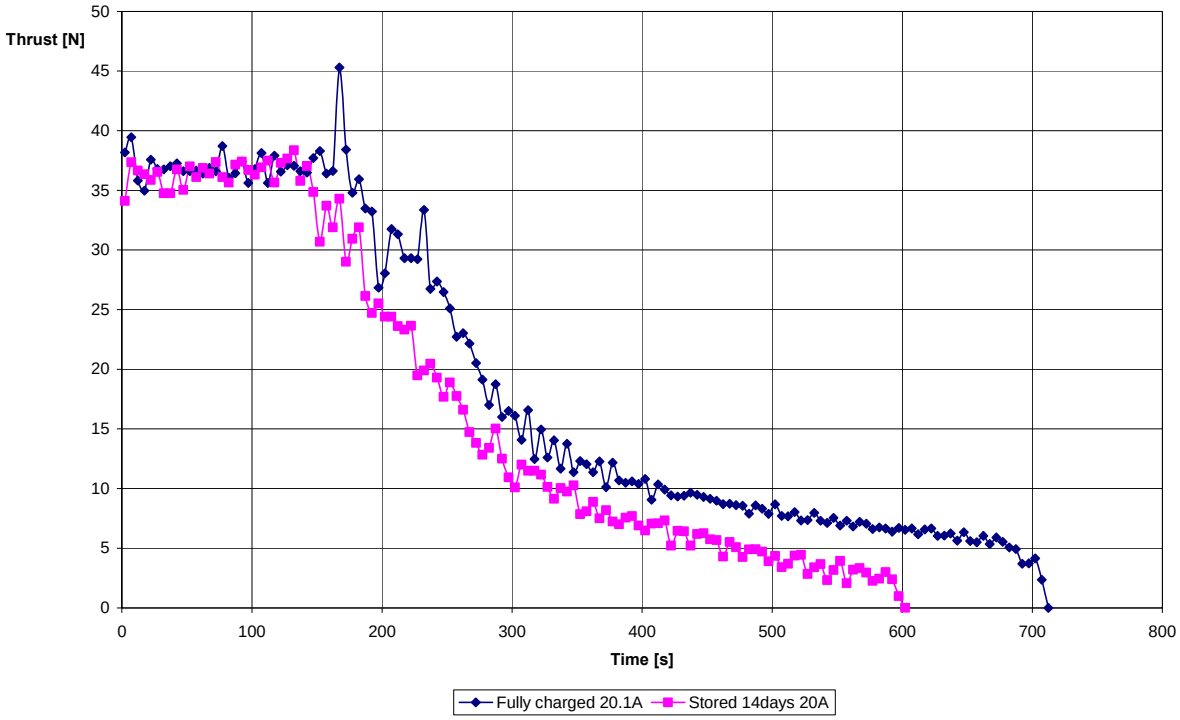

Figure 5.10a Fully charged Battery vs. 14 days stored Battery at ca. 20 A (Static Test)

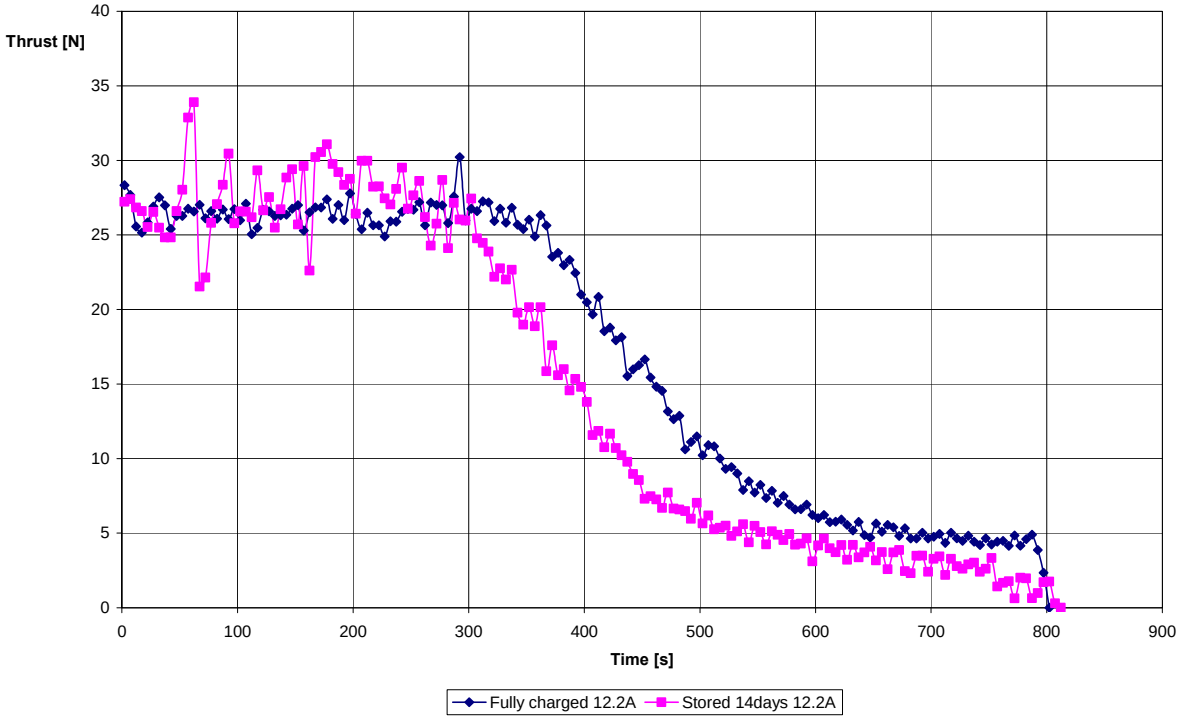

Figure 5.10b Fully charged Battery vs. 14 days stored Battery at 12.2 A (Static Test)

5 Wind Tunnel Tests

The wind tunnel tests were performed at the Eiffel wind tunnel of the Lonsdale Building at the University of Limerick. The air speed over the propeller diameter was measured as described in chapter 4.4. As a uniform airspeed over the diameter could not be reached, the arithmetic mean was calculated and used as the overall airspeed.

All wind tunnel tests were performed with the Hacker A60-18M and an APC 20x10 propeller. The tests were performed controlling the input current. The currents used were the same as for the static tests. However, it was decided not to test at the highest current of 37 A, as the short running time makes observations and comparisons more difficult.

5.1 Determining Drag and Thrust

Figure 6.1a shows the load cell measurements gained from the wind tunnel tests at 10.28 ms^{-1}. Figure 6.1b contrasts load cell measurements at different velocities. It includes the measurement from the wind tunnel test at 6.66 ms^{-1}. The curves for the forward force in both figures can roughly be divided into two sections. A section above and a section below zero forward force. Positive values result from the load cell being pulled, whereas it is compressed for negative values. If the thrust is too low, the power unit is pushed back instead of pulling on the load cell.

The graphs in figure 6.1a are highly superposed between 450 s and 550 s. For this period, the motor-propeller combination was pushed back by nearly the same force for all power settings. At this stage, the discharge current and voltage were at their minimum. The propeller was still turning and producing a small thrust. This thrust can be approximated from the thrust produced in the static test, when the propeller was running at about the same rotational rates short before terminating.

As explained in chapter 4.4, drag can be determined by subtracting the negative forward force from the thrust measurement in the static test. This approach is visualized in figure 6.2. (Note that figure 6.2 is combined from several measurements and that the time axis therefore is not the sample time as for the other figures.) The resulting values of drag and thrust in comparison with the static tests are shown in table 6.1. Figures 6.3a and 6.3b show the resulting curves for thrust over time.

Table 6.1 Forward Force, Drag and Thrust – Hacker A60-18M with APC 20x10 (Static Test vs. Wind Tunnel Test)

v_{air} [m/s]	I_{in} [A]	U_{in} [V]	P_{in} [W]	Battery No.	t_{usable} [s]	$F_{forward}$ [N]	F_{Drag} [N]	$T_{average}$ [N]	n [RPM]	v_{pitch} [m/s]	Δv [m/s]
0.00	25.9	27.90	722.61	2	164	42.613	0.0	42.613	4640	16.416	16.416
0.00	19.65	30.10	591.47	2	258	35.903	0.0	35.903	4278	15.018	15.018
0.00	12.2	32.23	393.21	1	443.5	26.243	0.0	26.243	3700	13.018	13.018
6.66	19.8	29.89	591.82	3	177.5	20.474	8.240	28.714	4523	18.090	11.430
10.28	25.8	27.52	703.11	1	119.0	24.422	9.228	33.650	4837	20.378	10.098
10.28	19.6	29.44	577.10	2	182.5	14.381	9.228	23.609	4538	19.550	9.270
10.28	12.05	31.57	380.37	3	303.5	5.926	9.228	15.154	3953	17.596	7.316

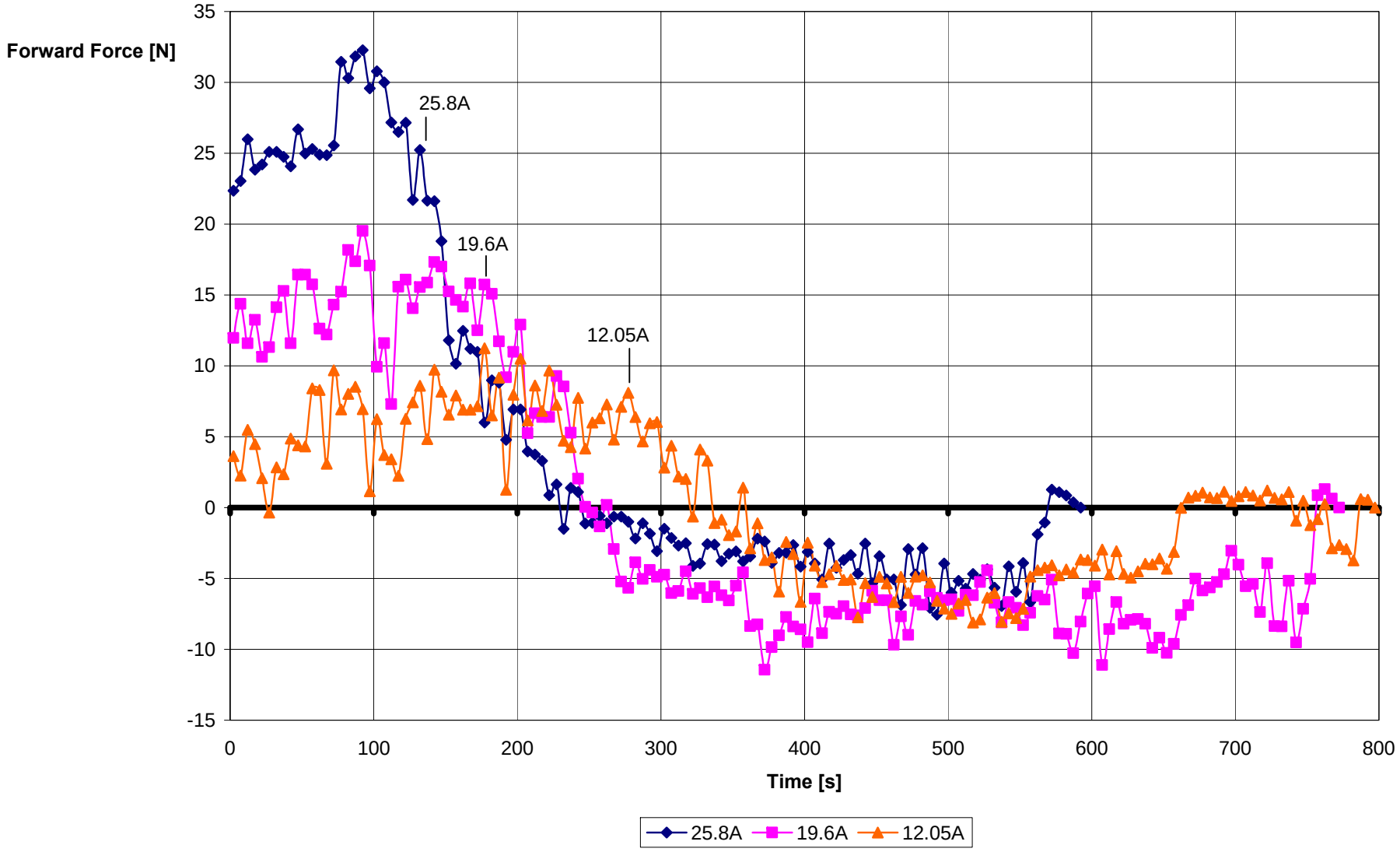

Figure 6.1a Forward Force over Time at different Current – Hacker A60-18M with Propeller APC 20x10 at 10.28 ms-1 (Wind Tunnel Test)

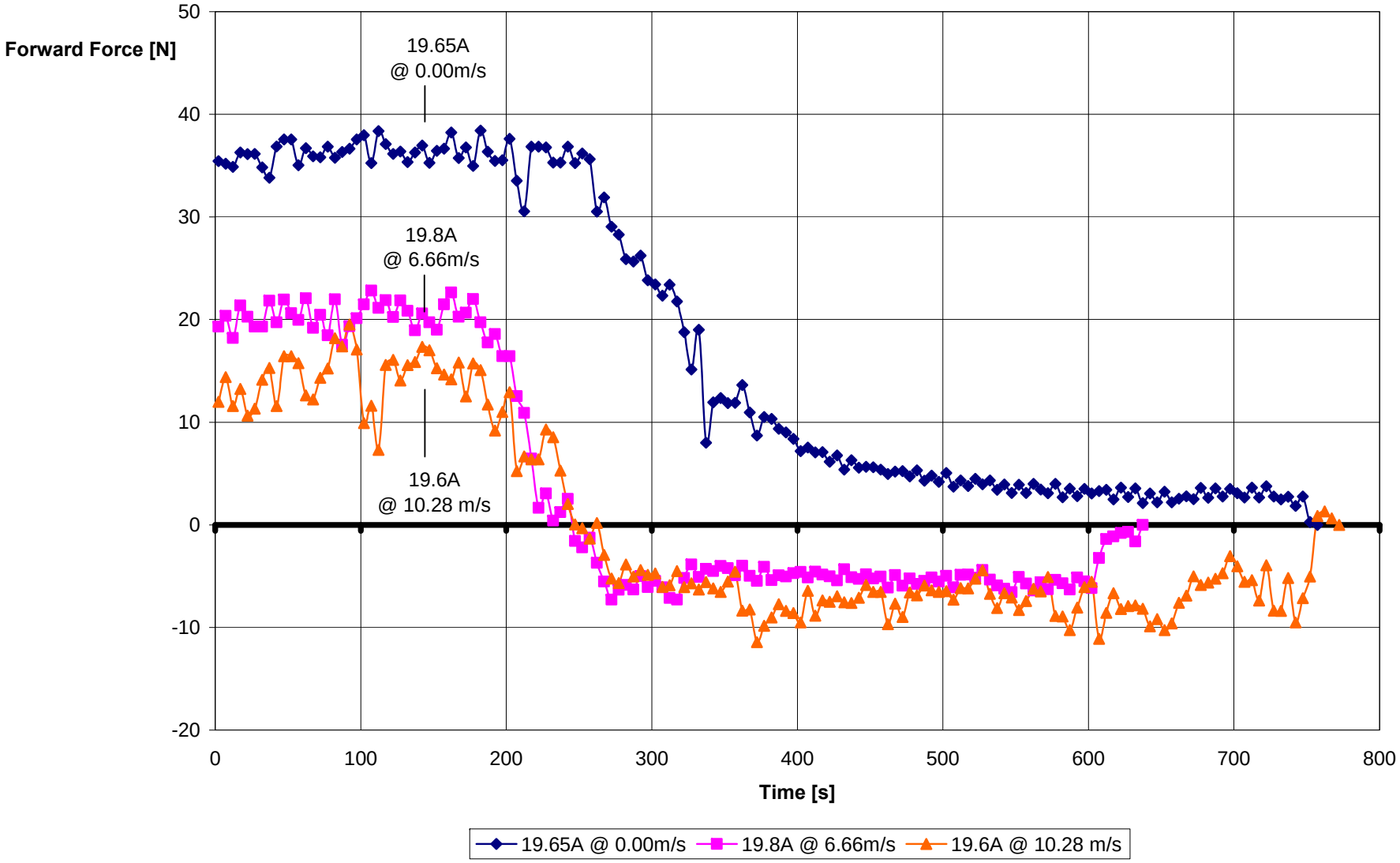

Figure 6.1b Forward Force over Time at different Air Speed – Hacker A60-18M with APC 20x10 at ca. 19.6 A (Static and Wind Tunnel Test)

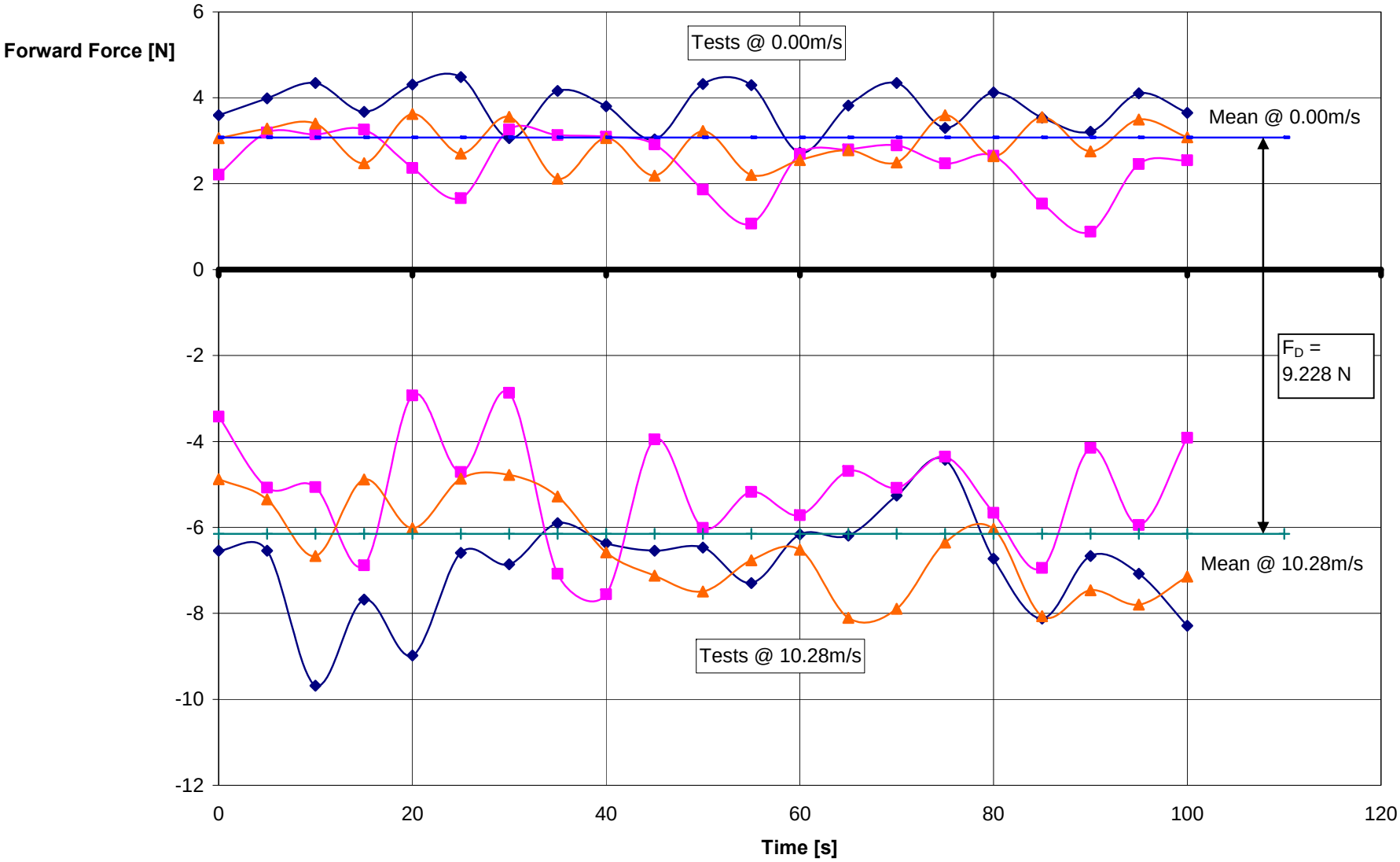

Figure 6.2 Determining Drag – Static Test vs. Wind Tunnel Test at 10.28 ms^{-1} – Hacker A60-18M with APC 20x10

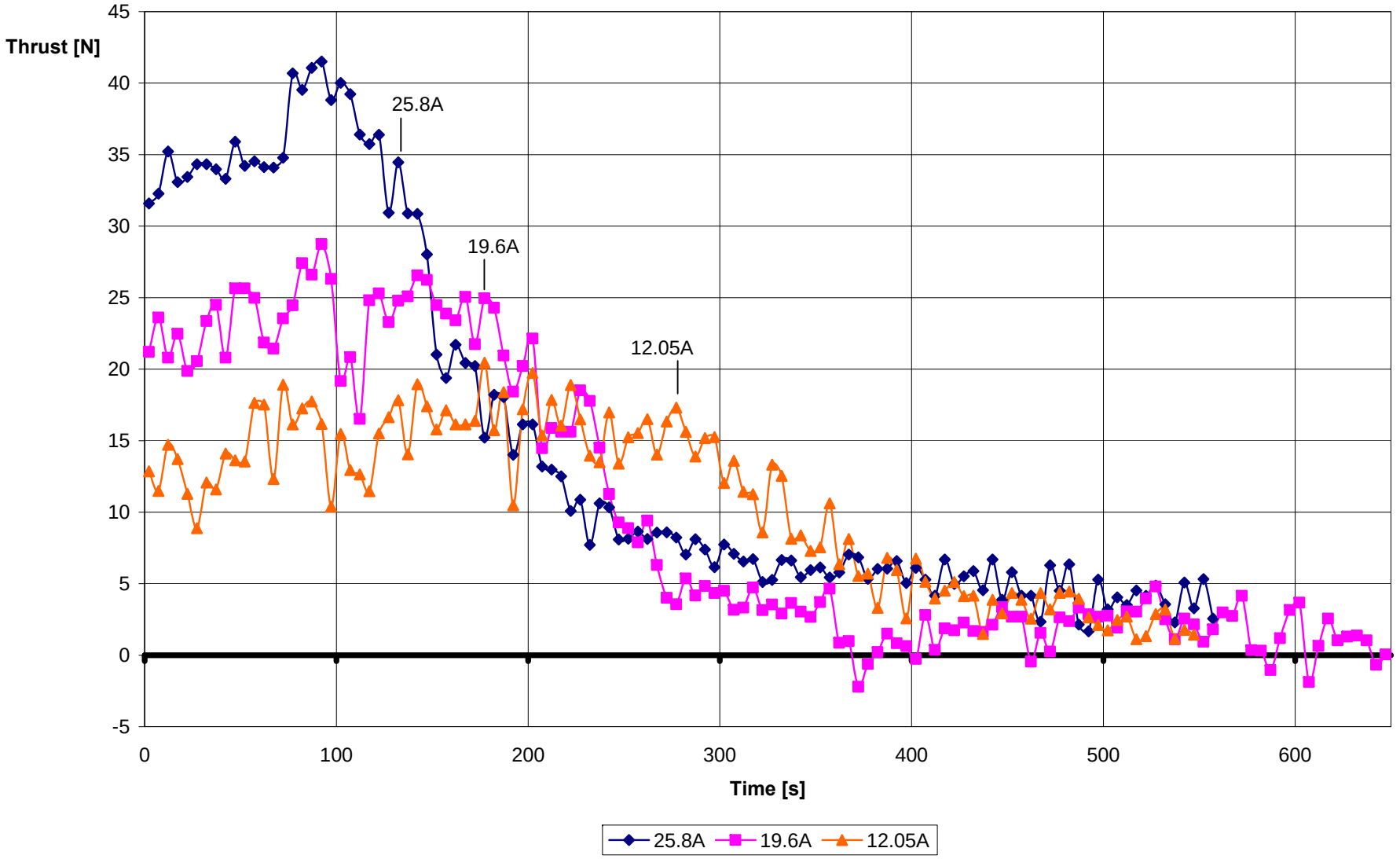

Figure 6.3a Thrust over Time at Different Current – Hacker A60-18M with APC 20x10 at 10.28 ms^{-1} (Wind Tunnel Test)

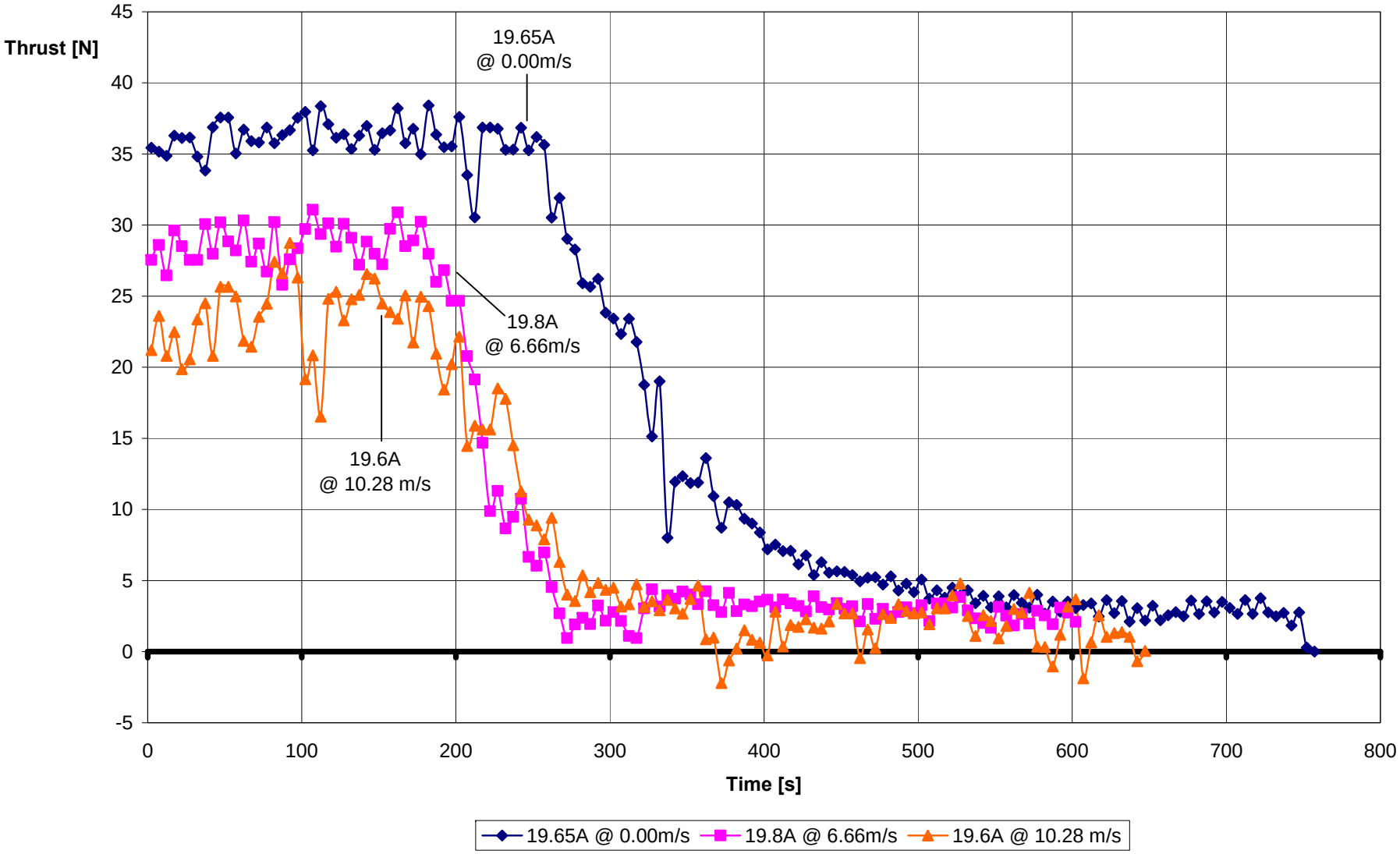

Figure 6.3b Thrust over Time at different Air Speed – Hacker A60-18M with APC 20x10 at ca. 19.6 A (Static and Wind Tunnel Test)

5.2 Comparison to Static Test Results

Comparison of Thrust Produced

As propeller theory suggests and as can be seen in figure 6.3b, thrust at a certain power input decreases with increasing air speed. At the same time, the aerodynamic drag increases. With increasing flight speed, thrust and drag converge until one equals the other. At lower air speed, the thrust exceeding the value of drag will result in forward force. This can be seen in figure 6.1b. Even with the lowest tested power input of 12.05 A and an air speed of already 10.28 m/s, the forward force would result in a further speed increase. One should always bear in mind that these experiments are tested on the power unit only. The propeller is therefore only loaded with the weight of the motor and of the attachment. Mounted on an airframe, the forward force would be reduced not only by the aerodynamic drag, but also by the weight of the airframe.

A comparison of thrust regarding the input power reveals a steady thrust loss for lower input powers. At a discharge current of 25.8 A and an airspeed of 10.28ms-1 the average thrust is much closer to its static value than it is for lower input powers. The curves for thrust over input power at different airspeeds are shown in Figure 6.4. Please note that the two outer thrust values for an air speed of 6.66 ms-1 are approximated. They were found by interpolating between 0.00 ms-1 and 10.28 ms-1 with the help of the measured thrust value for 19.8 A.

Comparison of Usable Running Time

A look at table 6.1 and the thrust curves in figure 6.3b reveals that the usable running time has heavily decreased from its static value. A comparison with running times of other motor-propeller combinations (discussed in chapter 5.4) turns out less severe. The running time for the bulk of discharge currents is very close to the curve of the graphical approach determined in chapter 5.4, as can be seen in figure 6.5. The results replicate static test results, which showed uncommonly long usable running times for the static test of the Hacker A60-18M equipped with an APC 20x10 propeller. Some possible explanation for this was given in chapter 5.4, but as the true reason remains unclear, more investigation is needed.

In comparison, the usable running time for 12.05 A at an air speed of 10.28 ms^{-1} is indeed far off other usable running times. It is reduced by almost fifty seconds from the worst static result. Despite several possible explanations, it is most likely that the usable running time is strongly reduced because of the used battery pack. Despite their identical design and charging procedures, the final capacities of the three battery packs were indicated different by the charging computer. The third battery pack was always showing the by far lowest indicated

capacity of the three used packs. Its indicated capacity averaged out at 1850 mAh, which is 350 mAh less than its nominal capacity. In all other experiments, which were run at comparable discharge currents of about 12 A, the two other battery packs were used. Their use resulted in longer usable running time. Chapter 5.4 and 5.5 already discussed the strong relation of usable running time and capacity. To avoid falsified results in future testing, it is advisable not to use battery packs, which show that diverse capacities.

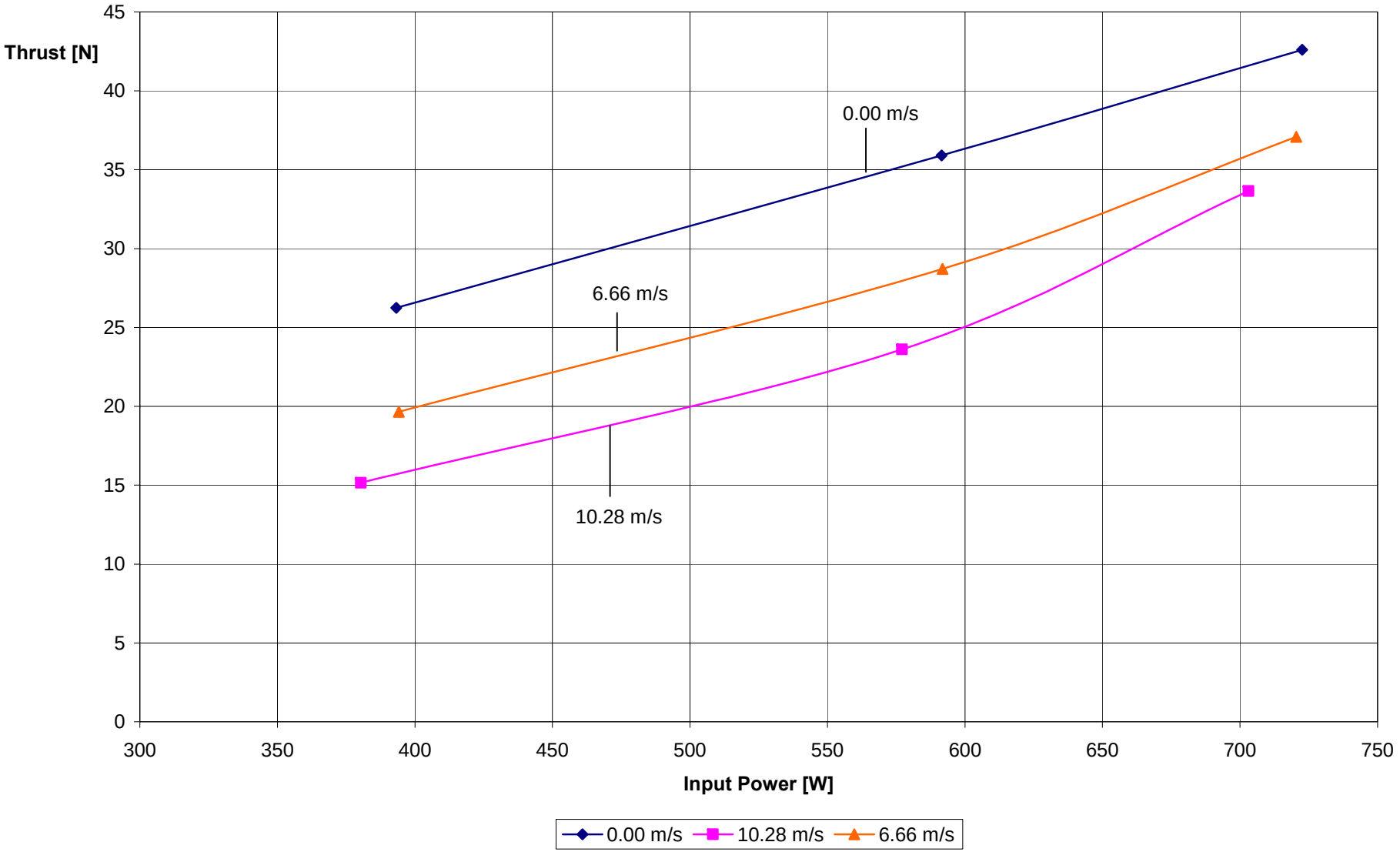

Figure 6.4 Thrust over Input Power at different Air Speed – Hacker A60-18M with APC20x10 (Static and Wind Tunnel Test)

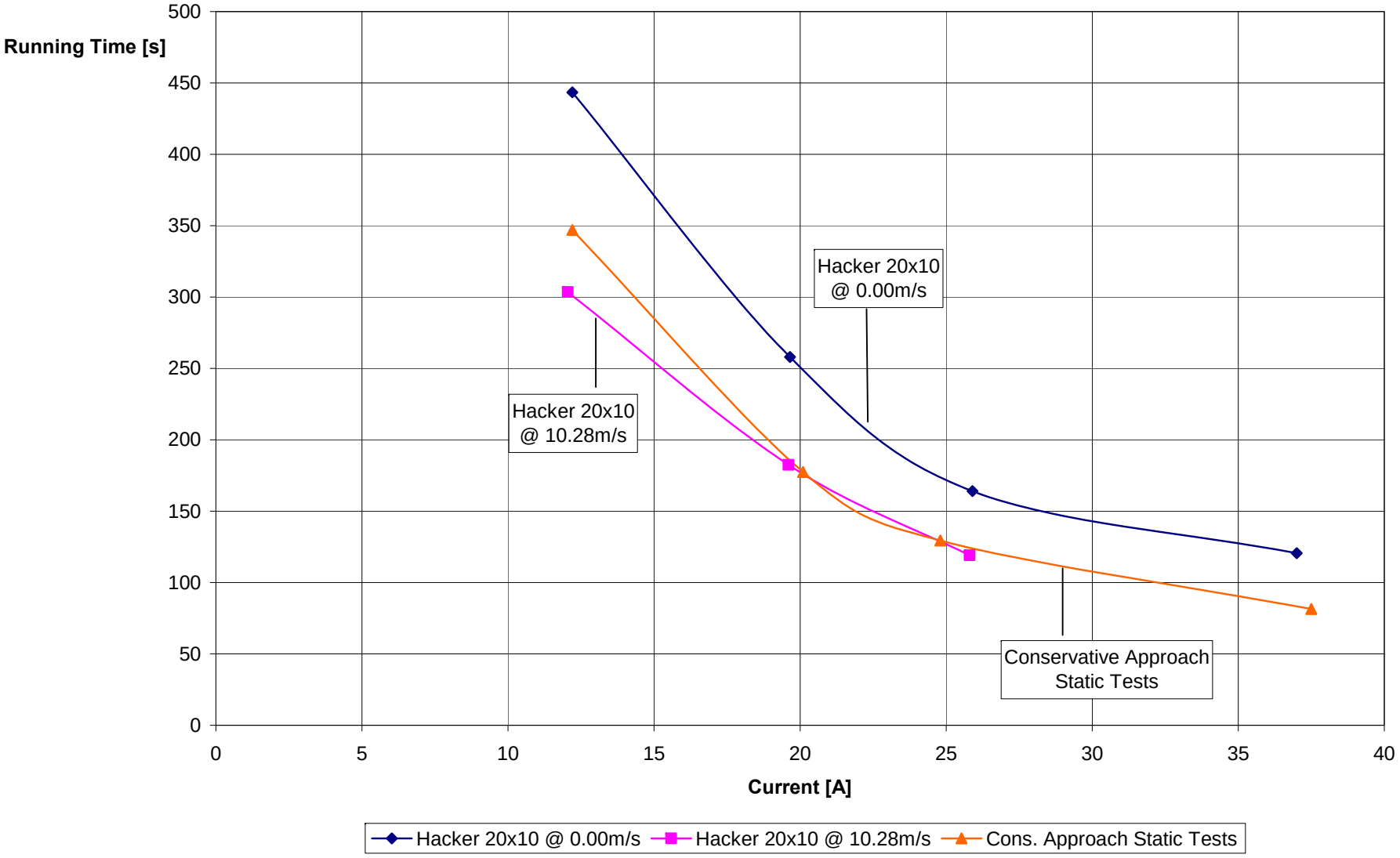

Figure 6.5 Usable Running Time over Current at different Air Speed – Hacker A60-18M with APC 20x10 (Static and Wind Tunnel Test)

5.3 Comparison to Thrust Estimates with Computer Software

Software Suitability

In comparison to static tests, the input of wind tunnel test results into the *Propeller Selector* will result in a higher number of estimated values. In addition to estimates of the thrust produced and the power absorbed, the software will output estimates for the power output and the efficiency of the propeller. This is due to the general definitions of power output, which is flight speed multiplied by thrust. For zero air speed, the two values will therefore always be computed to zero. For the same reason, these values are dependent on thrust and should neither be seen, nor be handled as independent estimates.

As already explained in chapter 5.3, the assumption can be made that the *Propeller Selector* software has to extrapolate experimental data to get results for the propellers used, as the NACA tested at slightly different propeller blade angles.

Contrasting Test Data and Software Estimates

As illustrated in chapter 4.4, a uniform air speed over the propeller diameter could not be made possible for the experiments. Instead, the air speed followed a bell-shaped curve, ranging from very high speeds at the propeller hub to very low speeds at the propeller tip. To be able to make a statement about the overall air speed and to make the results comparable to software estimates, the arithmetic mean was taken as the overall airspeed. This mean airspeed was then taken as input for the air speed of the *Propeller Selector*. The second input required by the software to produce thrust estimates is the rotational rate of the propeller, which was also gained by measurement during the test procedure.

Table 6.2 contrasts the thrust gained from the load cell measurement and the thrust estimated by the *Propeller Selector*. In addition, the total efficiencies η_{Total} were calculated. The total efficiency of the motor-propeller combination is the ratio of propeller output to power input. As mentioned above, the propeller output is the product of flight speed and thrust produced. The power input is calculated by multiplying discharge current with discharge voltage. Note that the estimated value of η_{Total} is not a software output. It was calculated by inserting the estimated thrust into equation (6.1). The air speed and input power for both, measured and estimated efficiency were taken from test data.

$$\eta_{Total} = \frac{P_{out}}{P_{in}} = \frac{T_{average} \cdot v_{air}}{I_{in} \cdot U_{in}} \tag{6.1}$$

where

η_{Total} = total efficiency for the motor-propeller combination

P_{out} = propeller output [W]

P_{in} = motor input [W]

Table 6.2 Measured Thrust and Estimated Thrust at different Current and Air Speed – Hacker A60-18M with Propeller APC 20x10 (Static and Wind Tunnel Test)

v_{air} [m/s]	I_{in} [A]	P_{in} [W]	n [RPM]	$T_{average}$ [N] measured	$T_{average}$ [N] estimated	Deviation [%]	η_{Total} [%] measured	η_{Total} [%] estimated
0.00	37.00	912.05	5050	52.657	47.842	-9.14%	-	-
0.00	25.90	722.61	4640	42.613	40.389	-5.22%	-	-
0.00	19.65	591.47	4278	35.903	34.333	-4.37%	-	-
0.00	12.20	393.21	3700	26.243	25.682	-2.14%	-	-
6.66	19.8	591.82	4523	28.714	34.635	20.62%	32.31%	38.98%
10.28	25.8	703.11	4837	33.65	35.606	5.81%	49.20%	52.06%
10.28	19.6	577.10	4538	23.609	30.453	28.99%	42.06%	54.25%
10.28	12.05	380.37	3953	15.154	21.357	40.93%	40.96%	57.72%

Accuracy of Thrust and Efficiency Estimates

As can be seen in figure 6.6, the thrust estimates for the wind tunnel tests are far less accurate than the estimates for the static tests. Whereas the deviation averages out at -5.22 per cent for the static test, the estimates for the wind tunnel have a deviation of 36.24 per cent in average.

Figure 6.7 shows the values of total efficiency gained from test results and software estimates. The shape of both curves is typical for efficiency curves. The curves for air speeds above 10.28 m/s are extrapolated using a polynomial trend equation. The curves suggest a peak in total efficiency at about 15 ms^{-1} for the wind tunnel measurement, and a peak at about 15.5 ms^{-1} for the estimations of the *Propeller Selector*. It is likely that under better test conditions (see below) the curves for measured efficiency and estimated efficiency would be much closer. Nevertheless, both results suggest a rather flat efficiency profile. The motor-propeller combination seems to be capable of working under a broad bandwidth of flight speeds and rotational rates. For an aircraft, which is intended to fly mission segments at different air speeds, the combination seems to be reasonably compatible.

A first look at the large deviation between measurement and estimation would suggest not using the *Propeller Selector* software for in-flight estimates. However, we should bring to mind at this stage the many cutbacks of our wind tunnel measurements. As the ratio of propeller disc area to diffuser outlet area is large, we have a very uneven flow over the propeller diameter. To produce accurate results that are comparable to in-flight characteristics,

the propeller disc area should be always small in comparison to the air stream. Furthermore, as already mentioned in chapter 4.4, the propeller is absorbing even slower air from outside the wind tunnel. This will further increase the difference of air speed advancing the different parts of the propeller blades.
Especially the result of drag and thrust are affected. The outer part of the propeller, which is producing the better part of the thrust, would benefit from running inside a faster air stream. Instead, the fast air is advancing the region of the motor and the propeller hub, thus increasing the form drag. Based on the results contained in this report, it is therefore unfortunately not possible to say whether the software is accurate in estimating in-flight propeller performance or not. Further research is needed in this field. To generate adequate results, future experiments should find possible ways to run the propeller in a uniform airflow.

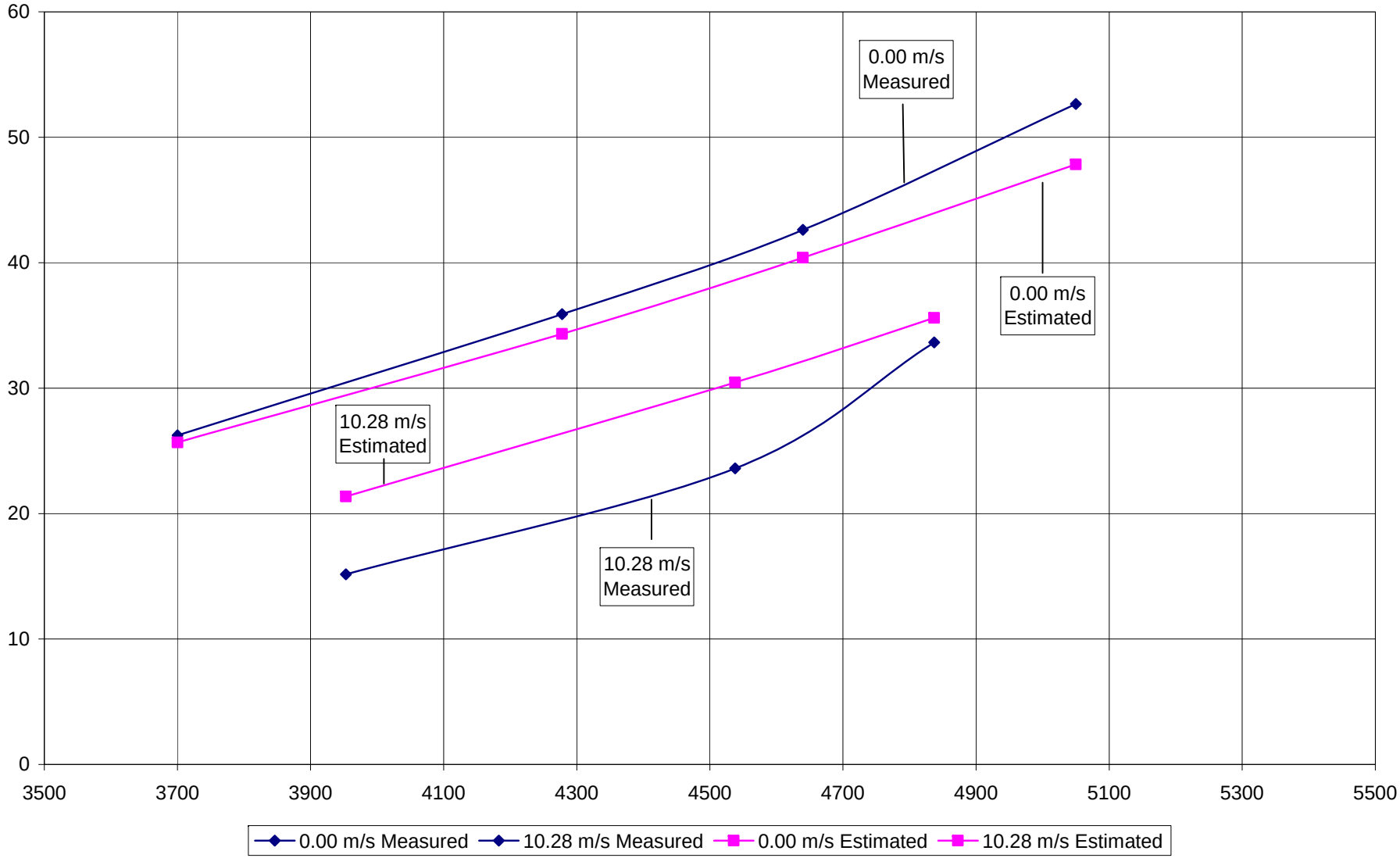

Figure 6.6 Thrust over Rotations per unit time – Propeller Selector Estimates vs. Direct Measurements (Wind Tunnel Test)

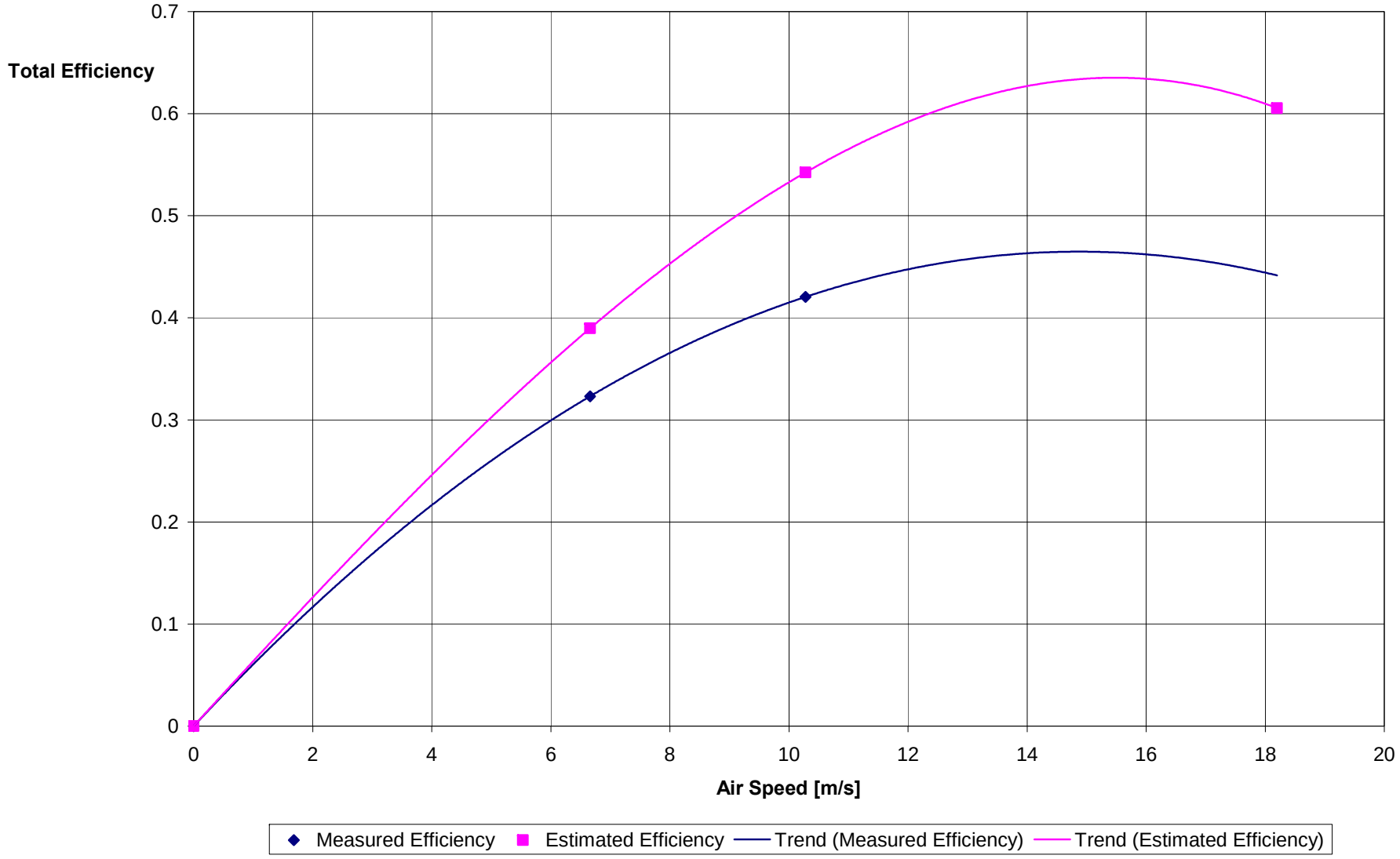

Figure 6.7 Total Efficiency over Air Speed – Measurement vs. Software Estimation – Hacker A60-18M with APC 20x10 (Wind Tunnel Test)

6 Conclusions

To **complete the development of the test rig and to build up an accurate measuring environment for future experiments** the test rig design was slightly changed to accommodate a new load cell. The load cell measured the force of the propeller pulling forward and transferred it to a computer. Thus, continuous thrust recordings with the help of software were made possible. Predominantly, this was done to generate thrust over time curves.

Furthermore, the number of physical variables to be measured was increased. Measurements of the propeller revolutions per unit time, the speed of air exiting the propeller and the motor current and voltage were included into the test procedures.

The test procedure was standardized to ensure their comparability. Hence, the motors were powered with one of three battery packs of identical design. Furthermore, the discharge current of the batteries acted as a reference value to standardize the input power. Four discharge currents (12.2 A, 20.0 A, 25.9 A and 37.0 A) were chosen in the range of motor currents specified by manufacturer specifications. In all tests, thrust measurements were taken and recorded constantly until the batteries were fully depleted. The time, for which a constant thrust could be provided, was determined. This time was then named the ‘usable running time’.

To **ascertain the performance of motors and propellers used**, the two motors, namely the Hacker A60-18M and the Plettenberg HP370/50/A3, were consecutively equipped with two different propellers and tested in a static test.

The Hacker A60-18M dominates the static test results with the smaller APC 20x10 propeller. Comparing the thrust over input power, an almost linear thrust curve could be determined. The curve indicates a constant motor efficiency for the currents tested. According to test results, the Hacker A60-18M motor was overstrained with the large APC 22x12W propeller. This was indicated by an unstable thrust curve and large thrust fluctuations.

The Plettenberg HP370/50/A3 dominates the static test results with the larger APC 22x12W propeller. The efficiency at low input powers for both propeller sizes is higher than the efficiency at high power inputs.It should also be noted that the large propeller was beating the air heavily at high power inputs, what resulted in large thrust fluctuations. This was especially true for the Hacker A60-18M.

To **contrast the measured performance to the equipment’s theoretical performance**, NiMH battery theory, as well as propeller theory was taken into account.

According to the theory of battery discharge, the capacity of a battery is dependent on the current drawn. The theory was fortified by our test results gained from usable running time measurements at different power settings. The usable running time at identical discharge currents was similar regardless nearly all motor-propeller combinations tested. Our results suggest usable running times that rise dramatically with lower currents. A graphical approach to predict usable running time was established on the test results (Ch. 5.4, figure 5.7b). It should be noted that the static test on the Hacker A60-18M motor equipped with the APC 20x10 propeller resulted in significantly higher running times than all other tests. The reason for this remained unclear.

A similar behaviour as for the running time was found for the discharge voltage. A linear drop in discharge voltage for increasing discharge currents resulted from the measurements (Ch. 5.2, figure 5.3). This behaviour is according to battery theory. Theory and measurements of discharge voltage and running time suggest powering the motors with reasonably low discharge currents. We measured strong reductions in running time and comparatively small thrust increase for high current draws.

The effect of battery storage on usable running time was experimentally determined and compared to the theory of battery self-discharge. The results corroborated the theory. According to theory, the capacity of the batteries was clearly reduced after two weeks of storing at 20 °C, as so was the usable running time. It was further found out, that the loss in running time increases with lower discharge currents. After storage, at a discharge current of 25.9 A, the usable running time reached ninety-six per cent of its original value. At a discharge current of 12.2 A, it only reached seventy per cent.

According to propeller theory, it was found out that a large propeller produces the same thrust at lower rotational rates as a small propeller at high rotational rate. Propeller theory also suggests that a large propeller is then more efficient as a small one. This could only be partly corroborated by the test results. A comparison of thrust produced at same power settings showed that the large propeller produced more thrust, thus was more efficient, at low input powers. At high input powers, the small propeller turning at high rotational rate clearly dominated.

To **evaluate the difference between static and wind tunnel tests**, additional wind tunnel tests with the Hacker A60-18M and the APC 20x10 propeller were run.

Airflow speed measurements along the propeller diameter revealed that the propeller to diffuser outlet ratio was too large to achieve a uniform air speed over the propeller diameter, so the arithmetic mean had to be taken as the overall air speed. According to propeller theory, the results show a decrease in thrust and an increase in drag with rising air speed. The thrust produced at changing input power and constant air speed was compared to the results of the static test. The comparison revealed similarities in the slope of the thrust curves.

It was further found out that the total efficiency at a constant discharge current of 20 A is following a reasonably flat curve with a peak at an air speed of 15 ms^{-1}.

To **evaluate the thrust estimates of computer software**, results of a computer program called *Propeller Selector* were contrasted to the test results. The software's calculations are based on experimental data of propeller wind tunnel tests performed by the National Advisory Committee for Aeronautics (NACA). Inputs needed to estimate thrust were the diameter and pitch of the propeller, the rotational rate and the air speed. The rotational rate was taken from actual measurements.

Comparing the estimates to the results of the static test, a reasonably good accuracy was determined. Especially for the smaller propeller, test results and software estimates are close. The estimated values deviate down 1.87 per cent in average for the smaller propeller and 6.33 per cent down for the larger propeller. The results suggest that the larger propeller was underestimated by the software. It should be noted that the software does not provide an input for uncommon propeller design. The 'wide-blade' 22x12W propeller was therefore calculated as a regular 22x12 propeller. Moreover, the software estimated the large propeller to be close to stall at zero air speed.

The thrust estimates for the wind tunnel tests were found to be far less accurate than the estimates for the static tests. Whereas the deviation averages out at -5.22 per cent for the static test, the estimates for the wind tunnel have a deviation of 36.24 per cent in average. Nonetheless, a statement about the adequacy of the software for estimating in-flight results could not be given. As the propeller was too large to run in a uniform wind tunnel air stream, the accuracy of the wind tunnel test results must be doubted.

7 Recommendations

Based on the results achieved and the difficulties encountered, the following future work is recommended:

Improve the test conditions and rerun the wind tunnel tests. To enhance comparability to actual in-flight performance, a uniform airflow over the propeller diameter should be achieved. To test propellers of the sizes dealt within this report, the wind tunnel air stream has to be dramatically enlarged.

Compare more accurate wind tunnel results to the estimates of the Propeller Selector software. A statement about the software's adequacy to predict in-flight performance still needs to be given.

Rerun static tests for the Hacker A60-18M motor equipped with the APC 20x10 propeller. Investigate the uncommonly high results concerning usable running time of the first test. In average, the combination achieved 23 per cent longer running times. The reason for this could not be found.

Rerun static tests for the Hacker A60-18M motor equipped with the APC 22x12W propeller. Investigate the unstable thrust curve of the first test. The first test did not provide enough information to find out if the propeller was running off-design or if the motor was overstrained by the propeller.

To make results of future experiments more comparable, the motor/discharge current should be set more exactly. This could possibly be done by a current control unit. Another possibility is to access the speed control directly. Experiments done without using the radio control would also minimize disturbances.

To make results of future experiments more comparable, the batteries used should all feature the same capacities indicated by the charging computer. We encountered difficulties in comparing all test results adequately, as one battery pack used had a strongly reduced capacity.

References

Ahern 2007 AHERN, Judson L.: *International Gravity Formula*, 2007. – URL: http://geophysics.ou.edu/solid_earth/notes/potential/igf.htm (2008-04-30)

GP 2006 GOLD PEAK: *Nickel Metal Hydride Technical Handbook*. Hong Kong: Gold Peak International Limited (GP), 2006. – GP Release GPPA6THH-A

Lindon 1995 LINDON, David: *Handbook of Batteries*. New York: McGraw-Hill, 1995

Raymer 1999 RAYMER, Daniel: *Aircraft Design: A Conceptual Approach*. Reston: American Institute for Aeronautics and Astronautics (AIAA), 1999

Simons 1994 SIMONS, Martin: *Model Aircraft Aerodynamics,* Hemel Hempstead: Argus, 1994

Sokia 1990 SOKIA, Thomas J.; JAFFE, Wolfgang: *Brushless DC Motors : Electronics Commutation and Controls*. Blue Ridge Summit: Tab Books, 1990

Stinton 2001 STINTON, Darrol: *The Design of the Aeroplane*. Oxford: Blackwell Science, 2001

Appendix A
Test Rig Modification and Calibration

A.1 Test Rig Modification

Previous tests for the Design/Build/Fly (DBF) Competition were made in autumn 2007. A test rig was designed by students to measure the static thrust produced by the different motor-propeller combinations. In this design, a shaft that accommodates the motor is located in the propeller's axis of rotation. As can be seen in figure 6.1 (former rig assembly), the thrust was then measured by attaching an external load cell to a pin.

For the experiments of this report, it was decided to modify the rig assembly slightly. In the design described above, the axis of measurement was not coincident with the axis of the thrust produced. Due to the lever arm of the pin the load cell would measure a force other than actually pulling on the shaft. A further reason not to use the former load cell was its programming to measure peak values only. Propeller thrust is tending to be unsteady and to oscillate around a mean value. A single peak value could therefore not be of interest for our experiments as our intention was to measure this mean and not an ultimate upper limit. A continuous thrust measurement was achieved by using another, smaller load cell. Figure 6.1 and 6.2 show the load cell and its placement in the test rig. Due to its smallness, it was easy to use it with the already existing test rig by making only a few changes to design. By arranging the load cell behind the shaft, measurement and thrust were located in one axis. Compared to the load cell used before, this load cell does not include its own reading. In our experiments, measurements were indicated by an external transducer and transferred to a computer using a digital oscilloscope. While testing, a computer program recorded thrust forces every 0.5 seconds.

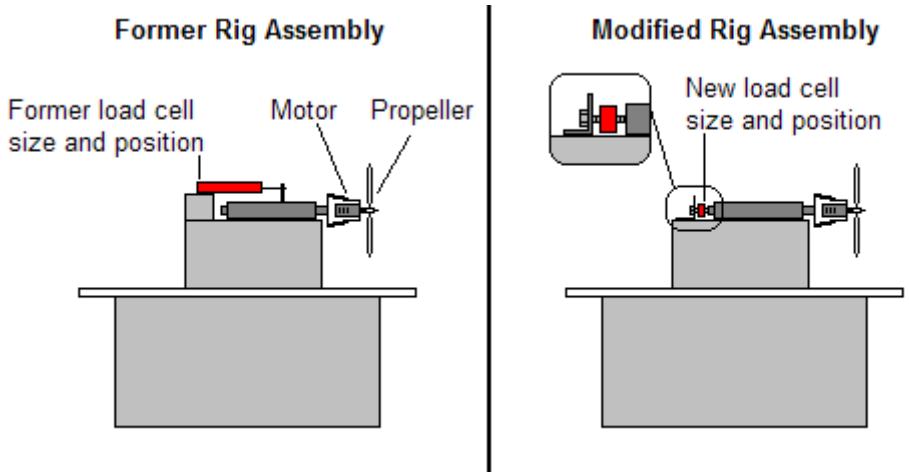

Figure A.1 Rig Assembly Comparison

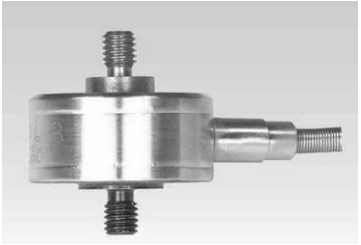

Figure A.2 Load cell type SLC31 – actual size (RDP Group 2008)

A.2 Load Cell Calibration

The thrust measurement of the modified rig assembly was calibrated using a wire, pulley wheel and dead weights as schematically shown in figure 6.3. The weight was increased and decreased gradually to be able to give information about a hysteresis within the system.
The measurements taken while increasing weight where slightly smaller than the actual mass of the dead weights, e.g. the load cell measured a mass of 10.795 kg when the actual mass was 11 kg. While decreasing, the measurements where slightly higher, e.g. the dead weights of 11 kg were indicated as 11.068 kg. Hence, a small hysteresis was found.
Based on the results of 30 measurements a mean value-indicated for a mass of 1.0 kg was calculated and found to be 1.0067 kg. In addition, the standard deviation σ from the mean value was calculated to be 0.022 kg. Hence, within the upper and lower limits of $\pm\,\sigma$, 1.0 kg is measured reasonably accurate between 1.0287 kg and 0.9847 kg. Tables and graphs containing all thirty measurements and the calculation of the standard deviation can be found on the following pages of this appendix.

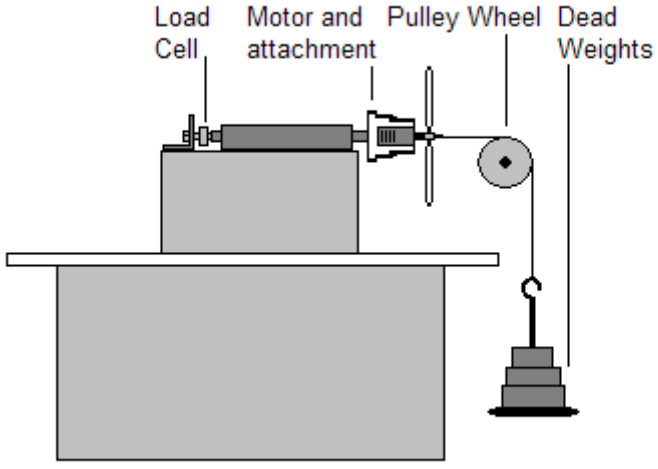

Figure A.3 Test Rig Calibration using Dead Weights

A.3 Calibration Data

Measurement No. 1

Type: Test Rig with pulley wheel and dead weights – horizontal
Date: 27/02/2008
Conversion Factors (to SI units): 1 lb = 0.453 592 37 kg (exactly)

Table A.1 Test Results regarding Total Weight – Measurement No.1

Dead Weights Total [kg]	Indication Total [lbs]	Indication Total [kg]	Absolute Deviation [kg]	Relative Deviation [%]
0	3.5	0.000	0.000	-
5	14.3	4.899	-0.101	-2.024
10	25.5	9.979	-0.021	-0.210
11	27.9	11.068	0.068	0.615
12	30.2	12.111	0.111	0.924
11	27.3	10.795	-0.205	-1.859
10	25.8	10.115	0.115	1.151
5	14.5	4.990	-0.010	-0.210
0	3.7	0.091	0.091	-

Table A.2 Test Results regarding Weight Increments – Measurement No.1

Dead Weights Increments [kg]	Indication Increments [lbs]	Indication Increments [kg]	Absolute Deviation [kg]	Relative Deviation [%]
-	-	-	-	-
5	10.8	4.899	-0.101	-2.024
5	11.2	5.080	0.080	1.605
1	2.4	1.089	0.089	8.862
1	2.3	1.043	0.043	4.326
-1	-2.9	-1.315	-0.315	31.542
-1	-1.5	-0.680	0.320	-31.961
-5	-11.3	-5.126	-0.126	2.512
-5	-10.8	-4.899	0.101	-2.024

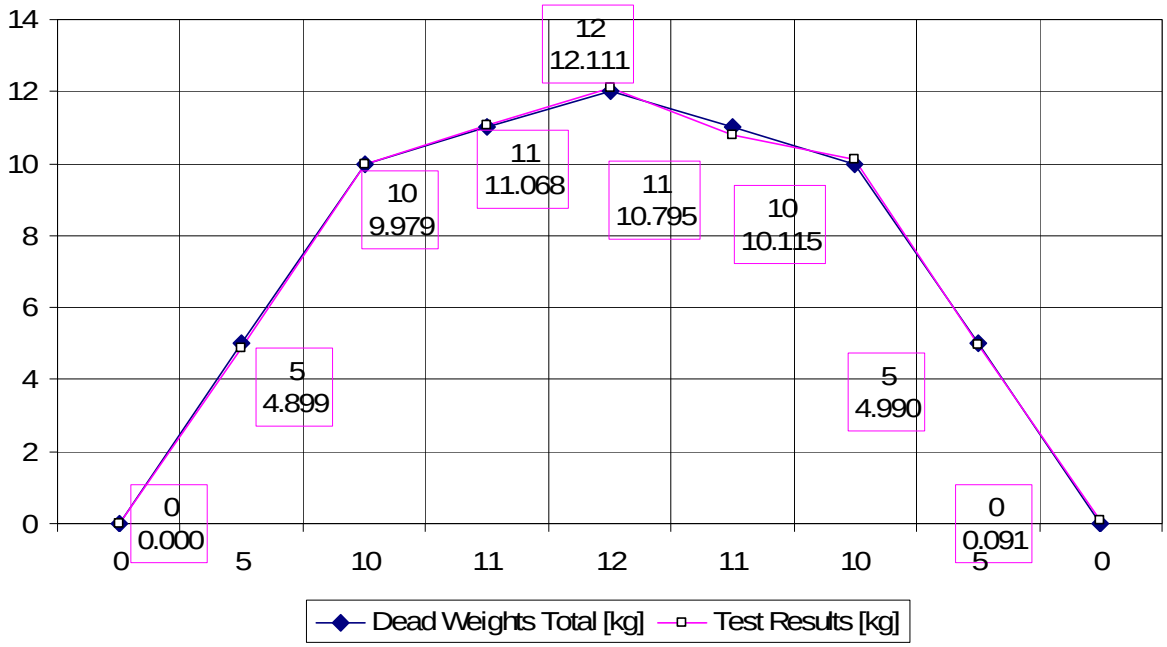

Figure A.4a Test Results vs. Dead Weights – Measurement No.1

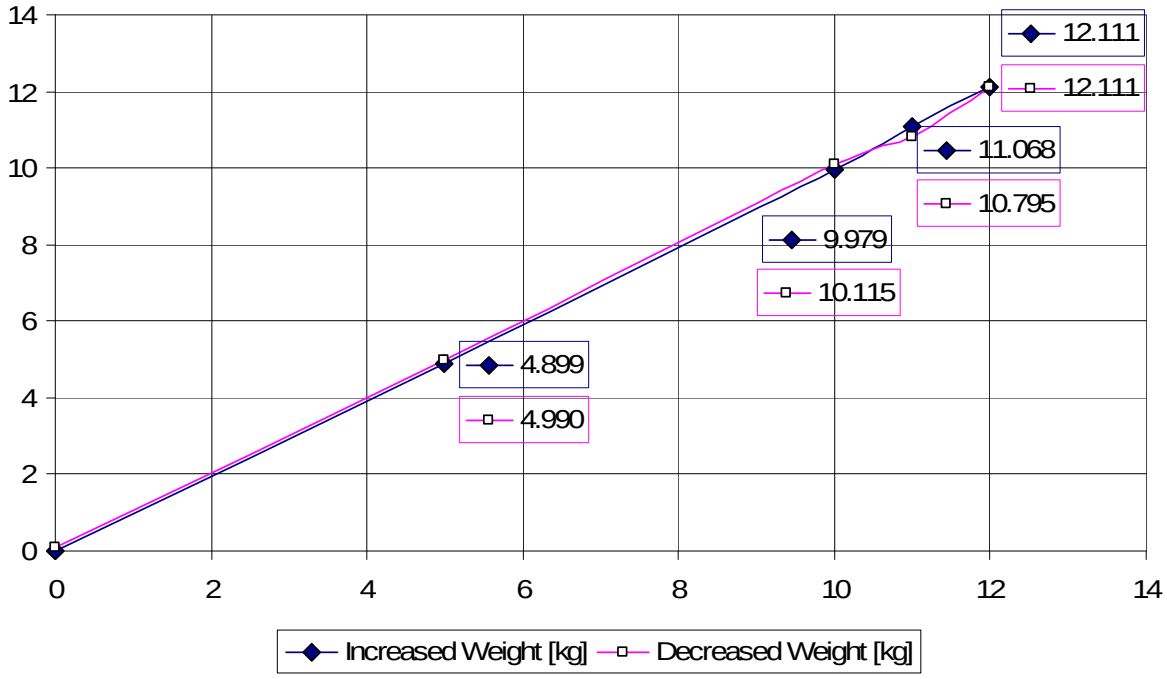

Figure A.4b Increased Weight vs. Decreased Weight – Measurement No.1

Measurement No. 2

Type: Test Rig with pulley wheel and dead weights – horizontal
Date: 27/02/2008
Conversion Factors (to SI units): 1 lb = 0.453 592 37 kg (exactly)

Table A.3 Test Results regarding Total Weight – Measurement No.2

Dead Weights Total [kg]	Indication Total [lbs]	Indication Total [kg]	Absolute Deviation [kg]	Relative Deviation [%]
0	0	0.000	0.000	-
5	10.8	4.899	-0.101	-2.024
10	21.8	9.888	-0.112	-1.117
11	24	10.886	-0.114	-1.034
12	26.2	11.884	-0.116	-0.966
11	25.3	11.476	0.476	4.326
10	23	10.433	0.433	4.326
5	11.5	5.216	0.216	4.326
0	0.3	0.136	0.136	-

Table A.4 Test Results regarding Weight Increments – Measurement No.2

Dead Weights Increments [kg]	Indication Increments [lbs]	Indication Increments [kg]	Absolute Deviation [kg]	Relative Deviation [%]
-	-	-	-	-
5	10.8	4.899	-0.101	-2.024
5	11	4.990	-0.010	-0.210
1	2.2	0.998	-0.002	-0.210
1	2.2	0.998	-0.002	-0.210
-1	-0.9	-0.408	0.592	-59.177
-1	-2.3	-1.043	-0.043	4.326
-5	-11.5	-5.216	-0.216	4.326
-5	-11.2	-5.080	-0.080	1.605

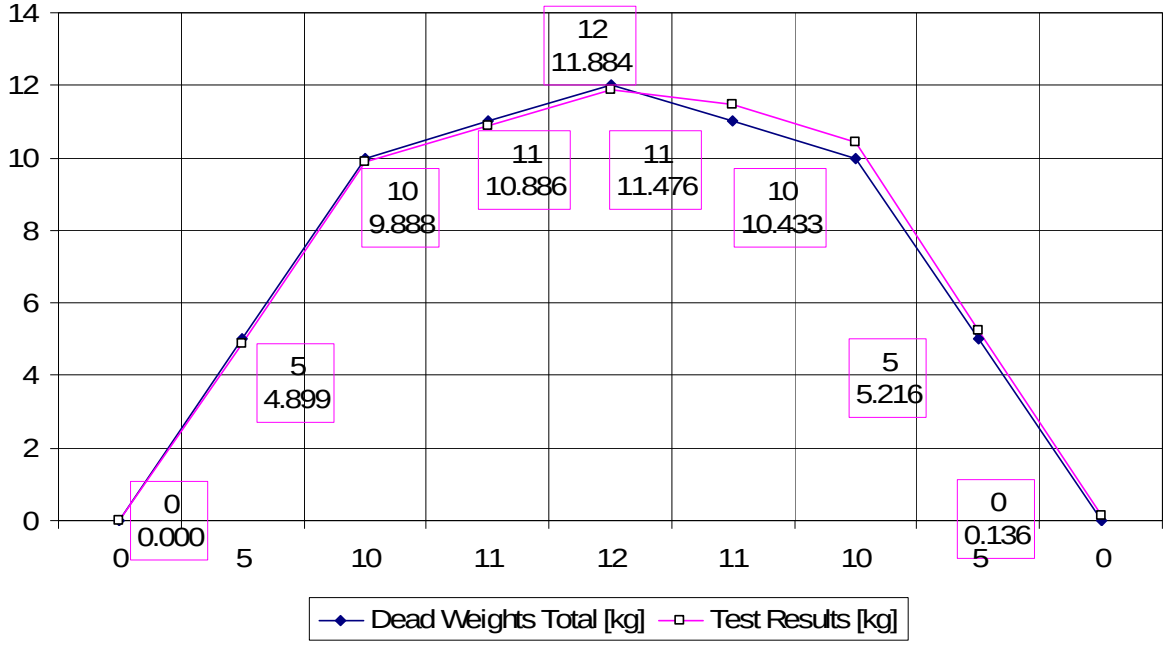

Figure A.5a Test Results vs. Dead Weights – Measurement No.2

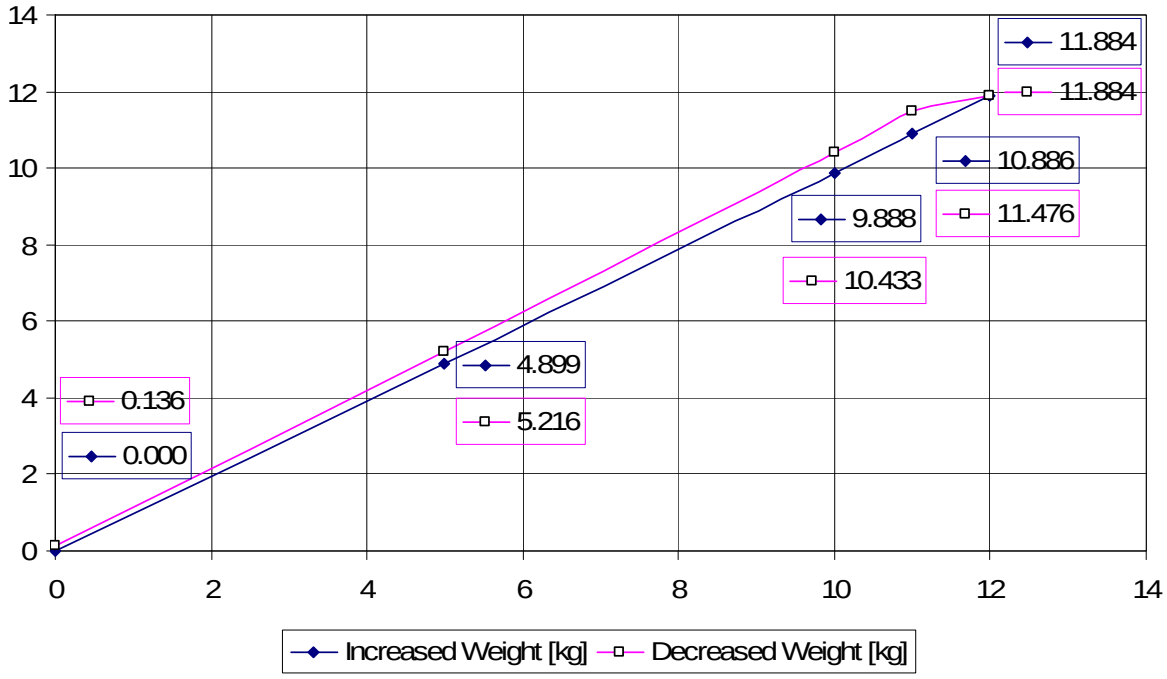

Figure A.5b Increased Weight vs. Decreased Weight – Measurement No.2

Measurement No. 3

Type: Test Rig with pulley wheel and dead weights – horizontal
Date: 27/02/2008
Conversion Factors (to SI units): 1 lb = 0.453 592 37 kg (exactly)

Table A.5 Test Results regarding Total Weight – Measurement No.3

Dead Weights Total [kg]	Indication Total [lbs]	Indication Total [kg]	Absolute Deviation [kg]	Relative Deviation [%]
0	0	0.000	0.000	-
5	11	4.990	-0.010	-0.210
10	21.3	9.662	-0.338	-3.385
11	24.3	11.022	0.022	0.203
12	26	11.793	-0.207	-1.722
12.25	26.6	12.066	-0.184	-1.506
12	26.4	11.975	-0.025	-0.210
11	24.5	11.113	0.113	1.027
10	22	9.979	-0.021	-0.210
5	11.1	5.035	0.035	0.698
0	0.1	0.045	0.045	-

Table A.6 Test Results regarding Weight Increments – Measurement No.3

Dead Weights Increments [kg]	Indication Increments [lbs]	Indication Increments [kg]	Absolute Deviation [kg]	Relative Deviation [%]
-	-	-	-	-
5	11	4.990	-0.010	-0.210
5	10.3	4.672	-0.328	-6.560
1	3	1.361	0.361	36.078
1	1.7	0.771	-0.229	-22.889
0.25	0.6	0.272	0.022	8.862
-0.25	-0.2	-0.091	0.159	-63.713
-1	-1.9	-0.862	0.138	-13.817
-1	-2.5	-1.134	-0.134	13.398
-5	-10.9	-4.944	0.056	-1.117
-5	-11	-4.990	0.010	-0.210

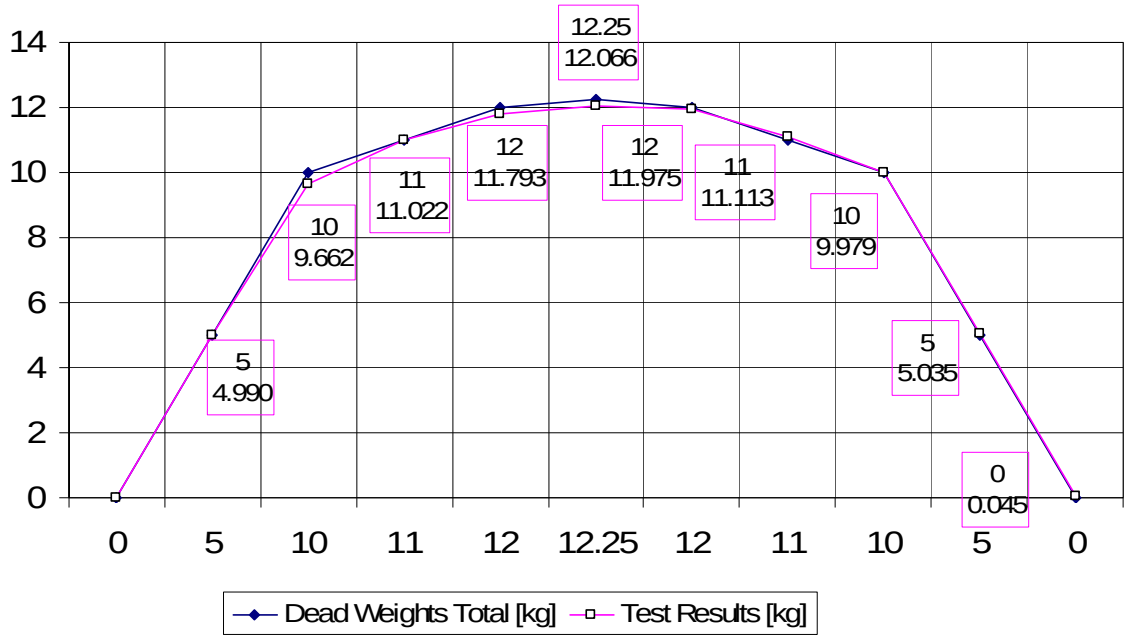

Figure A.6a Test Results vs. Dead Weights – Measurement No.3

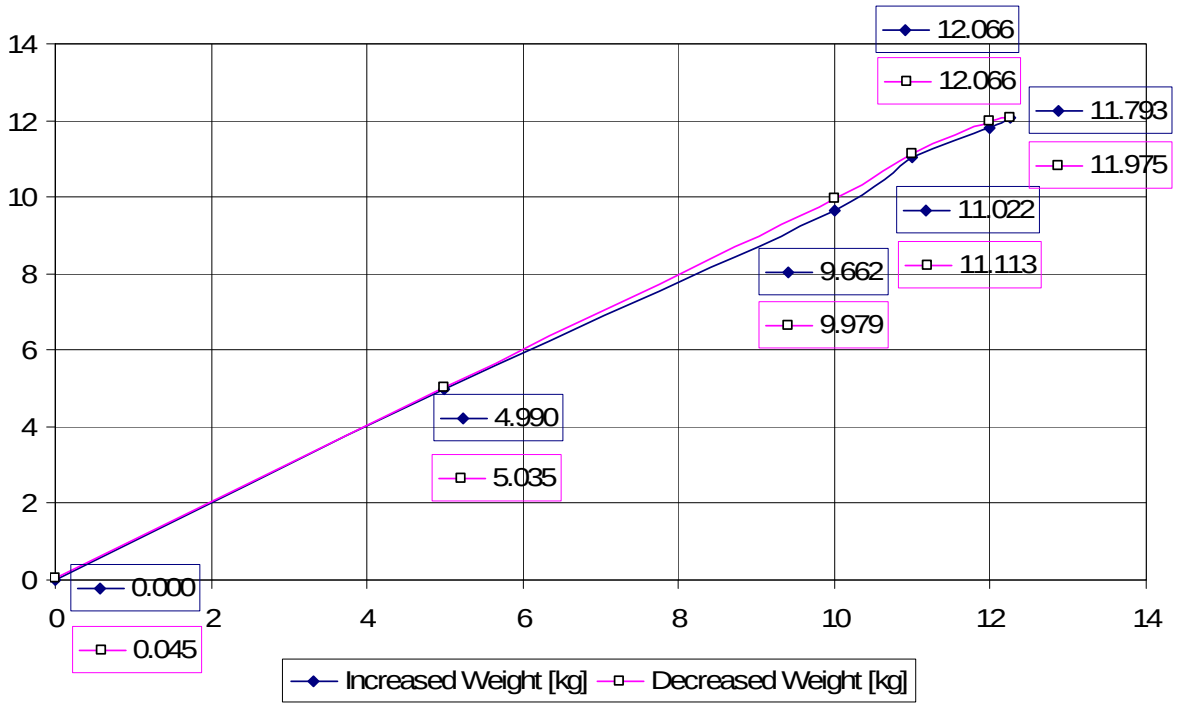

Figure A.6b Increased Weight vs. Decreased Weight – Measurement No.3

Measurement No. 4

Type: Test Rig with pulley wheel and dead weights – horizontal
Date: 27/02/2008
Conversion Factors (to SI units): 1 lb = 0.453 592 37 kg (exactly)

Table A.7 Test Results regarding Total Weight – Measurement No.4

Dead Weights Total [kg]	Indication Total [lbs]	Indication Total [kg]	Absolute Deviation [kg]	Relative Deviation [%]
0	0.1	0.000	0.000	-
1	2.4	1.043	0.043	4.326
2	4.5	1.996	-0.004	-0.210
7	15.3	6.895	-0.105	-1.506
12	26.5	11.975	-0.025	-0.210
7	15.3	6.895	-0.105	-1.506
2	4.5	1.996	-0.004	-0.210
1	2.4	1.043	0.043	4.326
0	0.1	0.000	0.000	-

Table A.8 Test Results regarding Weight Increments – Measurement No.4

Dead Weights Increments [kg]	Indication Increments [lbs]	Indication Increments [kg]	Absolute Deviation [kg]	Relative Deviation [%]
-	-	-	-	-
1	2.3	1.043	0.043	4.326
1	2.1	0.953	-0.047	-4.746
5	10.8	4.899	-0.101	-2.024
5	11.2	5.080	0.080	1.605
-5	-11.2	-5.080	-0.080	1.605
-5	-10.8	-4.899	0.101	-2.024
-1	-2.1	-0.953	0.047	-4.746
-1	-2.3	-1.043	-0.043	4.326

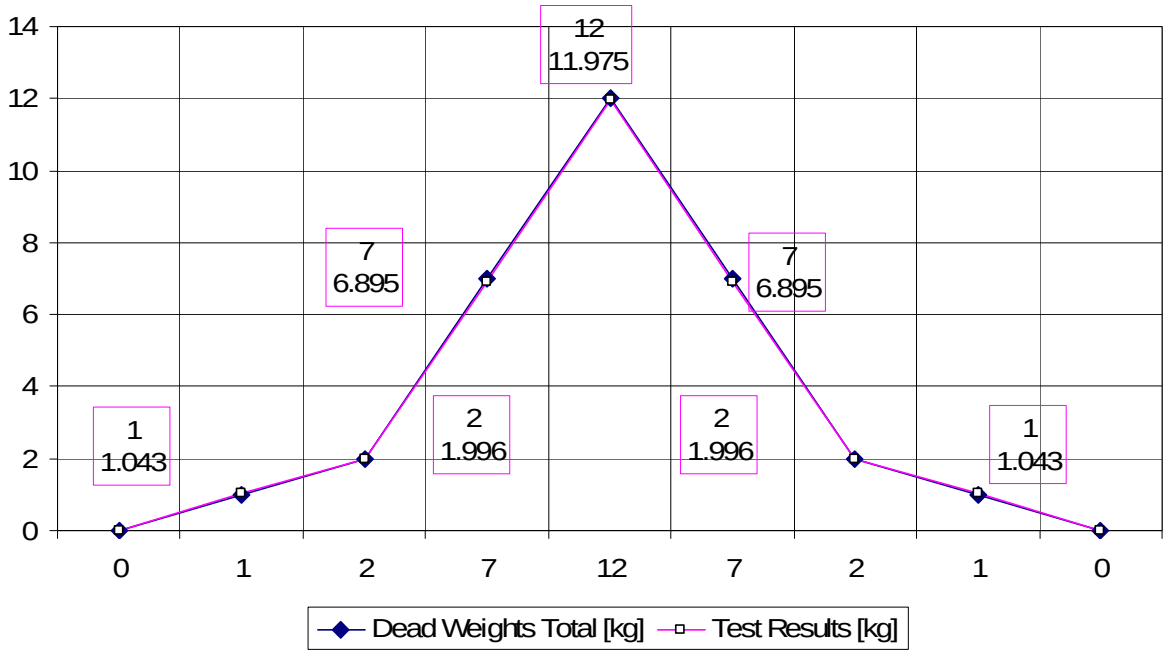

Figure A.7a Test Results vs. Dead Weights – Measurement No.4

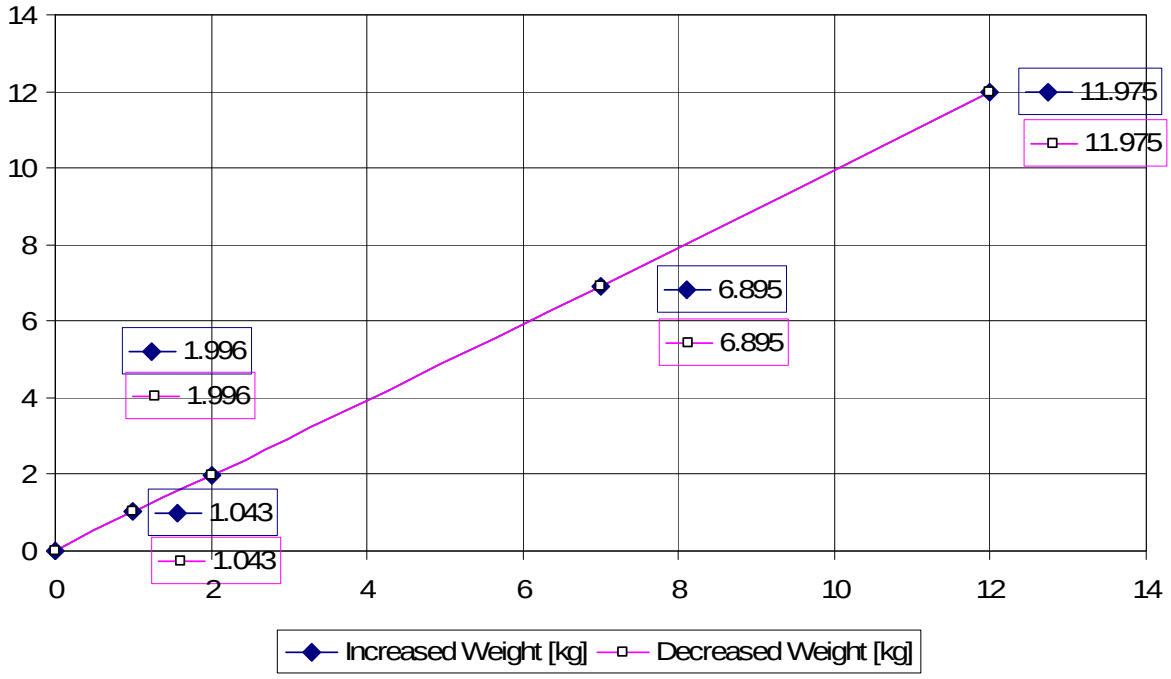

Figure A.7b Increased Weight vs. Decreased Weight – Measurement No.4

Standard Deviation

To be able to use all measurement values x'_i in the calculation of the standard deviation σ, they first had to be converted. The converted values are all related to a standard reference value of 1 kg. The following equations were used:

$$x_i = \frac{x'_i}{m_i} \tag{A.1}$$

$$\sigma = \sqrt{\frac{\sum_{i=1}^{n}(x_i - x_{dash})^2}{n-1}} \tag{A.2}$$

where

x_i = converted measurement value
x'_i = real measurement value
m_i = mass of dead weights in actual measurement
σ = standard deviation
x_{dash} = mean of converted measurement values
n = number of measurements

Table A.9 Results of Calculating Standard Deviation

x_{dash} [kg]	$\sum(xi-x_{dash})^2$ [kg]	n	σ [kg]	x_{dash} + σ [kg]	x_{dash} - σ [kg]
1.0067	0.0143	30	0.0222	1.0289	0.9845

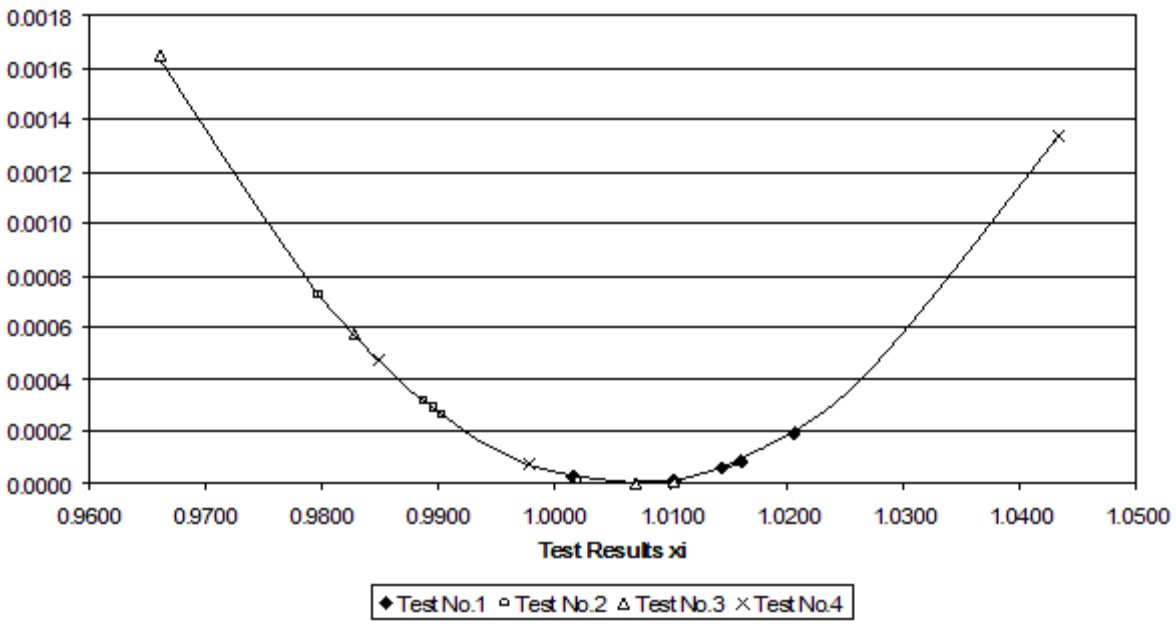

Figure A.8 Standard Deviation of Converted Measurement Values (Gauss)

Appendix B
Hacker Motor GmbH: A60-18M

Hacker Motor GmbH

Hummler Str. 5
Tel.: 0049 (0) 8761-752 129
Fax.:0049 (0) 8761-754 314
info@hacker-motor.com
D-85416 Niederhummel

Bedienungsanleitung für A60-Motoren
Operating Instructions for A60-Motors

Stand/*Revision*: 03/2006

1. Allgemeine Hinweise */ General Notes*

Alle Hacker-Brushless-Motoren sind bürstenlose Motoren. d.h., sie benötigen eine Kommutierung im Drehzahlsteller. Dafür sind die Drehzahlsteller der **MASTER-Serie und der X-Serie** vorgesehen.

Hacker Brushless Motors are as the name implies brushless motors requiring commutation, i.e. the conversion of direct current into alternating current, in the speed controller. Consequently they are intended for use with brushless sensorless speed controllers like the MASTER series and X-series controllers.

Ein Betrieb dieser Motoren mit herkömmlichen Drehzahlstellern für Bürstenmotoren oder mittels direktem Anschluß an eine Stromquelle ist deshalb nicht möglich. Eine solche Vorgehensweise wird den Hacker-Brushless-Motor zerstören.

The operation of Hacker Brushless Motors with conventional controllers intended for use with brushed motors, or when directly connected to an energy source like a battery pack or power supply, is therefore not permitted and will result in the destruction of the motor.

Achtung
Lesen Sie diese Anleitung sorgfältig durch Sie enthält für den Betrieb dieses Produkts unbedingt notwendige Hinweise
Caution
Please read these directions carefully. They contain important information ensuring long-term satisfaction with Hacker Brushless Motors products.

2. Technische Daten / Technical Specifications

Motor	***A60-S***			***A60-M***			***A60-L***			***Motor***
Ersetzt VerbrennerGröße	23ccm / 140 - size			26ccm / 160 - size			50.. 60ccm / 50..60cc			Equivalent to glow engine size
Leistungsbereich	max. 1900W (15 sec.)			max. 2200W (15 sec.)			max. 2600W (15 sec.)			Powerrange
E-Segler	bis 17kg / up to 37pounds			bis 20 kg / up to 45pounds			bis 25kg / up to 55pounds			Electric-Sailplane
Sport- und Scale	6..7,5kg / 13..16,5 pounds			7..9kg / 15..20 pounds			8..10kg / 17,5..22 pounds			Sport and Scale
Kunstflug und 3D	4..5kg / 8,5..11 pounds			5..6kg / 11..13 pounds			6..7kg / 13..15,5 pounds			Pattern and 3D
Hubschrauber	4..5kg / 8,5..11 pounds			5..6kg / 11..13 pounds			6..7kg / 13..15,5 pounds			Helicopter
Windungszahl	***20***	***22***	***24***	***16***	***18***	***20***	***14***	***16***	***18***	***Turns***
Empf. Prop-Größe	17x10 APC-E	20x10 APC-E	21x12 APC-EW	20x13 APC-E	21x14 APC-E	22x12 APC-E	20x10 ..21x14	20x13 ..22x12	21x12 ..24x12	Recommended Prop Range
Zellenzahl	8-10 LiPo	10 LiPo	10 LiPo	10..12 LiPo	10..12 LiPo	10..12 LiPo	10..14 LiPo	10..14 LiPo	10..14 LiPo	Cells
zulässiger Dauerstrom [A]	40A	40A	40A	42A	42A	42A	45A	45A	45A	Continuous Current [A]
kurzzeitiger Strom (15Sec) [A]	50A	50A	50A	55A	55A	55A	60A	60A	60A	Max. Burst Current (15s) [A]
Leerlaufstrom (Io) @8,4Volt [A]	1,7A	1,5A	1,3A	1,9A	1,8A	1,7A	2,5A	1,8A	1,6A	Idle Current (Io) @ 8,4Volt [A]
Innenwiderstand (Ri) [Ohm]	0,027	0,030	0,038	0,022	0,027	0,032	0,016	0,018	0,02	Resistance (Ri) [Ohm]
RPM/Volt (Kv)	245	217	195	215	190	180	192	168	149	RPM/Volt (Kv)
Prop-Adapter mit Spannzange	✓	✓	✓	✓	✓	✓	✓	✓	✓	Prop-Adaptor with cone
Befestigungsschrauben	✓	✓	✓	✓	✓	✓	✓	✓	✓	Screws
Lüfter	✓	✓	✓	✓	✓	✓	✓	✓	✓	Fan
Wellendurchm. D2	8,0 mm(0,315“)									Shaft Diameter D2
Wellenlänge L2	48,6mm / 1,91“									Shaftlenght L2
Gewicht	595g / 21,0oz			760g /26,7oz			910g / 32oz			Weight
Aussendurchm. D1	59 mm (23,3“)									Diameter D1
Länge L1	60,4mm / 2,38“			70,4mm / 2,77“			80,4mm / 3,17“			Length L1
Drehzahl max.	9.000									RPM max.

Achtung

Lesen Sie diese Anleitung sorgfältig durch Sie enthält für den Betrieb dieses Produkts unbedingt notwendige Hinweise

Caution

Please read these directions carefully. They contain important information ensuring long-term satisfaction with Hacker Brushless Motors products.

Lagerung	4 Kugellager / 4 Ballbearings			Bearings
Typ	14-Poliger Aussenläufer			Type
Drehzahlsteller	77..90 Amp Brushless	77..90 Amp Brushless	77..90 Amp Brushless	Speed Control
empf. Timing	20° - 25°			recomm. Timing
Schaltfrequenz	8 - 16 kHz			Switching Frequenzy

3. Der Einbau und Betrieb der Hacker-Brushless-Motoren / Mounting and Operation

° Bei der Befestigung der Hacker-Brushless-Motoren am vorderen Motorflansch ist unbedingt die maximal zulässige Einschraubtiefe zu beachten. Andernsfalls kann die Kupferwicklung durch die zu weit ins Gehäuse ragende Schrauben beschädigt werden.

ACHTUNG! Der beiligende Sperrholzspannt ist nur als BOHRSCHABLONE zu verwendet! Keinesfalls als Motorspannt verwenden!

Als Zubehör erhältlich ist ein stabiler Motorträger aus Aluminium für die A60-Motoren (BestNr: 15727618)

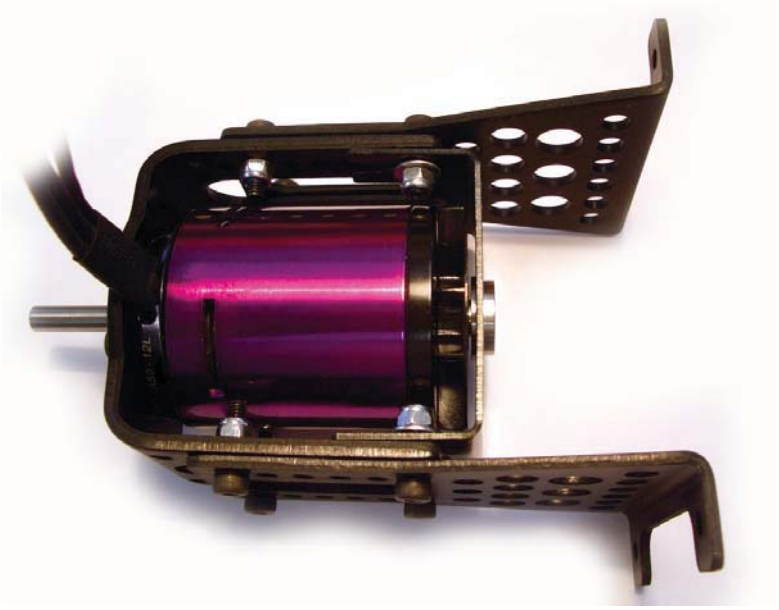

Care must be taken when using the forward mounting flange to mount the Hacker-Brushless- Motors not to exceed the following recommendations for screw protrusion into the motor's case. Using excessively long screws will damage the copper windings inside the motor!!!

DANGER! Use plywood-piece only for drilling your own motor-mount. Using this plywood-piece as motormount will destroy the plywood and can hurt you!

Please order the special A60-Aloy-Motormount which can handle the torque. OrderNr: 15727618

Achtung

Lesen Sie diese Anleitung sorgfältig durch Sie enthält für den Betrieb dieses Produkts unbedingt notwendige Hinweise

Caution

Please read these directions carefully. They contain important information ensuring long-term satisfaction with Hacker Brushless Motors products.

Motor	Gewinde / *Thread*	Teilkreisdurchmesser *Mountinghole diameter*	Max. Einschraubtiefe / *max. depth*
A60	M4	32,0mm	6,0mm

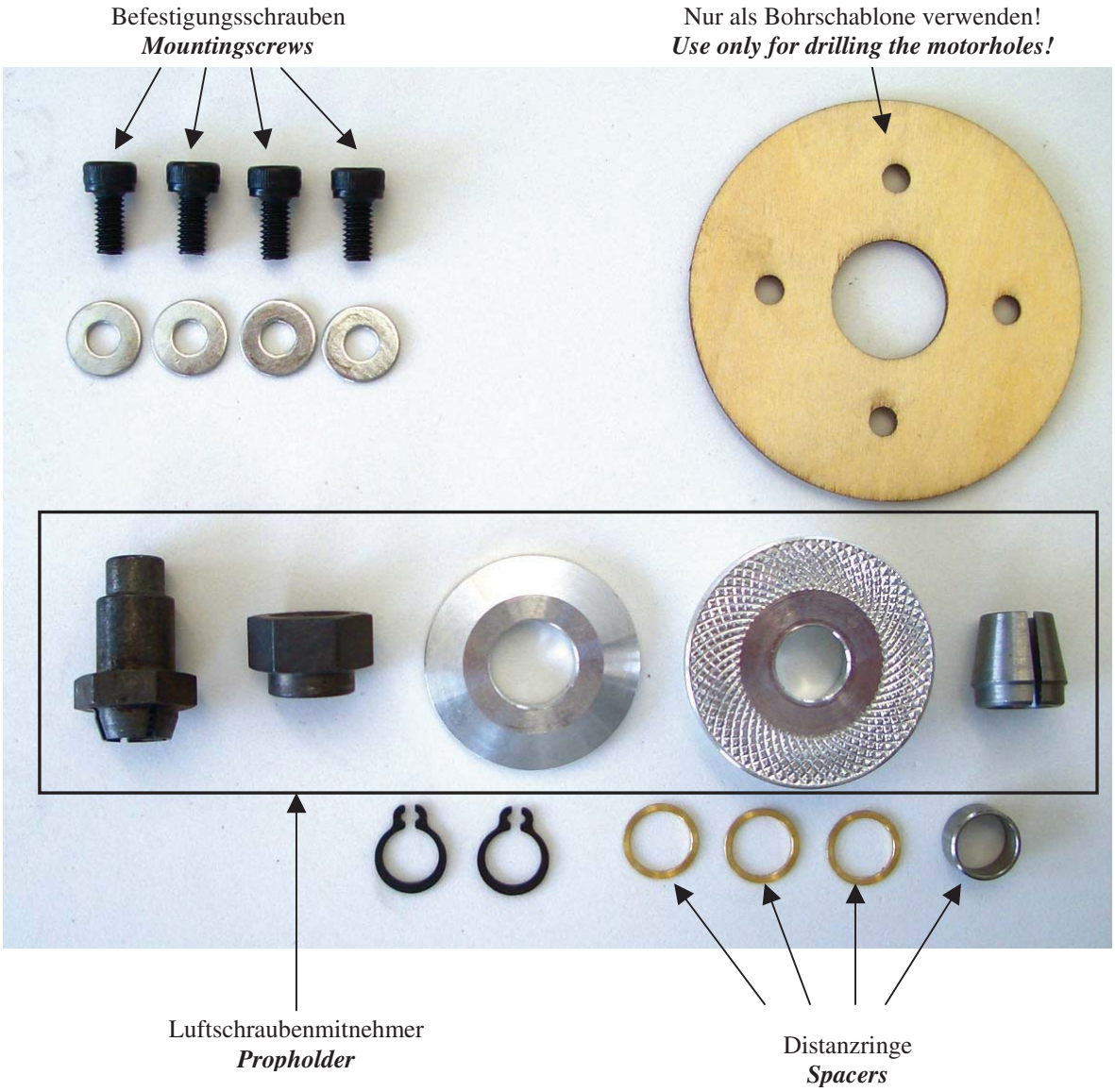

Achtung

Lesen Sie diese Anleitung sorgfältig durch Sie enthält für den Betrieb dieses Produkts unbedingt notwendige Hinweise

Caution

Please read these directions carefully. They contain important information ensuring long-term satisfaction with Hacker Brushless Motors products.

Montierter Propmitnehmer
Mounted Propholder

° Ein Elektromotor wird durch zu hohe Wärmeentwicklung zerstört. Die A60-Motoren sind bis 65 Grad Celsius temperaturfest. Darüber hinaus kann der Motor beschädigt werden. Auch wenn sich der Motor außen kalt anfühlt, kann die Wicklung deutlich heißer sein! Deshalb müssen zu hohe Temperaturen vermieden werden. Eine zu hohe Wärmeentwicklung tritt dann auf, wenn der Motor überlastet wird. Dies kann z.B. durch eine zu große Luftschraube, durch ein Blockieren der Motorwelle oder durch zu lang andauernde Einschaltdauer geschehen. Deshalb ist im Zweifelsfall immer zuerst eine kleinere Luftschraube (oder Schiffsschraube) zu erproben und dabei die Motortemperatur prüfen. Immer ist für eine wirkungsvolle Kühlung zu sorgen.

Excessively high temperatures will destroy an electric motor. Hacker Brushless Motors are designed for operating temperatures up to 65°C (149°F). Temperatures exceeding this level can lead to motor damage and should be avoided. Excessive temperatures result from overloading the motor and may arise from using an excessively large propeller, an obstructed or jammed motor shaft, or excessively long motor startup times. Therefore it is better to err on the side of caution and begin with a smaller propeller and check the motors temperature. Effective cooling must always be ensured.

° Den Motor keinesfalls im Leerlauf ohne Last betreiben! Der Motor kann auch durch nur kurzzeitige sehr hohe Drehzahlen zerstört werden.

Do not run the motor without an adequate load. The motor can be quickly destroyed by excessively high RPM and free running!

Achtung
Lesen Sie diese Anleitung sorgfältig durch Sie enthält für den Betrieb dieses Produkts unbedingt notwendige Hinweise
Caution
Please read these directions carefully. They contain important information ensuring long-term satisfaction with Hacker Brushless Motors products.

4. Bitte folgende Sicherheitshinweise unbedingt beachten / Please follow these safety precautions

° Die maximal zulässige Motordrehzahl beträgt bei den A60-Motoren 9000U/min. Sie sollte aus Sicherheitsgründen nicht
überschritten werden. Bei Verwendung eines Getriebes ist zu beachten, dass die Motordrehzahl um den Faktor der Getriebeübersetzung über der Luftschraubendrehzahl liegt

The maximum allowable motor speed on the A60-motors is 9,000 revolutions per minute. For safety's sake, care must be taken not to exceed this limit. When using a gearbox, take into consideration that the motor rpm may be calculated by multiplying the propeller rpm by the gearbox ratio.

° Sobald ein Antriebsakku angeschlossen ist, besteht die Möglichkeit, dass der Motor anläuft (z.B. durch
Fehlbedienung oder durch elektrischen Defekt). Deshalb ist von diesem Zeitpunkt an höchste Vorsicht geboten.

Since it is possible for an electric motor to start following connection to a battery (for example from improper operation, an electrical defect, or interference), Extreme caution must be exercised upon making this connection!

° Ein Elektromotor (speziell mit Luftschraube) kann erhebliche Verletzungen verursachen. Ebenso können durch fortfliegende Teile erhebliche Verletzungen hervorgerufen werden.

Electric motors have the potential to cause injury. This risk increases when the motor is rotating a propeller that may also strike and propel other objects.

° Der Betrieb der Hacker-Brushless-Motoren ist deshalb nur in Situationen zulässig, in denen Sach- und Personenschäden ausgeschlossen sind.

Hacker Brushless Motors may only be used when the potential for personal and property damage has been eliminated.

° Einen beschädigten Motor (z.B. durch mechanische oder elektrische Einwirkung, durch Feuchtigkeit usw.) keinesfalls weiter verwenden. Anderenfalls kann es zu einem späteren Zeitpunkt zu einem plötzlichen Versagen des Motors kommen.

A damaged motor (for example electrical, mechanical or moisture damage) may not under any circumstances continue to be used. Doing so may result in sudden motor damage in the future.

° Die Hacker-Brushless-Motoren sind nur zum Einsatz in Umgebungen vorgesehen, in denen keine Entladung von statischer Elektrizität auftritt.

Hacker Brushless Motors may only be used in an environment free from the risk of static electrical discharges.

Achtung
Lesen Sie diese Anleitung sorgfältig durch Sie enthält für den Betrieb dieses Produkts unbedingt notwendige Hinweise
Caution
Please read these directions carefully. They contain important information ensuring long-term satisfaction with Hacker Brushless Motors products.

° Die Hacker-Brushless-Motoren dürfen nur aus Akkumulatoren (über geeignete Drehzahlsteller, siehe oben) gespeist werden, ein Betrieb an Netzgeräten ist nicht zulässig. Es darf in keinem Falle eine elektrische Verbindung zwischen dem Hacker-Brushless-Motor und dem 230V Wechselstromnetz hergestellt werden.

Hacker Brushless Motors may only be supplied with electricity from batteries connected to an appropriate brushless controller (see above). The connection to a power supply is not permitted. Under no circumstances should a Hacker Brushless Motor be connected to an electrical network based on alternating current (e.g. 100-230V).

Ein Einsatz in Manntragenden Flug- oder Fahrzeugen ist nicht gestattet.

The use of these motors in man-carrying vehicles, whether airborne or otherwise, is not permitted.

5. CE-Richtlinien / CE Guidelines

Die beschriebenen Produkte genügen den einschlägigen und zwingenden EG-Richtlinien:
EMV-Richtlinen 89/336/EWG
92/31/EWG
93/68/EWG.

The described products are manufactured in compliance with the relevant and applicable CE Guidelines:

Electromagnetic compatibility: EMI89/336/EEC, 92/31/EEC, 93/68/EEC

Sollten Sie dennoch Empfangsprobleme haben, so liegen diese oftmals an der fehlerhaften Zusammenstellung der Komponenten oder dem unbedachten Einbau der Empfangskomponeneten.

Interference or range problems are most likely caused by unsuitable combinations of RC products and/or incorrect installations.

. Garantiebedingungen / Warranty Terms and Conditions

Wir gewähren 24 Monate Garantie auf dieses Produkt. Alle weitergehenden Ansprüche sind ausgeschlossen.
Dies gilt insbesondere für Schadensersatzansprüche die durch Ausfall oder Fehlfunktion ausgelöst wurden. Für Personenschäden, Sachschäden und deren Folgen, die aus unserer Lieferung oder Arbeit entstehen, übernehmen wir keine Haftung (außer bei grober Fahrlässigkeit oder Vorsatz), da uns eine Kontrolle der Handhabung und der Anwendung nicht möglich ist.

Achtung

Lesen Sie diese Anleitung sorgfältig durch Sie enthält für den Betrieb dieses Produkts unbedingt notwendige Hinweise

Caution

Please read these directions carefully. They contain important information ensuring long-term satisfaction with Hacker Brushless Motors products.

Hacker Brushless Motors are covered by a 24-month warranty. Additional claims are explicitly prohibited. This is especially true for claims for damages arising from failure or faulty operation. Hacker Brushless Motors specifically excludes any and all claims for personal injury, property damage or consequential damages resulting from the use of our products or arising from our workmanship (apart from gross negligence or malice), as Hacker Brushless Motors has no control over the operation or use of said products.

Hacker Motor GmbH

Benutzerinformationen zur Entsorgung von elektrischen Geräten und elektronischen Geräten (private Haushalte)
Entsprechend der grundlegenden Firmengrundsätzen der Panasonic-Gruppe wurde ihr Produkt aus hochwertigen Materialen hergestellt, die recycelbar und wieder verwendbar sind.
Dieses Symbol auf Produkten und/oder begleitenden Dokumenten bedeutet, dass elektrische und elektronische Produkte am Ende Ihrer Lebensdauer vom Hausmüll getrennt entsorgt werden müssen.
Bringen Sie bitte diese Produkte für die Behandlung, Rohstoffrückgewinnung und Recycling zu den eingerichteten kommunalen Sammelstellen bzw. Wertstoffsammelhöfen, da diese Geräte kostenlos entgegennehmen.
Die Ordnungsgemäße Entsorgung dieses Produkts dient dem Umweltschutz und verhindert mögliche schädliche Auswirkungen auf Mensch und Umwelt, die sich aus einer unsachgemäßen Handhabung der Geräte am Ende ihrer Lebensdauer ergeben könnten.
Genauere Informationen zur nächstgelegenen Sammelstelle bzw. Recyclinghof erhalten Sie bei Ihrer Gemeindeverwaltung.
Für Geschäftskunden in der Europäischen Union
Bitte treten Sie mit Ihrem Händler oder Lieferanten in Kontakt, wenn Sie elektrische und elektronische Geräte entsorgen möchten. Er hält weitere Informationen für Sie bereit.
Informationen zur Entsorgung in Ländern ausserhalb der Europäischen Union.
Dieses Symbol ist nur in der Europäischen Union gültig.

Information on Disposal for Users of Waste Electrical and Electronic Equipment (private households)
This symbol on the products and/or accompanying documents means that used electrical and electronic products should not be mixed with general household waste.
For proper treatment, recovery and recycling, please take these products to designated collection points, where they will be accepted on a free of charge basis.
Alternatively, in some countries you may be able to return your products to your local retailer upon the purchase of an equivalent new product.
Disposing of this product correctly will be help to save valuable resources and prevent any potential negative effects on human health and the environment which could otherwise arise from inappropriate waste handling. Please contact your local authority for further details of your nearest designated collection point.
Penalties may be applicable for incorrect disposal of this waste, in accordance with national legislation.
For business user in the European Union
If you wish to discard electrical and electronic equipment, please contact your dealer or supplier for further information.
Information on Disposal in other Countries outside the European Union
This symbol is only valid in the European Union.
If you wish to discard this product, please contact your local authorities or dealer and ask for the correct method of disposal.

CE

Made in China

Eine Gewähr für den Inhalt dieser Drucksache, insbesondere für die Richtigkeit der Maße, technischen Daten und Messwerte wird nicht übernommen.

Achtung
Lesen Sie diese Anleitung sorgfältig durch Sie enthält für den Betrieb dieses Produkts unbedingt notwendige Hinweise
Caution
Please read these directions carefully. They contain important information ensuring long-term satisfaction with Hacker Brushless Motors products.

Appendix C
Plettenberg Elektromotoren: HP370/50/A3

High End Elektromotoren
PLETTENBERG

Bürstenmotoren
Übersicht

Brushlessmotoren
Übersicht
Motor - Regler

Außenläufer
Übersicht
Motor - Regler

Zubehör
Getriebe

Maße/Gewichte | Luftschrauben | Datenblätter | Motor | Startseite

HP 370/50

Die Motoren der Serie **HP 370** sind zehnpolige bürstenlose Direktantriebe. Durch die hochpolige Bauweise konnte der Innenwiderstand gesenkt und somit das Drehmoment erhöht werden. Dadurch wurde es möglich, einen Motor mit niedrigem Gewicht, hohem Drehmoment, niedriger Drehzahl und enormer Belastbarkeit zu konstruieren.

Es ergibt sich ein hervorragendes Gewichts-Leistungs Verhältnis. In der drehzahlfesten S-Variante sind die Rotoren kevlararmiert und halten so sehr hohen Drehzahlen stand. Somit sind diese Motoren als Getriebe-, Impeller- und Bootsantriebe einsetzbar. Die Motoren sind mit 8/12mm Welle mit Luftschraubenkupplung erhältlich.

Motor	Modell	Zellen	Prop	max.Eta
HP 370/50/A3	Motormodelle	20 - 36	15" - 20"	89%
HP 370/50/A3	Großsegler	20 - 30	17" - 22"	89%
HP 370/50/A2	Motormodelle	20 - 28	14" - 18"	87%
HP 370/50/A2	Großsegler	20 - 26	15" - 20"	87%

High End Elektromotoren
PLETTENBERG

Bürstenmotoren
Übersicht
Brushlessmotoren
Übersicht
Motor - Regler
Außenläufer
Übersicht
Motor - Regler
Zubehör
Getriebe

Maße/Gewichte | Luftschrauben | Datenblätter | Motor | Startseite

HP 370/50

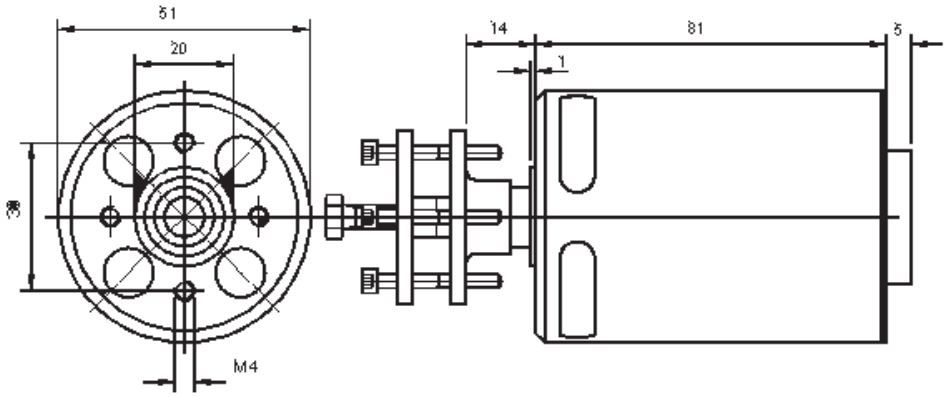

HP 370/50	
Gewicht ca:	**625 g incl. Luftschraubenkupplung**
Wellendurchmesser:	**8/12 mm**
Zellenzahl:	**20 - 36 Zellen**

Bürstenmotoren
Übersicht
Brushlessmotoren
Übersicht
Motor - Regler
Außenläufer
Übersicht
Motor - Regler
Zubehör
Getriebe

Maße/Gewichte | Luftschrauben | Datenblätter | Motor | Startseite

HP 370/50

HP 370/50/A1 S

Leerlaufdrehzahl / Volt: 815 1/min | **Leerlaufstrom bei ca. 11 V: 4,4 A**

HP 370/50/A2

Leerlaufdrehzahl / Volt: 350 1/min | **Leerlaufstrom bei ca. 11 V: 1,8 A**

Luftschraube:	Spannung in V	Strom in A	Drehzahl 1/min	Eta.max%	Schub in N
APC 15x10"	22,2	36,5	7050	87	38,3
	24,1	41,8	7560	86,5	44,1
	26,2	50,0	8250	86,5	53,0
	28,4	56,1	8710	85	58,9
APC 16x10"	20,1	39,1	6510	86	41,2
	22,7	45,4	7010	85,5	48,1
	24,5	51,8	7440	84,5	54,0
	26,6	59,8	8050	83,5	63,8

HP 370/50/A3

Leerlaufdrehzahl / Volt: 235 1/min | **Leerlaufstrom bei ca. 11 V: 1,1 A**

Luftschraube:	Spannung in V	Strom in A	Drehzahl 1/min	Eta.max%	Schub in N
APC 16x10"	29,8	23,6	6260	88,5	38,3
	32,2	27,1	6700	88	43,2
	34,4	30,5	7120	88	4,9
Menz S 18x10"	26,2	30,7	5240	86	44,1
	28,0	34,3	5550	85,5	49,1
	30,0	38,3	5900	84,5	56,9
	32,0	42,8	6250	83,5	63,8
Menz S 20x10"	23,7	31,8	4690	85	47,1
	27,3	39,7	5210	83	58,9
	29,3	45,3	5570	80,5	66,7

Appendix D
National Advisory Committee for Aeronautics (NACA): Technical Note No. 698

TECHNICAL NOTES

NATIONAL ADVISORY COMMITTEE FOR AERONAUTICS

No. 698

PROPELLER TESTS TO DETERMINE THE EFFECT OF NUMBER OF BLADES AT TWO TYPICAL SOLIDITIES

By E. P. Lesley
Daniel Guggenheim Aeronautical Laboratory
Stanford University

Washington
April 1939

NATIONAL ADVISORY COMMITTEE FOR AERONAUTICS

TECHNICAL NOTE NO. 698

PROPELLER TESTS TO DETERMINE THE EFFECT OF NUMBER OF BLADES AT TWO TYPICAL SOLIDITIES

By E. P. Lesley

SUMMARY

Propellers with equal total blade area, but with different numbers of blades, were tested at Stanford University.

The tests show generally that, for equal total blade area, propellers with the larger number of blades absorb the greater power and, provided hubs have equal drag, develop the higher efficiency.

It is shown that the differences found are in agreement, qualitatively, with what might be predicted from simple blade-element theory.

INTRODUCTION

The simple blade-element theory as developed by Drzewiecki shows that between two propellers with similar blade plan forms and blade section profiles and with equal total blade area, but with different numbers of blades, the power absorbed and the efficiency developed by the propeller with the larger number of blades should be the greater. The larger power absorption would be expected from the increased lift coefficients for blade elements of higher aspect ratio. A gain in efficiency should arise from increased L/D of blade elements.

In the practical case, unless the aerodynamic superiority of the many-blade propeller is considerable, the propeller with fewer and wider blades might be chosen, since, particularly for the controllable-pitch propeller, the mechanical features will be less complicated and the original cost no doubt smaller.

At the request and with the financial assistance of the National Advisory Committee for Aeronautics, the subsequently described experimental study was undertaken. The purpose was to determine by test the quantitative differences in aerodynamic characteristics between two- and three-blade propellers having equal total blade areas, and between three- and four-blade propellers, again having equal total blade areas but, in this case, 33-1/3 percent more area than for the two-blade -- three-blade comparison.

APPARATUS AND TESTS

Wind tunnel.- The experiments of this investigation were carried on in the wind tunnel of the Daniel Guggenheim Aeronautical Laboratory at Stanford University. The tunnel is of the Eiffel type with open throat 7-1/2 feet in diameter. The maximum wind velocity is 90 miles per hour.

Dynamometer.- The propeller dynamometer consists essentially of an electric motor carried on axially disposed, thin, steel plate knife edges. The propeller is secured to an extension of the motor shaft. The extension is free from axial constraint except that provided by a beam balance which measures the pull upon the shaft or the propeller thrust. The propeller torque is measured by the counter moment, indicated by a beam balance, required to restrain the driving motor against roll about the knife edges that support it. The propeller is placed well forward, about one and one-half diameters, of any considerable slipstream obstruction.

Model propellers.- The propellers were all 3-foot diameter, metal, adjustable-pitch models. The blade plan forms are shown in figure 1; the propeller hubs are shown in figure 2.

Blade E (fig. 1) has the plan form, blade angles and sections of propeller E in reference 1. The aspect ratio is 7.7. The nominal pitch-diameter ratio is 0.7 from 0.6 R outward to the tip. It gradually decreases from 0.6 R toward the hub to 0.42 at 0.15 R.

Blade E' is 33-1/3 percent wider and thicker than blade E. The aspect ratio is 5.77.

Blade E" is 50 percent wider and thicker than blade E. The aspect ratio is 5.13.

A two-blade propeller with E" blades thus has the same total area as a three-blade propeller with E blades. Likewise a three-blade propeller with E' blades has the same total area as a four-blade propeller with E blades.

Distribution along the radius of geometrical pitch-diameter ratio, width-diameter ratio, and thickness-width ratio for the three blade forms is shown in figure 3.

Tests were made of all propellers for blade angles at 0.75 R of 15°, 25°, 35°, and 45°.

Following the Stanford laboratory practice, a constant angular velocity was employed for all tests at a given blade angle. Variation in the parameter V/nD was brought about through change in the wind velocity. Because of limitations in wind speed and in power and rotational speeds available in the dynamometer, the rotational speeds employed were 2,000, 1,800, 1,500, and 1,000 revolutions per minute for the 15°, 25°, 35°, and 45° blade angles, respectively. The Reynolds Number of the tests was thus from 0.11 to 0.06 that of flight, assuming full-scale propellers 9 feet in diameter turning at 2,000 revolutions per minute.

The observed quantities of the tests, thrust, torque, rotational speed, velocity of advance, and density, were converted into the usual coefficients:

Thrust coefficient,

$$C_T = \frac{T}{\rho\, n^2\, D^4}$$

Power coefficient,

$$C_P = \frac{P}{\rho\, n^3\, D^5} = \frac{2\,\pi\, Q}{\rho\, n^2\, D^5}$$

Speed-power coefficient,

$$C_s = V\sqrt[5]{\frac{\rho}{P\, n^2}} = \frac{V}{nD}\sqrt[5]{\frac{1}{C_P}}$$

where

T is propeller thrust.

ρ, mass density of the air.

n, revolutions per unit time.

D, propeller diameter.

Q, propeller turning moment or torque.

P, power absorbed.

V, velocity.

RESULTS AND DISCUSSION

The coefficients derived from the observations of the tests are given in table I. In figures 4 to 7, C_T, C_P, and η are represented graphically as functions of V/nD.

Figures 4 and 5 show that, between two- and three-blade propellers of equal total blade area, there are appreciable differences in performance. The C_T and C_P curves for the three-blade propellers show a higher slope than corresponding curves of the two-blade propellers. From simple blade-element theory, C_T and C_P depend largely upon the lift coefficients of the blade elements. Curves of lift coefficients as functions of geometrical angle of attack will have higher slope for elements of greater aspect ratio. A higher slope in curves of C_T and C_P as functions of V/nD for the three-blade, greater aspect ratio propellers is therefore to be expected since, for a given blade setting, V/nD determines the geometrical angles of attack of the blade elements.

In the usual operating range, from V/nD for maximum efficiency to about 0.75 V/nD for maximum efficiency, the three-blade propellers develop from 2 to 8 percent more thrust and absorb a correspondingly greater power so that the differences in efficiency are barely noticeable. The differences in efficiency appear to be in favor of the three-blade propellers in some cases but in others the reverse is true.

The dynamic pitch-diameter ratio (V/nD for zero thrust) is larger in all cases for the two-blade than for the three-blade propellers. This result was believed to be evidence that the drag of the three-blade hub was considerably more than that of the two-blade hub. The blades had identical forms of section profiles. At zero thrust, the lift coefficients of the elements are too small to be significantly affected by the variation in aspect ratio. Therefore, unless the drags of the hubs were different, the V/nD for zero thrust would be the same for both propellers.

For the 25°, 35°, and 45° blade angles at 0.75 R, it may be seen that both two-blade and three-blade propellers show pronounced changes in the direction of the C_T and C_p curves at certain points, with resulting sudden increases in the slope of the efficiency curves. The values of V/nD at which the change occurs are about 0.4, 0.9, and 1.5 for the 25°, 35°, and 45° blade angles, respectively. The angle of attack for the tip section of the propellers is thus very close to 14°, which is near the burble point for sections of this type. (See reference 2.) It may be noted that the burbled tip condition, as evidenced by the sudden change in slope of the efficiency curves, occurs for the two-blade propellers at lower values of V/nD than for the three-blade propellers. The two-blade propellers thus show appreciably greater efficiency near this point. For example, the two-blade, 35° propeller shows an efficiency of 0.75 at V/nD = 0.95. That of the three-blade propeller for the same V/nD is 0.70. Outside of this region, however, and except at values of V/nD greater than that for maximum efficiency, neither two- nor three-blade propeller shows a consistent advantage in efficiency.

The qualitative difference in V/nD for burble of wide and narrow blade propellers may be explained, as has been the difference in slope of C_T and C_p curves, by consideration of the blades as made up of airfoil elements of different aspect ratios. The wider blades (smaller aspect ratio) have, for given geometrical angles of attack, larger induced angles of attack and thus smaller effective angles of attack.

Burble will occur at the same effective angles of attack for both wide and narrow blades and therefore at larger geometrical angles of attack (smaller V/nD) for the wider blades.

Calculation of the difference in geometrical angle of attack at burble for elliptically loaded airfoils, having the aspect ratios of the two- and the three-blade propellers of equal total blade area, gives about 1°. This value is close to what is shown by the change in V/nD for burble in the propeller tests.

It appeared that the later tip burble in the two-blade propellers might be partly explained by difference in Reynolds Number. A subsequent test of the two-blade, 35° propeller at two-thirds the angular velocity formerly employed, and thus at the same Reynolds Numbers as for the three-blade propeller, however, gave practically the identical curves for C_T, C_P, and η formerly derived.

During the tests, a pronounced change in the sound of the propellers was observed at burble. Before burble they were relatively quiet, giving off only a high-pitch hissing sound. At burble and thereafter, the sound was manyfold louder, of lower pitch, and similar to that of tearing cloth.

Comparison of figures 6 and 7 shows somewhat similar differences between three- and four-blade propellers of equal total blade area as are evident in the two-blade--three-blade comparison.

The thrust and the power coefficients are generally greater for four-blade propellers than for three-blade propellers but the difference is considerably less than shown between three-blade and two-blade propellers.

The efficiency of the four-blade propellers appears to be from zero to 2 percent greater than for the three-blade propellers.

The dynamic pitch-diameter ratio (V/nD for zero thrust) is generally somewhat less for the four-blade propellers than for the three-blade propellers. The difference is smaller and less consistent than for the two-blade--three-blade comparison.

As previously stated, the simple blade-element theory shows that, other things being equal, there should be an increase in power absorbed and in efficiency developed for the propellers with the larger number of blades.

In order to estimate the qualitative differences that

might be expected the following computations were carried through.

1. The lift and the drag coefficients for the 0.75 R section (given in reference 2) were transformed to coefficients for airfoils of the aspect ratios represented in the model propeller blades.

2. Computations were made of quantities corresponding to C_p and η of the 0.75 R element of the 35° propellers at V/nD = 1.3 (maximum efficiency).

Assuming that the computed coefficients derived for the 0.75 R section would be relatively representative of the propeller as a whole, it was predicted that the three-blade E propeller would absorb about 7 percent more power and develop 2 percent greater peak efficiency than the two-blade E" propeller. Likewise the four-blade E propeller would absorb about 4 percent more power and develop 1.6 percent greater peak efficiency than the three-blade E' propeller.

Smaller V/nD for zero thrust, as shown by the three-blade E propeller in comparison with the two-blade E" propeller and the failure of the three-blade propeller to realize in test an increase in efficiency led to further tests. These tests were thought desirable because the predicted increase in efficiency of the four-blade E propeller over that of the three-blade E' propeller appeared to have been shown.

The drags of the two-, three-, and four-blade hubs and propeller shaft (hubs without blades being placed on the shaft and rotated at propeller speed) were measured. It was found that the drag of the three-blade hub and shaft was more than double that of the two-blade hub and shaft. The drag of the four-blade hub and shaft was about 18 percent more than that of the three-blade hub and shaft.

It was seen that the difference in drag of two- and three-blade hubs and shafts might account for the failure of the three-blade E propeller to realize the 2 percent greater peak efficiency predicted for it. In order to confirm this explanation, identical spinners were fitted over the hubs of two- and three-blade propellers (as shown in figure 8 for the two-blade propeller) and tests were made for the 35° blade angle. Observations reduced to coefficient form are given in table II and are shown graphic-

ally in figure 9. From this figure it may be seen that the 2 percent greater peak efficiency predicted for the three-blade propeller is realized and that V/nD for zero thrust of the two propellers is the same.

Comparison of the C_T curves of figure 8 with the 35° C_T curves of figures 4 and 5 and in the region of maximum efficiency (V/nD 1.1 to 1.4) reveals that the thrust realized from the propellers with spinners is appreciably greater than for those with bare hubs. The increase in thrust for the two-blade propeller is about 1-1/2 percent, while that for the three-blade propeller is about 3-1/2 percent. Since there are only insignificant differences between power coefficients, with and without spinners, the net result is that the three-blade propeller shows 2 percent greater peak efficiency than the two-blade propeller when identical spinners are fitted over the hubs, while with bare hubs there is no consequential difference between them.

The increase of efficiency of the two-blade propeller through the addition of a spinner was somewhat surprising since, at first glance, it appeared that the drag of the spinner would be at least equal to that of the two-blade hub. A drag test like that employed to measure the comparative drags of two-, three-, and four-blade hubs showed, however, that the drag of the spinner and the shaft was not more than one-third of that of the two-blade hub and shaft. The increase in efficiency found was thus easily accounted for.

It would appear that, if spinners had been fitted in the four-blade--three-blade comparison, a further addition to efficiency in favor of the four-blade propellor might have been found. As compared with what was found for the three-blade--two-blade comparison, the addition would, however, have been small because the difference in drag between three- and four-blade hubs and shafts was only one-third of that between two- and three-blade hubs and shafts.

CONCLUSION

These tests show that, for a given diameter and total blade area provided other things are equal, the propeller

with the largest number of blades will absorb the greatest power and develop the highest efficiency.

Daniel Guggenheim Aeronautical Laboratory,
Stanford University, December 10, 1938.

REFERENCES

1. Losley, E. P., and Reid, Elliott G.: Tests of Five Metal Model Propellers with Various Pitch Distributions in a Free Wind Stream and in Combination with a Model VE-7 Fuselage. T.R. No. 326, N.A.C.A., 1929.

2. Weick, Fred E.: Aircraft Propeller Design. McGraw-Hill Book Co., Inc., 1930.

Table 1
Continued on
following
pages

TABLE I

Three-Blade E Propeller

15° at 0.75 R

V/nD	C_T	C_P	C_s	η
0.734	0.0020	0.0120	1.780	0.122
.679	.0178	.0204	1.478	.592
.631	.0292	.0266	1.304	.693
.593	.0379	.0307	1.191	.732
.548	.0483	.0355	1.089	.745
.506	.0576	.0394	.966	.739
.473	.0646	.0422	.891	.724
.425	.0748	.0452	.790	.703
.370	.0833	.0473	.681	.651
.326	.0905	.0485	.597	.607
.254	.1007	.0497	.463	.514

TABLE I - Continued

Three-Blade E Propeller

25° at 0.75 R

V/nD	C_T	C_P	C_s	η
1.166	0.0024	0.0216	2.511	0.130
1.125	.0174	.0349	2.198	.560
1.059	.0316	.0478	1.946	.700
1.007	.0457	.0598	1.779	.770
.982	.0549	.0673	1.651	.784
.912	.0636	.0752	1.540	.797
.868	.0733	.0795	1.442	.800
.817	.0819	.0846	1.339	.791
.783	.0888	.0886	1.272	.785
.738	.0962	.0921	1.190	.771
.689	.1049	.0959	1.102	.754
.628	.1155	.0997	.996	.727
.585	.1215	.1011	.925	.704
.541	.1279	.1021	.854	.677
.479	.1344	.1042	.753	.617
.419	.1375	.1038	.659	.554
.354	.1374	.1098	.551	.443

TABLE I - Continued

Three-Blade E Propeller

35° at 0.75 R

V/nD	C_T	C_P	C_s	η
1.625	0.0172	0.0613	2.840	0.457
1.586	.0300	.0778	2.642	.612
1.523	.0449	.0964	2.431	.709
1.468	.0556	.1083	2.290	.752
1.409	.0668	.1200	2.152	.784
1.361	.0760	.1278	2.053	.809
1.297	.0868	.1387	1.926	.812
1.251	.0972	.1481	1.805	.808
1.171	.1069	.1554	1.700	.805
1.111	.1168	.1624	1.598	.798
1.051	.1233	.1667	1.505	.777
.999	.1290	.1720	1.421	.749
.939	.1298	.1770	1.328	.689
.880	.1316	.1781	1.243	.650
.801	.1333	.1798	1.128	.594
.728	.1358	.1836	1.022	.538
.646	.1383	.1850	.905	.983

TABLE I - Continued

Three-Blade E Propeller

45° at 0.75 R

V/nD	C_T	C_P	C_s	η
2.247	0.0378	0.1380	3.340	0.615
2.188	.0485	.1554	3.174	.683
2.103	.0626	.1775	2.971	.748
2.025	.0753	.1962	2.802	.777
1.944	.0876	.2137	2.647	.797
1.856	.0997	.2291	2.491	.807
1.763	.1120	.2439	2.340	.810
1.681	.1221	.2557	2.210	.803
1.599	.1298	.2648	2.087	.784
1.511	.1315	.2689	1.966	.739
1.420	.1319	.2676	1.850	.700
1.335	.1328	.2674	1.739	.662
1.261	.1340	.2685	1.642	.629
1.181	.1356	.2681	1.538	.597
1.112	.1369	.2694	1.448	.566
1.043	.1385	.2706	1.356	.534
.982	.1401	.2728	1.275	.504
.874	.1425	.2775	1.121	.449
.790	.1453	.2828	1.014	.406

TABLE I - Continued

Two-Blade E" Propeller

15° at 0.75 R

V/nD	C_T	C_P	C_s	η
0.763	0.0011	0.0101	1.915	0.085
.705	.0158	.0185	1.565	.602
.655	.0271	.0246	1.375	.722
.611	.0352	.0287	1.244	.749
.565	.0443	.0331	1.118	.755
.516	.0536	.0370	.998	.748
.451	.0657	.0411	.854	.721
.416	.0722	.0436	.779	.689
.377	.0777	.0448	.702	.654
.328	.0852	.0462	.607	.605
.275	.0936	.0480	.505	.536

TABLE I - Continued

Two-Blade E" Propeller

25° at 0.75 R

V/nD	C_T	C_P	C_s	η
1.190	0.0045	0.0208	2.582	0.258
1.128	.0173	.0325	2.241	.604
1.078	.0293	.0425	2.027	.744
1.022	.0399	.0515	1.850	.792
.971	.0495	.0597	1.708	.805
.909	.0610	.0686	1.554	.808
.863	.0696	.0750	1.448	.801
.803	.0785	.0805	1.329	.782
.754	.0871	.0850	1.237	.772
.710	.0944	.0888	1.153	.755
.660	.1027	.0924	1.065	.734
.619	.1100	.0953	.991	.714
.574	.1163	.0968	.916	.689
.528	.1226	.0976	.838	.661
.475	.1305	.0990	.754	.626
.427	.1362	.0990	.678	.587
.390	.1415	.0995	.619	.554
.336	.1402	.1092	.523	.432
.249	.1428	.1135	.385	.313

TABLE I - Continued

Two-Blade E" Propeller

35° at 0.75 R

V/nD	C_T	C_P	C_s	η
1.625	0.0229	0.0625	2.830	0.596
1.570	.0344	.0764	2.625	.706
1.508	.0449	.0890	2.446	.760
1.454	.0545	.1006	2.301	.788
1.397	.0644	.1115	2.168	.807
1.318	.0767	.1244	2.000	.812
1.267	.0850	.1323	1.899	.814
1.202	.0941	.1403	1.781	.806
1.145	.1020	.1463	1.684	.799
1.114	.1066	.1502	1.627	.791
1.081	.1118	.1535	1.573	.787
1.051	.1158	.1560	1.525	.780
1.015	.1206	.1588	1.466	.771
.983	.1247	.1608	1.417	.762
.953	.1286	.1635	1.370	.750
.921	.1325	.1670	1.318	.731
.891	.1324	.1733	1.266	.681
.860	.1338	.1756	1.218	.655
.785	.1358	.1788	1.106	.596
.717	.1388	.1803	1.010	.552
.666	.1431	.1841	.935	.518
.412	.1584	.2011	.568	.325

TABLE I - Continued

Two-Blade E" Propeller

45° at 0.75 R

V/nD	C_T	C_P	C_s	η
2.243	0.0377	0.1284	3.387	0.659
2.159	.0485	.1452	3.190	.724
2.092	.0599	.1643	3.002	.763
2.022	.0700	.1793	2.850	.790
1.940	.0815	.1965	2.682	.803
1.859	.0930	.2125	2.532	.814
1.766	.1036	.2251	2.380	.812
1.688	.1133	.2371	2.250	.806
1.595	.1242	.2475	2.108	.800
1.504	.1322	.2586	1.972	.769
1.418	.1338	.2658	1.849	.714
1.343	.1343	.2667	1.750	.678
1.266	.1360	.2671	1.649	.644
1.174	.1378	.2694	1.528	.600
1.112	.1412	.2731	1.444	.575
1.031	.1434	.2766	1.334	.534
.961	.1476	.2824	1.239	.502

TABLE I - Continued

Four-Blade E Propeller

15° at 0.75 R

V/nD	C_T	C_P	C_s	η
0.744	0.0020	0.0155	1.715	0.095
.713	.0137	.0220	1.552	.445
.679	.0244	.0278	1.391	.597
.646	.0353	.0334	1.275	.684
.627	.0405	.0359	1.221	.708
.595	.0494	.0403	1.132	.730
.563	.0600	.0449	1.029	.741
.525	.0680	.0480	.964	.743
.493	.0758	.0512	.895	.731
.467	.0825	.0535	.839	.720
.445	.0861	.0548	.796	.698
.406	.0958	.0576	.719	.677
.381	.1004	.0594	.670	.646
.335	.1086	.0610	.586	.596
.300	.1148	.0624	.523	.552
.263	.1206	.0632	.457	.502
.227	.1258	.0634	.394	.451

TABLE I - Continued

Four-Blade E Propeller

25° at 0.75 R

V/nD	C_T	C_P	C_s	η
1.171	0.0062	0.0327	2.320	0.222
1.128	.0209	.0458	2.090	.515
1.076	.0381	.0594	1.897	.692
1.046	.0488	.0685	1.788	.745
.998	.0613	.0785	1.661	.779
.960	.0719	.0864	1.567	.799
.906	.0824	.0936	1.455	.798
.883	.0828	.0979	1.405	.801
.853	.0978	.1038	1.342	.803
.823	.1041	.1084	1.283	.791
.786	.1126	.1130	1.216	.783
.735	.1221	.1174	1.128	.765
.687	.1331	.1226	1.045	.748
.640	.1429	.1265	.968	.722
.583	.1545	.1300	.877	.693
.523	.1635	.1315	.785	.650
.465	.1736	.1341	.695	.603
.409	.1780	.1368	.609	.532
.333	.1753	.1411	.495	.406
.267	.1771	.1430	.394	.331

TABLE I - Continued

Four-Blade E Propeller

35° at 0.75 R

V/nD	C_T	C_P	C_s	η
1.597	0.0409	0.1032	2.515	0.632
1.544	.0545	.1189	2.364	.708
1.484	.0684	.1347	2.217	.754
1.440	.0796	.1476	2.112	.776
1.406	.0873	.1550	2.042	.790
1.374	.0956	.1641	1.972	.801
1.336	.1031	.1704	1.905	.808
1.274	.1153	.1816	1.792	.808
1.206	.1312	.1954	1.672	.810
1.138	.1451	.2065	1.561	.799
1.078	.1565	.2146	1.467	.786
1.006	.1661	.2213	1.362	.757
.938	.1669	.2268	1.263	.691
.877	.1695	.2275	1.179	.653
.820	.1700	.2265	1.104	.616
.750	.1724	.2298	1.006	.563
.670	.1757	.2352	.895	.501
.584	.1812	.2410	.776	.439
.482	.1843	.2440	.638	.364
.352	.1884	.2534	.463	.262

TABLE I - Continued

Four-Blade E Propeller

45° at 0.75 R

V/nD	C_T	C_P	C_s	η
2.184	0.0661	0.2155	2.978	0.676
2.085	.0865	.2418	2.772	.746
2.020	.0990	.2619	2.640	.764
1.930	.1160	.2856	2.480	.784
1.848	.1289	.3022	2.350	.790
1.807	..1364	.3100	2.283	.796
1.710	.1522	.3290	2.136	.791
1.626	.1635	.3447	2.015	.772
1.542	.1679	.3502	1.902	.739
1.448	.1704	.3500	1.786	.706
1.349	.1716	.3505	1.664	.661
1.258	.1722	.3502	1.552	.619
1.154	.1756	.3510	1.398	.567
1.052	.1779	.3530	1.295	.530
.958	.1815	.3571	1.177	.487
.821	.1830	.3614	1.007	.415
.660	.1876	.3725	.804	.332
.532	.1910	.3828	.644	.265

TABLE I - Continued

Three-Blade E' Propeller

15° at 0.75 R

V/nD	C_T	C_P	C_s	η
0.765	0.0011	0.0136	1.808	0.062
.715	.0176	.0228	1.524	.552
.665	.0344	.0328	1.298	.687
.606	.0474	.0391	1.159	.735
.552	.0619	.0460	1.021	.743
.506	.0733	.0508	.919	.730
.451	.0850	.0549	.806	.698
.396	.0966	.0588	.698	.650
.353	.1040	.0607	.619	.605
.296	.1147	.0629	.515	.539
.245	.1235	.0639	.425	.474

TABLE I - Continued

Three-Blade E' Propeller

25° at 0.75 R

V/nD	C_T	C_P	C_s	η
1.203	0.0081	0.0255	2.510	0.382
1.145	.0204	.0427	2.151	.547
1.085	.0372	.0582	1.916	.694
1.032	.0523	.0705	1.755	.766
.964	.0679	.0829	1.586	.790
.919	.0805	.0929	1.478	.796
.856	.0936	.1025	1.350	.781
.795	.1065	.1105	1.235	.766
.744	.1172	.1158	1.145	.753
.689	.1292	.1221	1.049	.729
.635	.1416	.1278	.944	.695
.550	.1568	.1318	.825	.654
.485	.1671	.1345	.724	.602
.425	.1725	.1398	.630	.524
.379	.1744	.1443	.558	.458
.318	.1747	.1463	.467	.380

TABLE I - Continued

Three-Blade E' Propeller

35° at 0.75 R

V/nD	C_T	C_P	C_s	η
1.625	0.0325	0.0972	2.590	0.543
1.552	.0527	.1150	2.391	.711
1.490	.0657	.1310	2.238	.747
1.465	.0719	.1377	2.179	.765
1.413	.0838	.1513	2.061	.783
1.349	.0979	.1663	1.932	.794
1.290	.1101	.1784	1.821	.796
1.255	.1171	.1852	1.760	.794
1.215	.1250	.1925	1.689	.789
1.169	.1335	.1997	1.613	.782
1.096	.1464	.2099	1.498	.765
1.041	.1557	.2173	1.413	.746
1.016	.1597	.2210	1.373	.734
.985	.1624	.2245	1.328	.712
.950	.1647	.2298	1.275	.681
.919	.1668	.2321	1.250	.660
.876	.1693	.2338	1.172	.634
.810	.1728	.2362	1.081	.592
.753	.1766	.2391	1.003	.556
.634	.1841	.2459	.839	.475
.529	.1900	.2538	.696	.396

TABLE I - Continued

Three-Blade E' Propeller

45° at 0.75 R

V/nD	C_T	C_P	C_s	η
2.277	0.0462	0.1831	3.194	0.574
2.200	.0618	.2044	3.022	.665
2.123	.0772	.2274	2.856	.721
2.042	.0919	.2510	2.691	.748
1.962	.1068	.2703	2.550	.775
1.870	.1219	.2920	2.390	.780
1.779	.1376	.3119	2.248	.785
1.689	.1504	.3281	2.110	.774
1.605	.1619	.3412	1.990	.761
1.512	.1668	.3505	1.865	.719
1.427	.1696	.3537	1.757	.684
1.348	.1720	.3551	1.658	.653
1.271	.1740	.3569	1.562	.620
1.184	.1783	.3608	1.451	.585
1.121	.1805	.3631	1.375	.556
1.051	.1841	.3672	1.285	.527
.974	.1888	.3717	1.187	.495
.885	.1936	.3774	1.075	.454
.781	.1987	.3842	.946	.404

TABLE II

Three-Blade E Propeller with Spinner
35° at 0.75 R

V/nD	C_T	C_P	C_s	η
1.652	0.0178	0.0574	2.926	0.512
1.599	.0384	.0754	2.682	.667
1.541	.0445	.0906	2.498	.757
1.479	.0592	.1073	2.312	.816
1.426	.0692	.1190	2.183	.829
1.361	.0808	.1368	2.051	.848
1.306	.0897	.1586	1.939	.844
1.243	.0999	.1470	1.824	.844
1.196	.1071	.1536	1.739	.833
1.135	.1161	.1602	1.637	.822
1.082	.1235	.1655	1.551	.807
1.030	.1296	.1701	1.466	.784
.975	.1338	.1745	1.383	.744
.932	.1398	.1765	1.319	.708
.888	.1356	.1771	1.257	.671
.839	.1341	.1784	1.185	.651
.787	.1345	.1788	1.111	.598
.736	.1387	.1810	1.066	.556

TABLE II - Continued

Two-Blade E' Propeller with Spinner
35° at 0.75 R

V/nD	C_T	C_P	C_s	η
1.685	0.0099	0.0489	3.164	0.389
1.630	.0240	.0611	2.835	.656
1.566	.0340	.0748	2.638	.718
1.516	.0448	.0870	2.470	.781
1.465	.0543	.0981	2.328	.810
1.386	.0662	.1117	2.149	.821
1.332	.0751	.1205	2.035	.831
1.268	.0866	.1318	1.895	.829
1.188	.0977	.1457	1.754	.814
1.126	.1072	.1495	1.647	.807
1.065	.1157	.1558	1.545	.791
.968	.1290	.1633	1.392	.765
.906	.1345	.1757	1.285	.701
.827	.1357	.1776	1.168	.632
.741	.1396	.1801	1.044	.574
.656	.1440	.1844	.920	.512

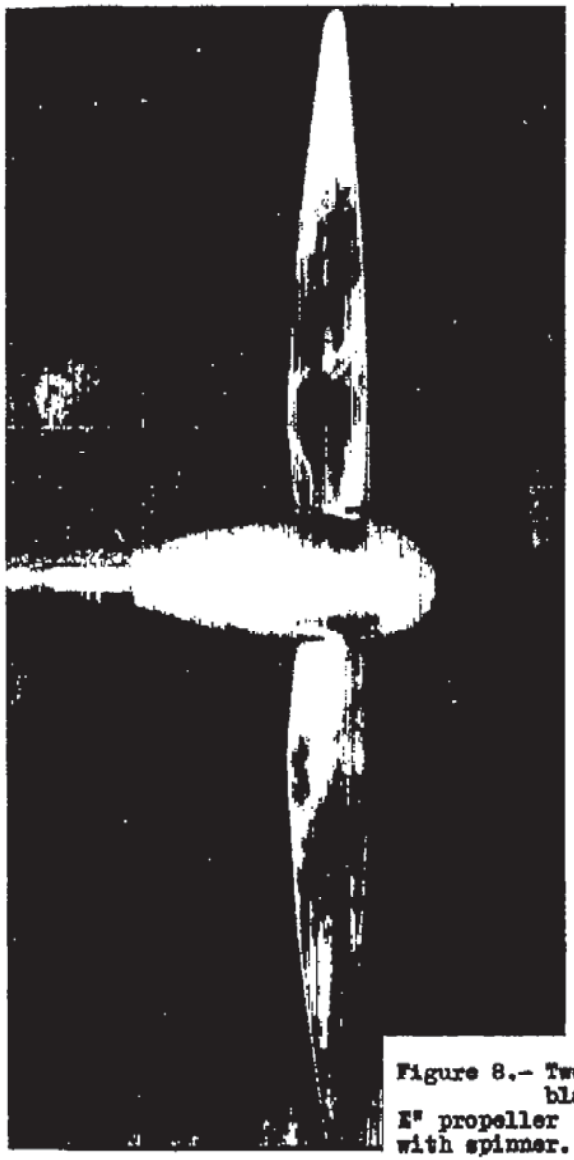

Figure 8.- Two-blade E" propeller with spinner.

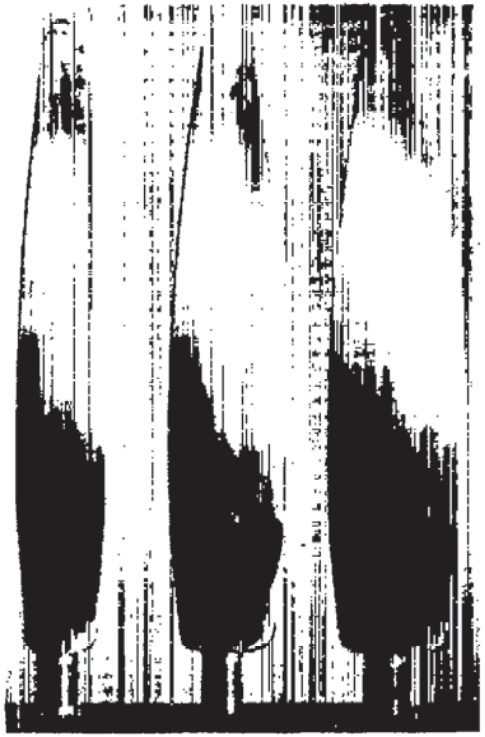

Figure 1. Blade plan forms.

E E' E".

Figure 2.- Propeller hubs.

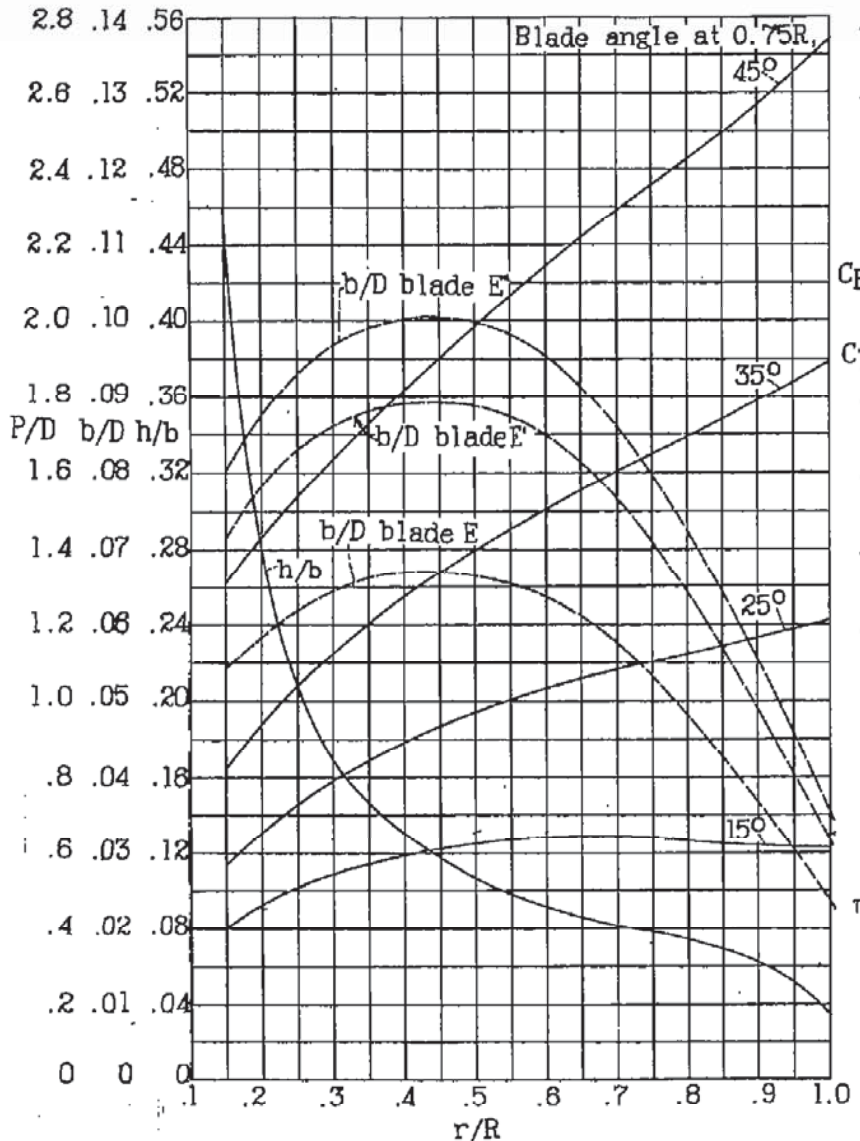

Figure 3.- Blade-form curves.

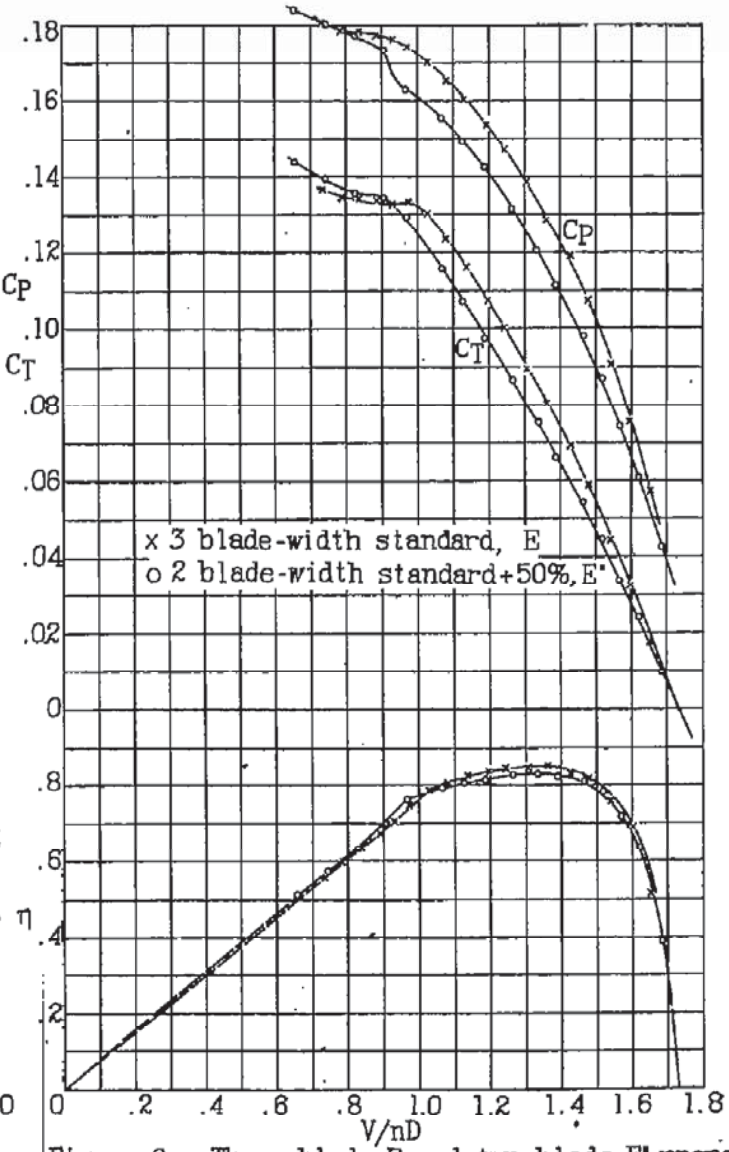

Figure 9.- Three-blade E and two-blade E' propellers with spinners. Blade angle 35°.

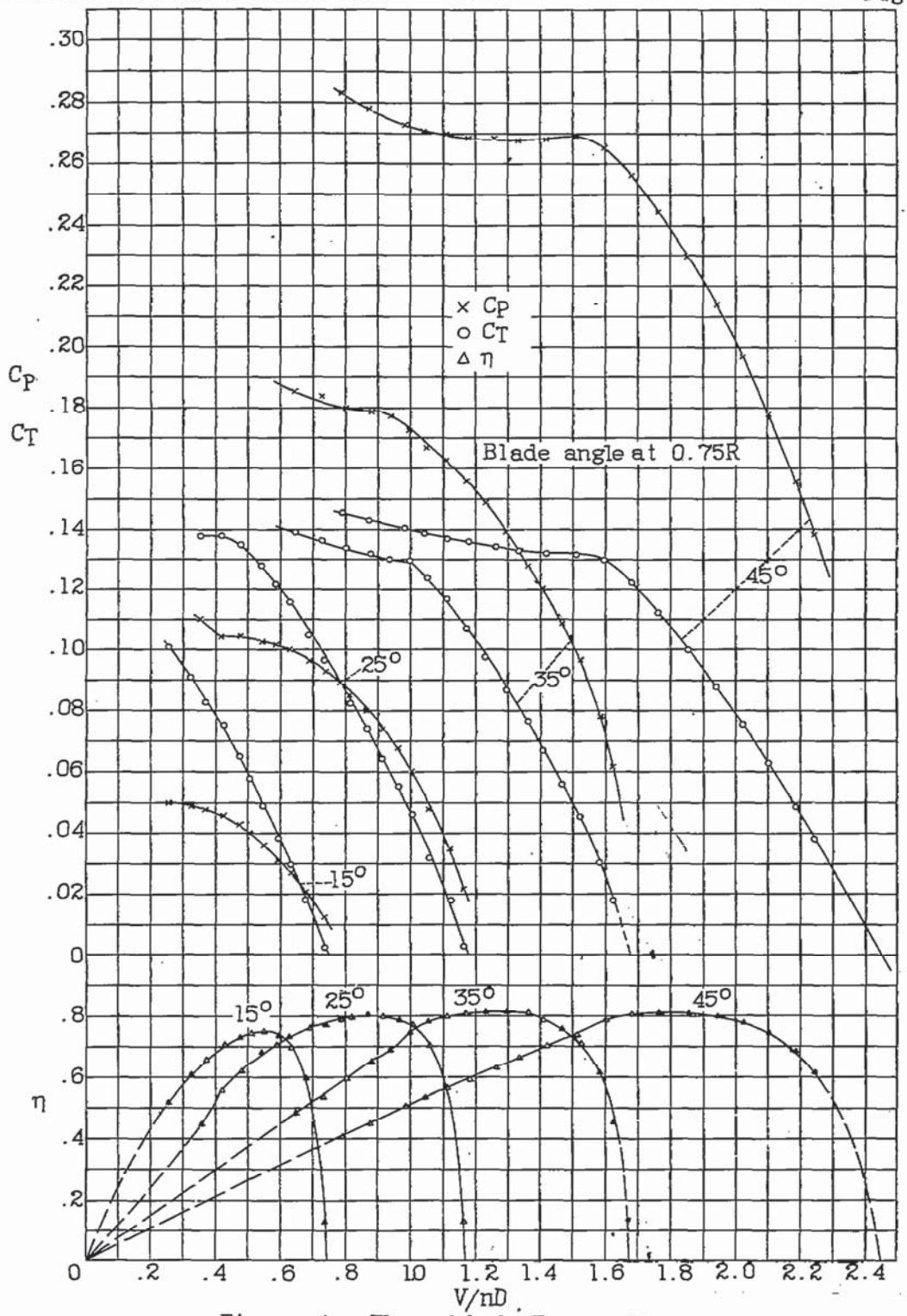

Figure 4.- Three-blade E propeller.

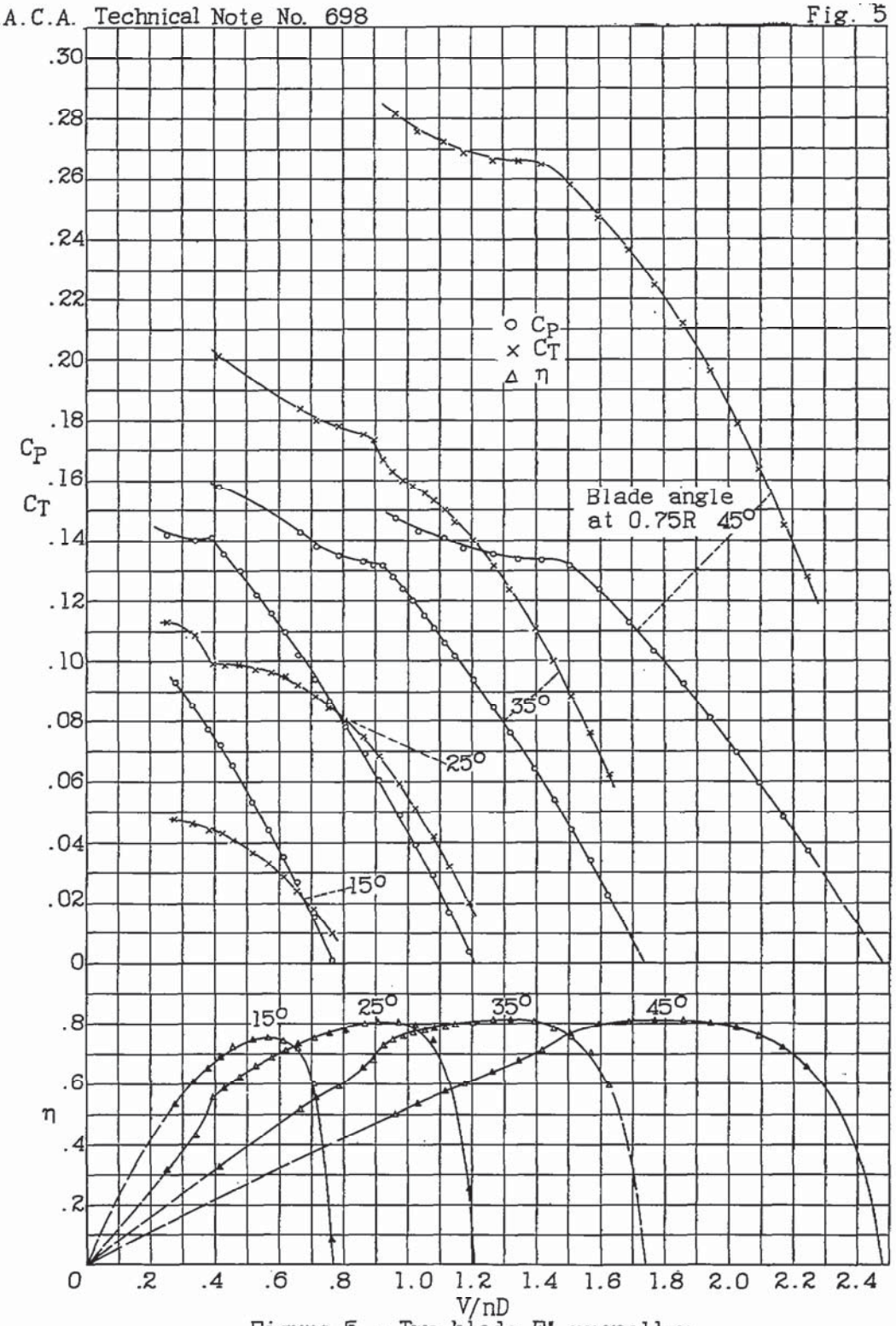

Figure 5.- Two-blade E' propeller.

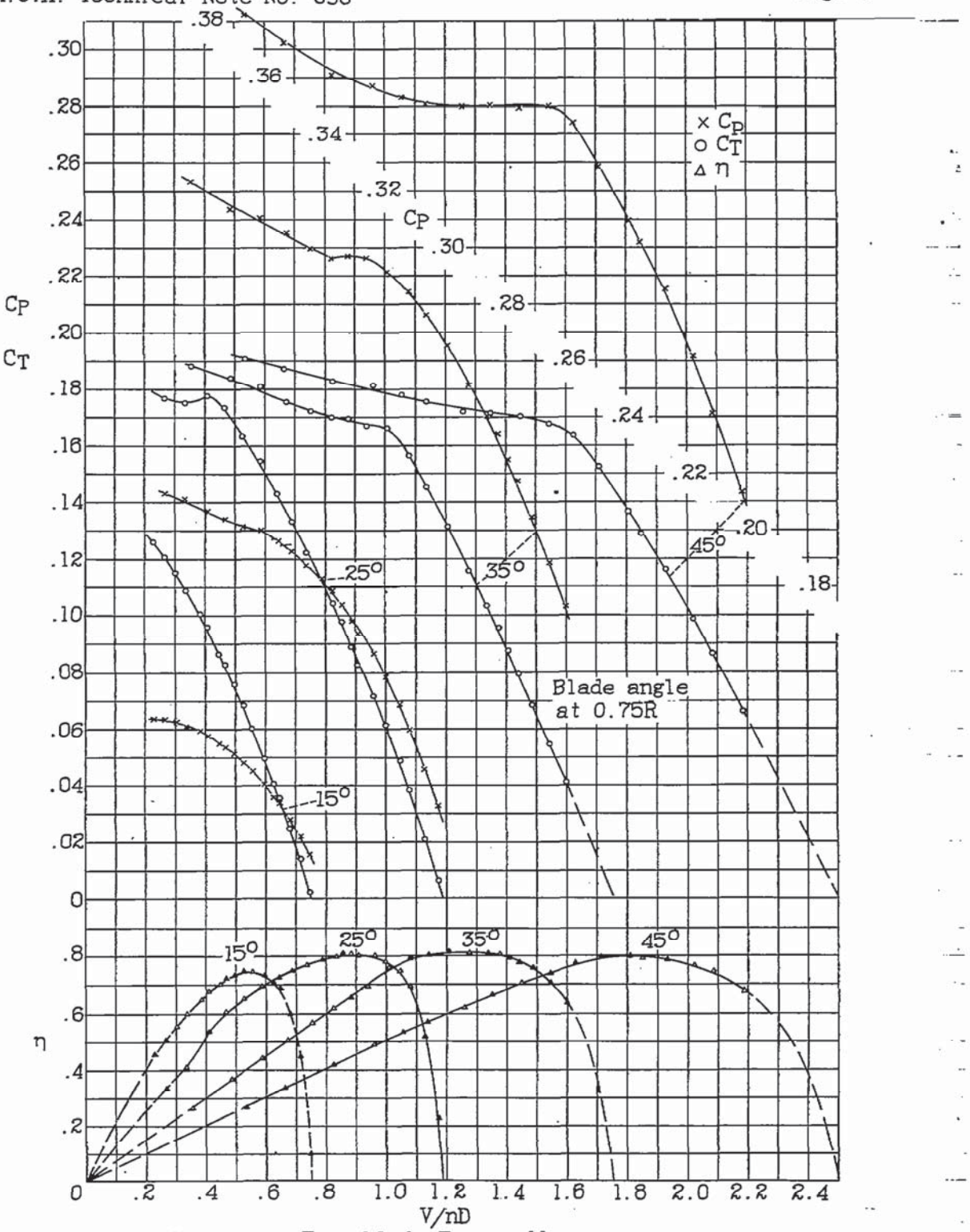

Figure 6.- Four-blade E propeller.

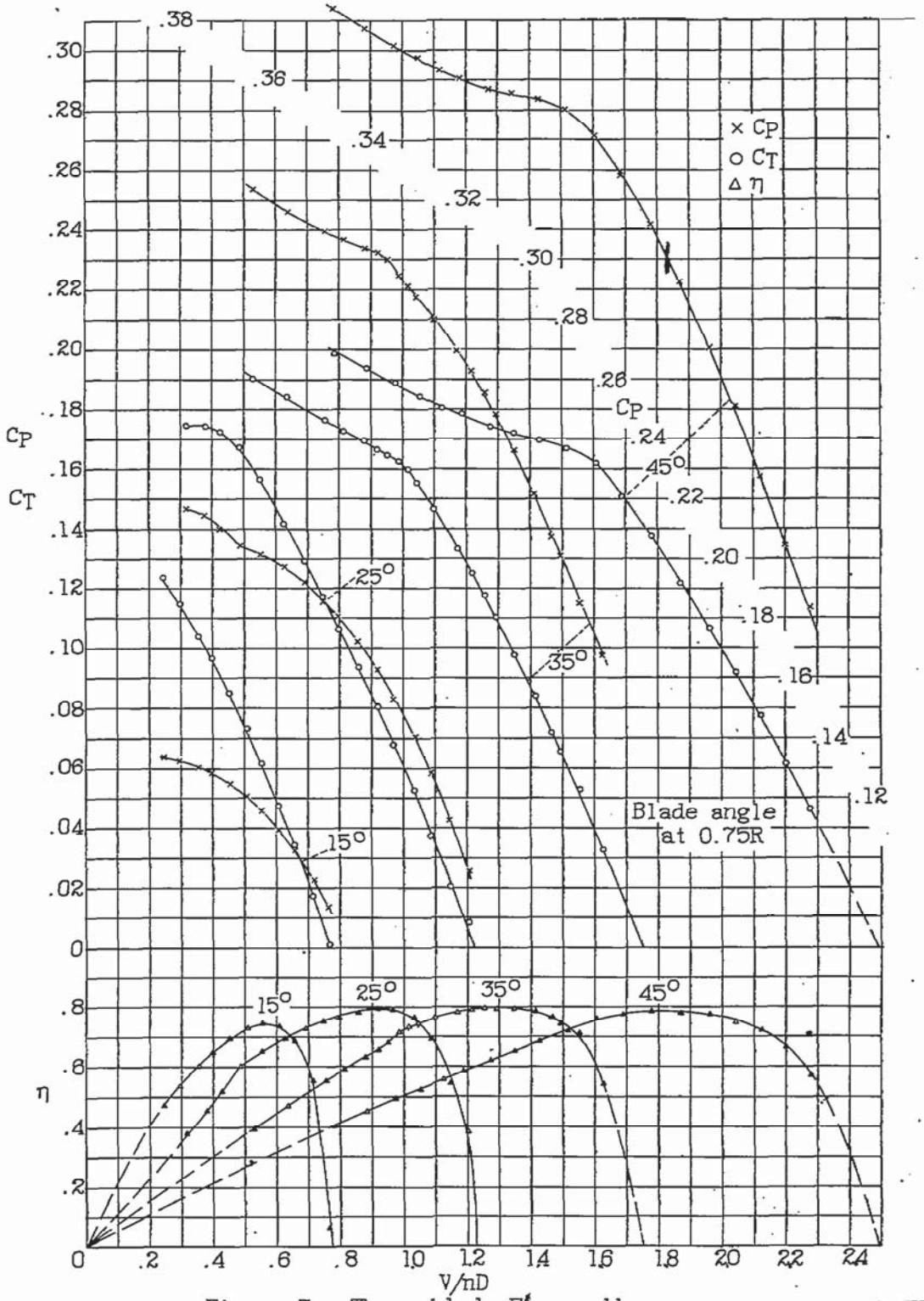

Figure 7.- Three-blade E propeller.